Turbulence and Heterogeneous Wind Conditions in the Field of Wind Energy

Quantification of Heterogeneity Effect on Lidar Measurements and Turbulence Normalisation on Wind Turbine Power Curves

R. Keus B.Sc.

24-4-2017

TUDelft
Delft
University of
Technology

Challenge the future

Turbulence and Heterogeneous Wind Conditions in the Field of Wind Energy

Quantification of Heterogeneity Effect on Lidar Measurements and Turbulence Normalisation on Wind Turbine Power Curves

Master of Science Thesis

For obtaining the degree of Master of Science in Aerospace Engineering at Delft University of Technology

R. Keus B.Sc.

24-4-2017

Faculty of Aerospace Engineering · Delft University of Technology

DELFT UNIVERSITY OF TECHNOLOGY
DEPARTMENT OF
WIND ENERGY

The undersigned hereby certify that they have read and recommend to the Faculty of Aerospace Engineering for acceptance a thesis entitled **"Turbulence and Heterogeneous Wind Conditions in the Field of Wind Energy"** by **R. Keus B.Sc.** in partial fulfillment of the requirements for the degree of **Master of Science**.

Dated: <u>24-4-2017</u>

Head of department:
_____
Prof.dr. G.J.W. van Bussel

Supervisor:
_____
Dr.ir. W.A.A.M. Bierbooms

Reader:
_____
Ir. V.P. Brügemann

Reader:
_____
Drs. J.P. Coelingh

Summary

Monitoring and optimising turbine performance are important tasks of a wind energy operator. However, monitoring activities are expensive and the current state-of-the-art in this field could be improved. A newly developed Avent five-beam Lidar was tested and the impact of heterogeneity on Lidar measurements was analysed. Also, the effect of turbulence on turbine performance was investigated.

The Avent five-beam Lidar measurements were compared to several measurement devices: an IEC-compliant met-mast, a ZephIR Lidar and a ROMO Wind spinner anemometer. The Avent five-beam Lidar proved to be an accurate measurement device compared to the met-mast in measuring wind speed and yaw misalignment. However, the thresholds for its availability seemed to be too conservative. The Avent Lidar underestimated the power curve and consequently measured up to 3.5% difference in AEP. Furthermore, by including a meteorological station at hub height, a more accurate PCV can be performed. The IEC presented a methodology to normalise power curves in order to determine the effects of turbulence on power curves. It was expected that the scatter would be improved and that power curve uncertainty would be reduced. Simulations showed the effects on the power curves and a lower scatter was obtained after normalising the power curves to one turbulence intensity. The theoretical results were validated with measurements from two measurement campaigns, however the circumstances were different due to varying conditions next to turbulence intensity during the measurement campaign. The effects of turbulence on the power curves were clearly observed whereas no improvement in the scatter around the power curves was perceived. Therefore, it could be valuable to investigate the turbulence normalisation by isolating the effects of turbulence.

Simulations were performed to approach heterogeneous wind conditions. Also, a five-beam Lidar was simulated to analyse its ability to correct for heterogeneity. Measurements from the met-mast and Avent five-beam Lidar were used to validate the simulations in order to examine the magnitude and possible effect on Lidar measurements. It was found that the effect of heterogeneity depended on the magnitude. A linear correction could be applied, but was insufficient in wind fields with large heterogeneity. In case of low heterogeneity, a correction is not needed. Finally, it is recommended to investigate heterogeneity further by measuring with a Lidar continuously looking into the direction of a met-mast.

Acknowledgements

I would like to thank several people who contributed to this master thesis, which is the final work to obtain my master of science in Aerospace Engineering.

First, I would like to thank Jan Coelingh, who was my supervisor at Vattenfall. He gave me the opportunity to execute this project. Jan was always available for questions and discussions and a great support. Also, his valuable time and willingness to brainstorm about the various changes in this research were very useful.

Secondly, I would like to thank Wim Bierbooms, who was my supervisor at TU Delft, for his patience and support in overcoming numerous obstacles I have been facing through my research. Wim steered and guided me in the right the direction and helped me to strive for the best results possible.

Furthermore, I would like to thank my colleagues at the Wind & Site team and other teams for the pleasant working experience at Nuon. In particular, I would like to thank Stefan Goossens, Jorn Goldenbeld, Stathis Koutoulakos, Carelva Marchena and Henrik van der Velde. It was always a pleasure to work next to you in the office and I very much enjoyed our pleasant discussions and coffee meetings.

Finally, I would like to express my gratitude to my parents, girlfriend and friends for providing me with unfailing support and continuous encouragement throughout the years of my study and during the process of writing this thesis. You gave me all the support I needed to finalise this task.

Contents

List of Figures

List of Tables

Nomenclature

Latin Symbols

a	Wind shear coefficient	[-]
A	Weibull scale parameter/Area	$[-/m^2]$
c	Cubic fit parameter	[-]
C_P	Power coefficient	[-]
D	Rotor diameter	$[m]$
f	Doppler frequency shift/Gaussian wind distribution	$[Hz/\text{-}]$
h	Height	$[m]$
k	Calibration constant/Weibull shape parameter	[-]
l	Distance	$[m]$
M	Molar Mass	$[kg/mol]$
n_h	Number of measurement heights	[-]
N	Number of data points	[-]
p	Pressure	$[Pa]$
P	Power	$[W]$
P_{kin}	Kinetic energy flux	$[J/m^2/s]$
r	Ratio between right and left LOS radial velocities	[-]
R	Gas constant/Measurement range	$[(J/(kgK))/\text{m}]$
R^2	Coefficient of Determination	[-]
t	Time	$[s]$
T	Air temperature	$[K]$
u	Wind speed in x-direction	$[m/s]$

U	Mean wind speed	$[m/s]$
v	Wind speed in y-direction	$[m/s]$
V	Wind vector	$[m/s]$
V_{eq}	Rotor equivalent wind speed	$[m/s]$
w	Wind speed in z-direction	$[m/s]$
x	Number of rotor diameters	[-]
X	Heterogeneity	[-]
z	Height	$[m]$

Greek Symbols

α	Cone angle/Inflow angle	[°]
β	Half-opening angle	[°]
β_{tilt}	Lidar tilt angle	[°]
δ	Shaft tilt angle	[°]
γ	Yaw misalignment	[°]
λ	Lidar signal wavelength	$[nm]$
μ	Mean	[-]
ϕ	Wind direction	[°]
ρ	Air density	$[kg/m^3]$
σ	Standard deviation	[-]
θ	Azimuthal direction	[°]
θ_d	Disturbed sector width	[°]

Abbreviations

ABL	Atmospheric Boundary Layer
AEP	Annual Energy Production
CW	Continuous-Wave
HWS	Horizontal Wind Speed
IEC	International Electrotechnical Commission
LES	Large Eddy Simulations
Lidar	LIght Detection And Ranging
LOS	Line-of-sight
PCV	Power Curve Verification
REWS	Rotor Equivalent Wind Speed
RWS	Radial Wind Speed

SCADA	Supervisory Control And Data Acquisition
TI	Turbulence Intensity
UTC	Coordinated Universal Time
WPDC	Wind Power Data Center
YM	Yaw Misalignment

Chapter 1

Introduction

A target to achieve 20% energy from renewables by 2020 was set for the EU. Wind energy is expected to be the main source of renewable energy. Vattenfall is a company which generates electricity partly by wind power and will contribute to the increase of wind energy. This can be done by developing new wind farms, by making bigger turbines, by expanding offshore wind activities and by increasing the operational efficiency.

Currently, cup anemometers mounted on a met-mast monitor the operational efficiency of wind turbines by performing wind resource assessments and Power Curve Verification (PCV). These met-masts are IEC-certified, which means that they comply with the standards of the International Electrotechnical Commission (IEC)[21]. However, turbines reach higher and higher which requires taller met-masts to monitor the wind conditions, and the costs for taller met-masts increase approximately to the third power with height[39]. Also, locating turbines offshore leads to an increase in costs of wind resource assessment, because met-masts are relatively expensive to install offshore. Therefore, research has been performed into novel measurement techniques such as Lidar (LIght Detection And Ranging) and spinner anemometers[19][51][61].

Although Lidars and spinner anemometers can reduce the costs of monitoring activities due to their lower costs and easier installation, they also provide valuable accurate measurements. Moreover, increasing the accuracy and reliability of these measurement devices can lower the agreed uncertainty in power curve warranties. In most cases, power curve underperformance occurs due to a too optimistic yield expectation[1]. Currently, an uncertainty of 5% to 8%, depending on annual wind, is incorporated into the power curve warranty to deal with measurement errors which impedes financial compensation in case of limited underperformance. However, if Lidar becomes a trustworthy measurement device resulting in lower uncertainty in PCV, Vattenfall's negotiating position against turbine manufacturers could improve.

Lidar is not yet IEC-certified and has consequently not been used as default reference system yet. Therefore, further research is required to support a transition of replacing met-masts by approved (nacelle-based) Lidars. For instance, the performance to mea-

sure YM and TI is to be determined. Also, the effect of heterogeneity on the Lidar measurements should be investigated[61].

In addition, the operational efficiency of wind turbines depends on several variables such as yaw misalignment (YM) and turbulence intensity (TI). Although a wind turbine will be corrected for YM, it cannot be defined beforehand what average YM the turbine will experience. However, TI will be measured during a site assessment which is performed to determine the local wind conditions of a potential site. It is therefore interesting to implement the effect of TI into the power curves. Recently, a method to determine the effect of TI on the power production has been reported in a new IEC standard. Hence, this thesis will be focused on the following research question:

To what extent can a (nacelle-based) Lidar measure YM and TI accurately compared to other measurement devices and what is the effect of heterogeneity on its measurements, as well as turbulence normalisation on turbine power performance?

From the main research question the following subquestions have been formulated to guide this thesis:

1. What is the difference in PCV between a ground- or nacelle-based Lidar and a met-mast?

2. How does accuracy in measuring wind conditions and PCV of a five-beam Lidar compare to other nacelle-based Lidar, spinner anemometers and IEC-compliant met-masts?

3. What is the effect of turbulence normalisation on the turbine performance and AEP? And how does it affect the scatter around the power curve?

4. Can heterogeneity be quantified? And what is its effect on Lidar measurements?

In this thesis, measurements from a nacelle-based five-beam Lidar will be compared to spinner anemometers, and to another nacelle-based Lidar as well as to an IEC-compliant met-mast to understand the differences in wind speed, wind direction and TI measurements. This will help to interpret and analyse measurements from nacelle-based Lidar. Also, power curves will be made with measurements of nacelle-based Lidar. These will be analysed in the context of the IEC standard to determine Lidar's accuracy for PCV, but also to investigate causes of possible underperformance of wind turbines. Also, by gaining more practical experience and understanding, the author seeks to increase the benefits of using Lidar as measurement device in wind farms for Vattenfall.

Furthermore, the effect of TI on the power curve will be investigated. This will be done by following the IEC reported process to normalise power curves for turbulence as described in the new IEC[22]. The normalisation allows to generate site-specific power curves, so that power curves can be adjusted to a dominant TI at the site of interest. Also, the change in scatter around the power curve will be analysed since this method to normalise power curves could result in power curves less sensitive to TI. Similarly, the power curve measurement uncertainty could be reduced leading to an improvement in the annual energy production (AEP) estimation.

Moreover, the concept of heterogeneity is fairly unknown, which enlarges the potential value of this research. The differences in wind conditions measured by Lidar beams will be investigated for this purpose. The concept of heterogeneity will also be explored with a five-beam Lidar from Avent, which is beneficial for Vattenfall as knowledge and experience with a newly developed remote sensing device can be gained in the field of wind monitoring activities.

To conclude, the research will examine a unique test configuration with two nacelle-based Lidars, sonic spinner anemometers and a met-mast. Also, measurements from a ground-based Lidar, which is moved to another location within a wind farm but without a reference met-mast nearby, will be investigated. The research can help to find the optimal device for a specific application (measuring TI, YM, wakes or PCV). Furthermore, it can help to strengthen the reliability and robustness of (nacelle-based) Lidar in wind energy applications.

The thesis continues with the theoretical background described in chapter 2. This will be followed by an overview of the relevant literature in chapter 3. In chapter 4, the measurement set-up is provided and chapter 5 treats the validation of the data from the measurement campaigns at Prinses Alexia and Nørrekær Enge. The turbine performance of the turbines under research at both sites will be discussed in chapter 6. In chapter 7, the turbulence normalisation of the power measurements is described. Furthermore, chapter 8 addresses the concept of heterogeneity and its effect on Lidar measurements. Finally, the conclusions and recommendations of this research are presented in chapter 9.

Chapter 2

Theoretical Background

In this chapter the theory behind the thesis will be presented. First, the working principle, benefits and drawbacks, and installation procedure of Lidar and spinner anemometers will be discussed. Secondly, the standard for power curve measurements will be described. Especially, the normalisation of power curves according to TI is explained. Finally, an introduction into the concept of heterogeneity will be presented.

In the early stages of monitoring wind power resources cup anemometers were used as the main wind measurement device. These were installed on an IEC compliant meteorological mast (further referred as met-mast) to be able to measure the wind conditions at heights corresponding to the rotor. Since 2006, Lidar has been investigated extensively as an alternative for monitoring wind conditions. In addition, spinner anemometers were introduced to measure YM and its effect on turbine performance. Thus, various wind measurement devices have been used to monitor and improve wind turbine yield. The specific type of the Lidars that will be treated in this chapter in more detail are nacelle-based (a ZephIR DM and an Avent five-beam Lidar), the sonic spinner anemometers are from ROMO Wind.

2.1   Lidar

Single-shot lasers observed "clear air" during an experimental program in 1965, which was one of the first applications of Lidar. It was found that Lidar can be used to observe clouds, but it was recommended to use higher pulse-repetition frequencies [12]. Collis describes the potential applications in meteorology. Furthermore, a prediction was made that Lidar will play a role in defining atmospheric conditions by making quantitative observations[14].

One of those atmospheric conditions that is interesting in the field of wind energy is wind speed. In 1975, Eloranta et al. measured the wind speed of vertical profiles in the low atmosphere, from 0 to 1 km height, with a Lidar. The measurements of this Lidar were

compared to measurements of pilot balloons from which it could be concluded that Lidar is able measure wind speed in the boundary layer remotely.[16]

Using Lidar in wind energy evolved in 2006, primarily to investigate its suitability as measurement device for wind resource assessment. One of the first studies was performed by Kindler et al. who analysed the performance of a ZephIR Lidar. It was tested onshore and offshore revealing its flexibility and manoeuvrability. Observations from the experiments against measurements from met-masts showed that the Lidar can be a helpful measurement device to determine flow conditions remotely. However, more research on the applicability in wake flows, high shear or complex terrain was recommended.[28]

Nacelle-based Lidar

Recently, an upwind-looking nacelle-based Lidar (Wind Iris) was applied at a wind farm of Vattenfall: Slufterdam West. Goossens concluded that the Wind Iris measured wind speed accurately. However, an uncertainty in wind direction of about 4° was found instead of the expected 0.5°. Also, significant spread was observed in the TI measurements between the Lidar and a Sodar ($R^2 = 0.25$).[19]

Wagenaar et al. found that wind speed, TI and YM measurements as well as PCV between a nacelle-based Lidar and a met-mast compared well[55]. It was suggested that Lidar can be applied for site assessments, PCV, YM correction and wind turbine control, which will be further discussed in chapter 3. A nacelle-based Lidar can also be applied as downwind-looking for measuring turbine wake effects. This application allows for validating wake models, which can help to quantify the decrease in energy production of downwind turbines. It also allows to determine the increase in fatigue loads due to a turbulent environment in the wake of a turbine[23].

Well-known nacelle-based Lidars are the Wind Iris and ZephIR DM. The former can measure horizontal wind speed (HWS) and YM from 40 to 400 m whereas the latter one can measure from 10 to 300+ m[2][65]. Their advantage over ground-based Lidars is that they do not need support structures since they can be installed on top of a nacelle. But, the change in measurement height due to tilt and roll movements of the nacelle should be incorporated into the measurements[59].

Five-beam Lidar

A newly developed nacelle-based Lidar is the Avent five-beam Lidar. It contains five beams with four beams pointing at the corners of a square and one in the centre, which can be used in two different configurations as shown in Figure 2.1. The Lidar can measure at 10 different ranges simultaneously with a measurement frequency of 1 or 4 Hz. The angle between the centre beam and the other beams is α, which is equal to 15° as a result of combining the horizontal (α_h) and vertical half-opening angle (α_v) of 10.73°, which are called β in Figure 2.1. Assuming that no YM occurs, the radial wind speed (RWS) measured by the centre beam, or line-of-sight (LOS) 0, equals the HWS. This Lidar allows for a more accurate wind field estimation, because of more measurement points at the configured ranges. The derivation of the HWS and direction measurements is given in subsection 2.1.2.
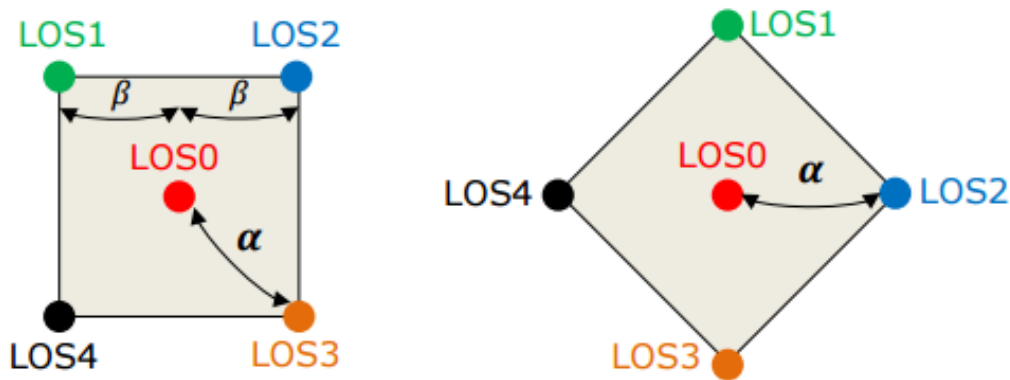
Figure 2.1: Five-beam Lidar LOS configurations[8]

2.1.1 Continuous Wave and Pulsed Lidars

In principle, there are two types of Lidars: *continuous-wave (cw)* and *pulsed*. A cw Lidar emits a beam of light continuously at a fixed elevation focussed at a certain height. However, the measurement height and spatial resolution can be changed by adjusting the focal settings of the telescope. A common limit of the measuring height is between 200 and 300 m due to the so-called "probe length", which increases with the square of the measuring range. Also, the measuring height can be influenced by changes in the aerosol concentration (mist layers) resulting in significant backscatter from wrong heights.[33]

Another approach to take measurements is by transmitting a sequence of light pulses and keep track of the time until the backscatter is received. This (pulsed) Lidar can measure at several heights at a time, in contrast to cw Lidar that needs to adjust its focal settings[54]. In addition, the spatial resolution is independent of the measurement range which is a limiting factor of the cw Lidar. In this way a spatial resolution of 30 to 40 m can be obtained at each measurement height. However, the maximum measurement height of a pulsed Lidar is limited by a lower returning signal with increasing height due to scattering[33]. This results in a maximum measurement height of about 300 m.[39]

Although the spatial resolution of a pulsed Lidar is independent of the measurement range, a cw Lidar features a higher data acquisition rate. This allows for turbulence measurements, which is important to maximise energy production and to ensure structural integrity of the turbines. On the other hand, a pulsed Lidar measures with a constant spatial resolution, but lower than with a cw Lidar. The principle of both techniques is shown in Figure 2.2 and Figure 2.3.

2.1.2 Working principle

The acronym of Lidar, Light Detection and Ranging, describes the remote measurement technique that uses laser signals. The time between emitting a light pulse and receiving the scattered signal determines the distance to the object that reflects the light. For wind energy applications, the technology of (Doppler) Lidar is applicable to measure wind speed and direction remotely. Electromagnetic radiation, i.e. light, is transmitted in different directions by using a turning mirror or rotating parts[39]. The receiver collects scattering
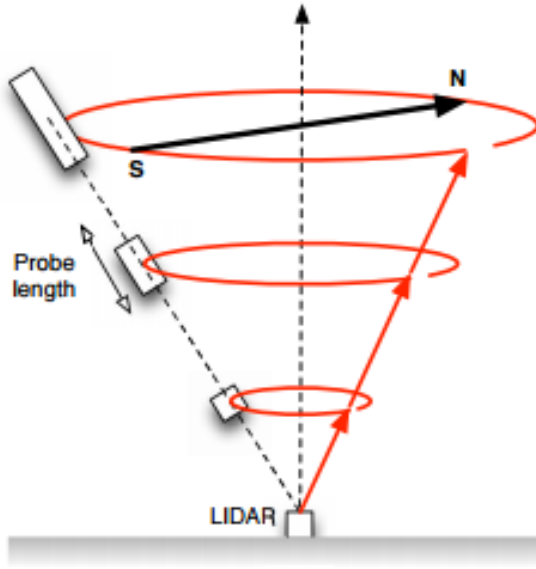
Figure 2.2: Continuous-wave Lidar[11]
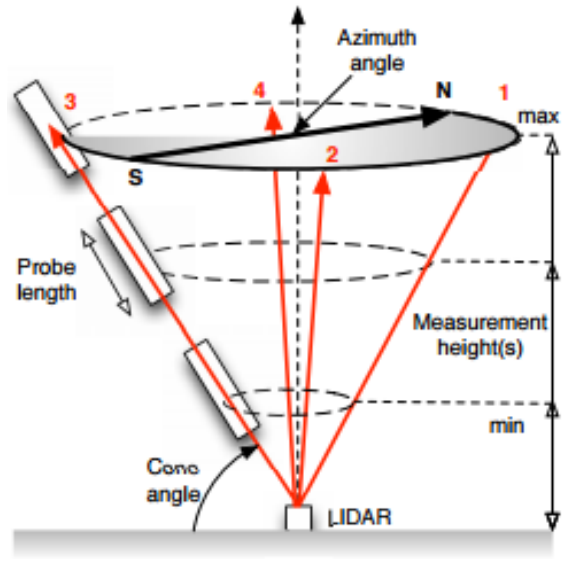
Figure 2.3: Pulsed Lidar[11]

of the light from aerosols in the air, which are typically dust, water droplets, pollution, pollen or salt crystals[48].

Lidar transmits electromagnetic radiation without danger for human eyes, because a wavelength of 1.55 μm is used. The scattered light is collected by a receiver with a very high sensitivity that can detect scatter from one photon for every 10^{12} transmitted[48]. The reflecting photon causes a frequency shift due to its movement proportional to the LOS velocity as given by the relation shown in Equation 2.1[30].

$$\Delta f = \frac{2|\mathbf{U}|\cos\phi}{\lambda} \tag{2.1}$$

Here, $\mathbf{U}$ is the velocity of the scattering particle, λ the wavelength of the transmitted light, and ϕ the angle between the wind direction and LOS from the Lidar. The underlying principle of this technique is called "Doppler effect" which is also heard in the change of the sound from a passing ambulance. The configuration of such a carbon dioxide laser Doppler Lidar is given in Figure 2.4. The laser beam is split before it enters the telescope and pointed at the target of interest. The shifted scatter is collected and amplified after which it is detected and processed.[30]

To be able to monitor the wind energy available in a wind field, the LOS velocity does not give enough information. Therefore, a second target near the measurement point is to be analysed by using a two-beam[2] or a moving beam[65] Lidar under the assumption of a homogeneous wind field in the measurement range[10], as shown in Figure 2.5. As discussed by Goossens, a larger opening angle increases the accuracy of YM and wind speed measurements, but a smaller opening angle results in a better indication of the local wind speed. In addition, the accuracy depends on the type of Doppler Lidar that is used (cw or pulsed).

In principle, the LOS measurements of a two-beam Lidar are related to the wind vector, opening angle and misalignment of the wind flow with the Lidar axis as follows[59]:
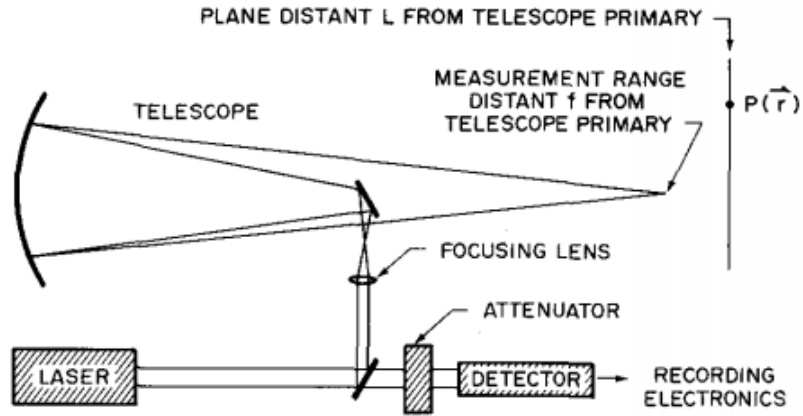
Figure 2.4: Schematic of laser Doppler system for remote wind sensing[30]

$$V_r = V\cos(\alpha + \gamma) \tag{2.2a}$$

$$V_l = V\cos(\alpha - \gamma) \tag{2.2b}$$

$$\gamma = \tan^{-1}\left(\frac{r-1}{\tan(\alpha(r+1))}\right) \tag{2.2c}$$

where V_r and V_l are the RWS measured by the right and left LOS, γ is the angle between the wind direction and the Lidar axis, and r is the ratio between both LOS velocities ($r = \frac{V_r}{V_l}$). The wind vector is a combination of the wind speeds in x- and y-direction:

$$u = V\cos(\gamma) \tag{2.3a}$$

$$v = V\sin(\gamma) \tag{2.3b}$$

Hence, the wind speeds in x- and y-direction can be obtained from the Lidar measurements as follows:

$$u = \frac{V_r + V_l}{2\cos\alpha} \tag{2.4a}$$

$$v = \frac{V_r - V_l}{2\sin\alpha} \tag{2.4b}$$

Finally, HWS and YM can be calculated with Equation 2.5 using the RWS measurements.

$$HWS = \sqrt{u^2 + v^2} \tag{2.5a}$$

$$\gamma = \arctan\left(\frac{v}{u}\right) \tag{2.5b}$$

In the case of the five-beam Lidar, the wind speeds in x- and y-direction can be calculated with the two top and bottom beams (LOS 1 and LOS 2 or LOS 3 and LOS 4 according to
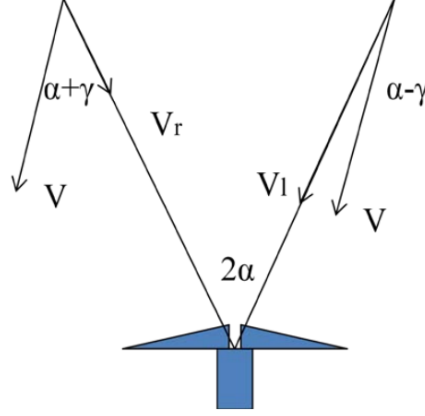
Figure 2.5: Two-beam Lidar measures wind speed and direction from two LOS vectors[59]

the left configuration in Figure 2.1). When it is assumed that the flow is homogeneous, the following equation can be used[8]:

$$u = \frac{V_r + V_l}{2\cos\alpha_h \cos\alpha_v} \tag{2.6a}$$

$$v = \frac{V_r - V_l}{2\sin\alpha_h \cos\alpha_v} \tag{2.6b}$$

Another assumption should be made to define the wind speeds at hub height, which is a linear vertical wind speed profile. Hence, the wind speeds at hub height and consequently the HWS can be calculated as follows[8]:

$$u_{hub} = \frac{u_{top} + u_{bot}}{2} = \frac{V_{r_{top}} + V_{l_{top}} + V_{r_{bot}} + V_{l_{bot}}}{4\cos\beta_h \cos\beta_v} \tag{2.7a}$$

$$v_{hub} = \frac{v_{top} + v_{bot}}{2} = \frac{V_{r_{top}} - V_{l_{top}} + V_{r_{bot}} - V_{l_{bot}}}{4\sin\beta_h \cos\beta_v} \tag{2.7b}$$

$$HWS = \sqrt{u_{hub}^2 + v_{hub}^2} \tag{2.7c}$$

2.1.3   Benefits and drawbacks

The ability to measure wind speed and direction or YM remotely can be seen as the main advantage of Lidar. However, the measurement range is limited by the optic sensitivity limit of the receiver[40]. Overall, a ground-based Lidar should be installed at a measurement distance of 2.5 rotor diameters away from the turbine to be tested[22], but it is accompanied by easy installation and relative flexibility. Furthermore, a nacelle-based Lidar can be installed at the top of the turbine so that no support structure is required.

In addition, a large area can be measured by Lidar while a fixed cup anemometer takes point measurements. This allows the Lidar to aim outside the areas which are disturbed by, for example, wakes or obstacles. Moreover, a better approximation of the wind conditions along the whole rotor can be made. A Lidar can also measure at different heights as ground-based, or at different distances as nacelle-based. Thus, more reliable data can be

collected during a measurement campaign. However, multiple scattering due to cloudy or bad weather (rain or snow) influences the measurements. The data will then be affected by the errors in the Lidar signals.[63]

In contrast to cup anemometers, Lidar does not interfere with the flow. This means that inertial effects on the measurements due to the so-called "over-speeding" of cup anemometers are absent[34]. This phenomenon is caused by a faster response of the cup anemometer to accelerating wind than decelerating, which will increase the average wind speed measured by a cup anemometer.

On the other hand, the principle of Lidar relies on homogeneous flow conditions in the measurement area. However, this assumption does not hold in complex terrain or wind turbine wakes. The resulting inhomogeneous flow can result in wind speed measurement errors on the edges of the wake up to 15% and at the centre up to 30% of the wind speed measured at hub height depending on the complexity and steepness of the terrain[31].

On a similar note, Lidar measurements can be affected by different sources of error from the system itself. Some of these errors, *range weighting* and *directional bias*, were investigated using realistic simulations with a spinner mounted Lidar[45]. In case of a cw Lidar, the first error is caused by taking measurements along a laser beam, which samples a volume of an infinitely thin beam instead of a single point. This follows from integrating the wind speed measurements taken along that beam with a weighting function, which filters the measurements to determine the wind speed at the target point. The error of a pulsed Lidar is caused by the spatial averaging, since it measures at several ranges. "Pulsed Lidars emit a collimated laser pulse and integrate the backscattered light as the pulse travels through several 'range gates'"[45, pp. 416]. Therefore, it measures the wind speed at several distances. Furthermore, the Lidar measures only radial wind velocity with the assumption that it is only due to the mean stream-wise component (u). Thus, a directional bias occurs when the Lidar is measuring while it is misaligned in yaw (γ) and/or azimuthal direction (θ). This error will increase with larger misalignment angles as shown by the following relation:

$$err(\hat{u}) = \tan\gamma(v\sin\theta - w\cos\theta) \tag{2.8}$$

2.1.4 Installation

As discussed in the previous section, Lidar can be installed at the ground, but also at the nacelle of a wind turbine. Both configurations require accurate installation to measure power curves reliably, since a small offset in measurement height can have significant effects on the power curve. For example, a Lidar that measures at a lower height than expected, records lower wind speeds due to wind shear which results in an overestimated power curve. In the subsequent chapters more details on the installation procedure will be provided to avoid measurement uncertainties.

Height

The height at which a Lidar will be measuring should be within ± 2% of hub-height as discussed by the IEC. Since a Lidar can measure at different ranges or heights, it
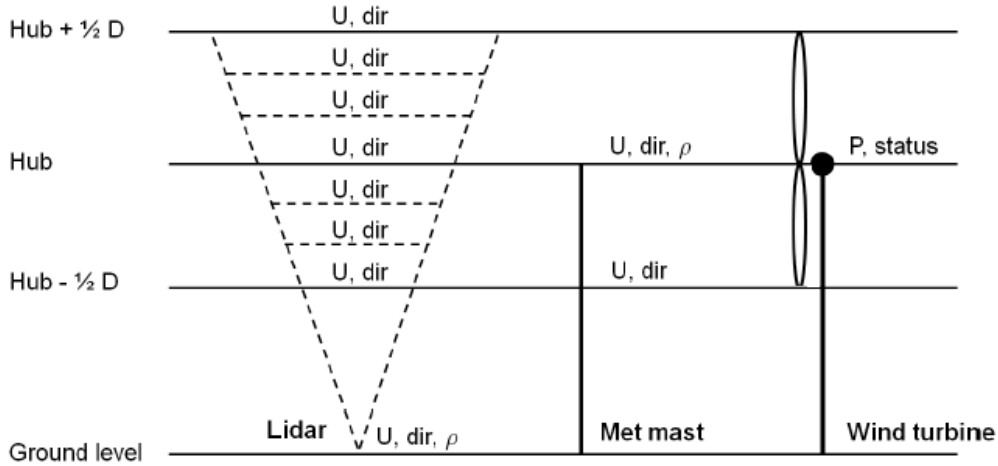
Figure 2.6: Schematic measurement set-up of the Lidar and turbine[51]

should be configured so that a representation can be made of the wind speeds in the rotor area. In the case of a ground-based Lidar, it is easy to define these heights in the Lidar configuration. A schematic measurement set-up of a ground-based Lidar measuring at different heights, a met-mast and a turbine is shown in Figure 2.6.

However, in the case of a nacelle-based Lidar the tilt of the turbine and installation height atop the nacelle should be taken into account. The Lidar should be tilted to compensate the effects of the distance from the Lidar to the enter line of the tower, the distance from the Lidar to the rotor centre and the turbine tilt as function of the wind speed. The optimal Lidar tilt as a result is given in Equation 2.9.[59]

$$\beta_{tilt} = \arctan\left(\frac{h}{xD + L_{cl}}\right) + \beta_{corr} - \beta_{ope} - \beta_{sta} \tag{2.9}$$

Where β_{Lidar} corresponds to the tilt angle which should be implemented during installation for wind speed measurements close to hub height. In addition, h is the height between the optical head of the Lidar and hub height, x indicates the number of rotor diameters, D, and L the distance from the optical head of the Lidar to the tower centre line. Furthermore, β_{corr} corresponds to the correction of the tilt error observed during the Lidar calibration and β_{ope} represents the tilt of the operating turbine at the predominant wind speed. Finally, β_{sta} is the static tilt which is in general negligible small. The tilt of the Lidar can be checked by the readings from the Lidar's inclinometers.

Distance

When using Lidar or met-mast for PCV, the measurements should be performed between 2 to 4 rotor diameters from the turbine according to the IEC. A ground-based Lidar should therefore be placed within this limits, optimally at a distance of 2.5 rotor diameters from the turbine. In the case of a nacelle-based Lidar, this measurement distance can be obtained by configuring the device so that its measurement distances cover the recommended range including 2.5 rotor diameters from the turbine.
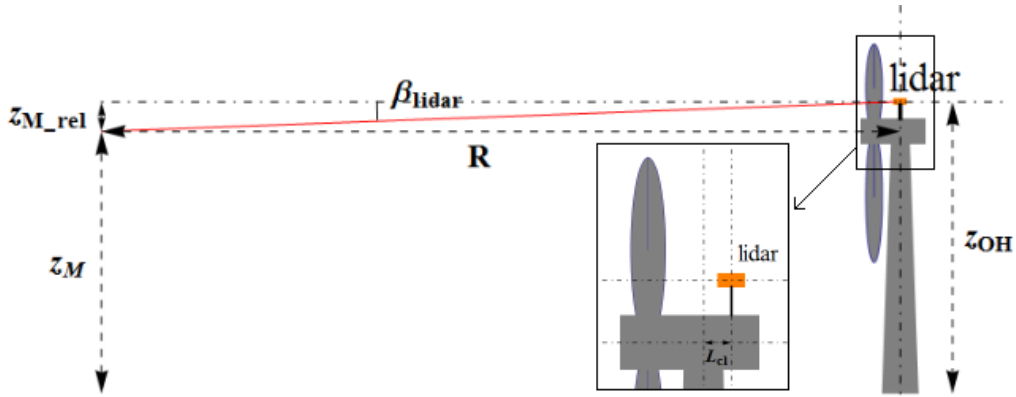
Figure 2.7: Measurement height and distance given the tilt angle and nacelle-based Lidar height[59]

One thing to take into account using nacelle-based Lidar is the tilt angle. From Figure 2.7 the measurement height can be determined with Equation 2.10 including the effect of the tilt angle[59]:

$$z_M = z_{OH} - z_{M_{rel}} = z_{OH} - R \cdot \tan(\beta_{tilt}) \qquad (2.10)$$

where z_M is the measurement height of the Lidar at a measurement range $R \ (= xD + L)$ and z_{OH} represents the absolute height of the Lidar above the ground. As a consequence of the tilt angle β_{tilt} the relative measurement height of the Lidar is $Z_{M_{rel}}$.

2.2 Sonic Spinner Anemometers

Since 2007, Pedersen et al. have investigated the application of spinner anemometers in wind energy[35][36][37]. It was possible to measure power curves with this device, because it could measure the same parameters as a met-mast or Lidar for example. Moreover, Pedersen et al. observed that wind speed measurements of a spinner anemometer correlated better with turbine power than measurements of the nacelle anemometer or met-mast. Also, it was demonstrated that the preferred method to calibrate a spinner anemometer for YM was to deliberately misalign the turbine in stopped conditions.[37]

Since TI measurements with Lidar seem to deviate from met-mast measurements[19], the use of spinner anemometers could evolve new possibilities. Pedersen analysed a spinner anemometer that was calibrated in a sector without wake effects, thus in the absence of high turbulence conditions. The angular and turbulence measurements corresponded well with the met-mast measurements. However, an induction factor correction function was required to correct the wind speed measurements from the spinner anemometer. Moreover, an average YM of approximately 10° was measured which could have been caused by the alternating way in which the two symmetrically mounted spinner anemometers were controlled. The research into the calibration and accuracy of spinner anemometers should be continued to gain more benefits from the spinner anemometers.[35]

(a) 1D sonic anemometer[37]   **(b)** Spinner anemometer[37]
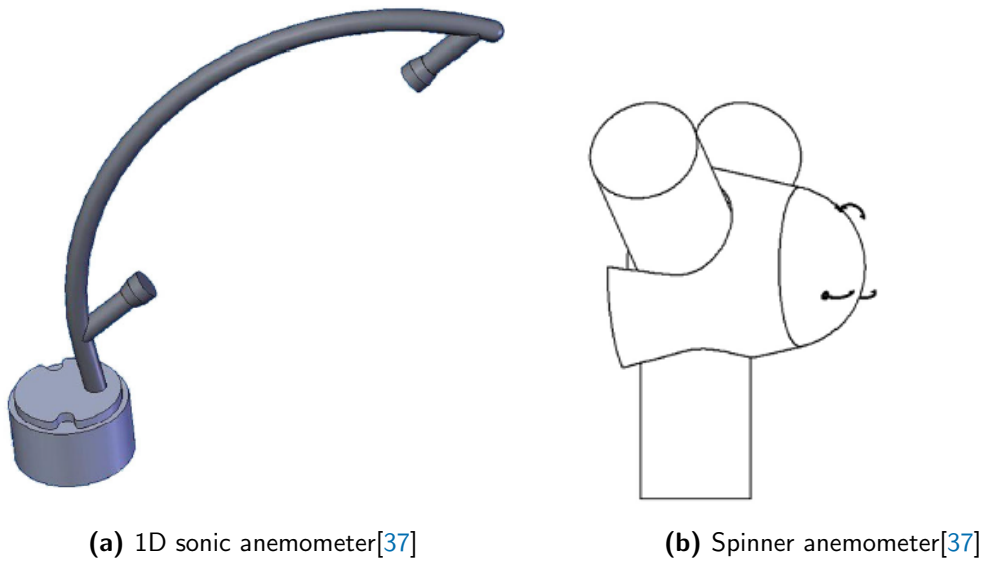
Figure 2.8: Sonic spinner anemometer

Furthermore, Wessels investigated the inclusion of spinner anemometers in wind farms in 2015. The spinner was able to measure wind conditions sufficiently after a calibration with a met-mast[61]. Since the research into the use of Lidar instead of a met-mast in wind farms is going on, the opportunity to calibrate spinner anemometers by using Lidar could be interesting. However, the uncertainty related to the calibration by using a Lidar has not yet been sufficiently examined[17]. Therefore, it has been recommended to investigate the accuracy of the spinner anemometer measurements after a calibration with a Lidar.

To summarise, a spinner anemometer can measure wind speed, YM and flow inclination angle. Also, confidence is given in its ability to measure TI while it is still in debate whether Lidar can measure TI accurately. It is therefore interesting to include spinner anemometers in a field experiment.

2.2.1   Working principle

Different types of spinner anemometers have been applied in research. The spinner anemometer from ROMO Wind is discussed since it was used during the measurement campaign. This spinner anemometer consists of three 1D sonic anemometers (Figure 2.8a) installed symmetrically at the front of the spinner of a turbine as shown in Figure 2.8b. The "Ultrasonic Wind Sensor Technology" is used which works by comparing the time gap between the sound waves going between the two sensors of a sonic anemometer. By combining measurements from the three sonic anemometers, the wind speed, YM and flow inclination angle can be defined with a conversion algorithm which is explained by Demurtas and Janssen[15].[39]

The vector wind speeds can be derived from the sensor wind speeds (V_1, V_2 and V_3) as expressed in Equation 2.11. k_1 and k_2 are algorithm constants that can be obtained from a calibration process which is discussed in subsection 2.2.3. The constants are used to

convert the measurements from the spinner anemometer to the free wind conditions 2.5 rotor diameters in front of the turbine. These constants are related to the design of the turbine spinner and blade roots, so they remain the same for identical turbines if the spinner anemometer is mounted accurately.[37]

$$V_1 = U(k_1 \cos \alpha - k_2 \sin \alpha \cos \theta) \tag{2.11a}$$

$$V_2 = U\left(k_1 \cos \alpha - k_2 \sin \alpha \cos\left(\theta - \frac{2\pi}{3}\right)\right) \tag{2.11b}$$

$$V_3 = U\left(k_1 \cos \alpha - k_2 \sin \alpha \cos\left(\theta - \frac{4\pi}{3}\right)\right) \tag{2.11c}$$

Here, U is the vector wind speed, α the inflow angle and θ the azimuth position where the flow stagnates on the spinner. The parameters discussed above can be obtained from the relations in Equation 2.11 and the coordinate systems in Figure 2.9. The expressions, which represent the conversion algorithm mathematically, are given in Equation 2.12. The expression for θ is clarified in Figure 2.10. The complete derivation is outside the scope of thesis, but can be found in [37].
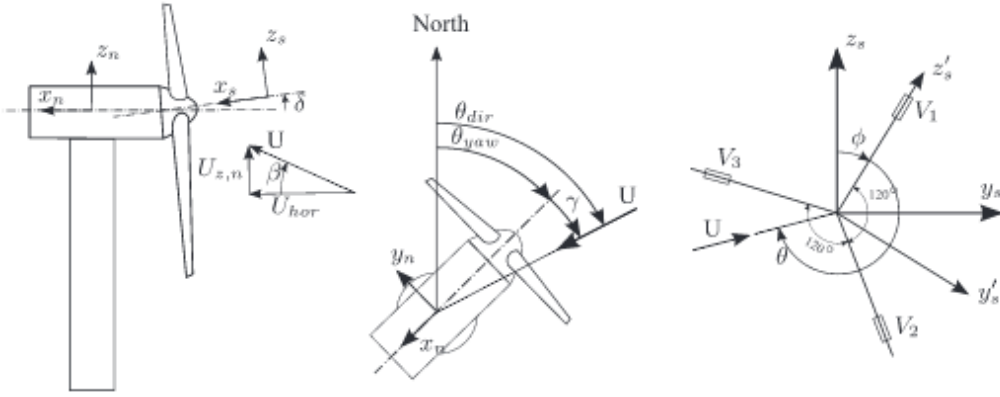
Figure 2.9: Coordinate systems including the relevant angles in a side, top and front view. The subscripts *s* and *n* correspond to the non-rotating shaft and fixed nacelle coordinate systems. The superscript ' corresponds to the rotating spinner coordinate system.[37]

$$V_{ave} = \frac{V_1 + V_2 + V_3}{3} \tag{2.12a}$$

$$U = \frac{V_{ave}}{k_1 \cos \alpha} \tag{2.12b}$$

$$\alpha = \arctan \frac{k_1 \sqrt{3(V_1 - V_{ave})^2 + (V_2 - V_3)^2}}{\sqrt{3}k_2 V_{ave}} \tag{2.12c}$$

$$V_1 < V_{ave} : \theta = \arctan \frac{(V_2 - V_3)}{\sqrt{3}(V_1 - V_{ave})} \tag{2.12d}$$

$$V_1 \geq V_{ave} : \theta = \arctan \frac{(V_2 - V_3)}{\sqrt{3}(V_1 - V_{ave})} + \pi \tag{2.12e}$$
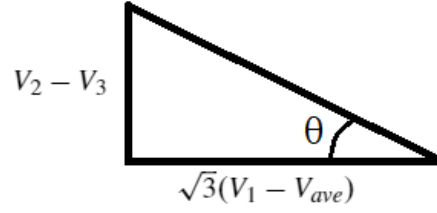
Figure 2.10: θ as function of the vector wind speeds

Subsequently, these expressions can be translated to define the velocity components of the fixed nacelle coordinate system as shown in Equation 2.14[37].

$$u = U(\cos\alpha\cos\delta - \sin\alpha\cos(\phi + \theta)\sin\delta) \tag{2.13a}$$

$$v = -U\sin\alpha\sin(\phi + \theta) \tag{2.13b}$$

$$w = -U(\sin\alpha\cos(\phi + \theta)\cos\delta + \cos\alpha\sin\delta) \tag{2.13c}$$

Where δ represents the shaft tilt angle. Then, the HWS, U_{hor}, and YM, γ, can be determined using the previous expressions:

$$U_{hor} = \sqrt{u^2 + v^2} \tag{2.14a}$$

$$\gamma = \arctan\left(\frac{v}{u}\right) \tag{2.14b}$$

2.2.2   Benefits and drawbacks

The main advantage of spinner anemometers is the measurement location which is in front of the rotor. This means that the flow is not distorted by passing blades for example before it reaches the sensor[15]. Moreover, the rotation results in measurements of the flow angles in absence of mounting and adjustment errors[35].

2.2.3   Installation and calibration

The installation of ROMO Wind spinner anemometers requires specific mounting and calibration steps. First, a standard calibration at zero wind speed or in a wind tunnel should be performed to relate the output readings to the actual wind speed. Secondly, the spinner anemometers should be mounted in front of the rotor, at the spinner of the turbine, 120° apart from each other. The calibration process is continued to include sensor and mounting uncertainties by an internal calibration at the field at wind speeds between 6 and 10 m/s for at least 30 minutes when the turbine is in operating condition. In this step, a first estimate of the calibration constants k_1 and k_2 is made, which are related to the wind speed component parallel and perpendicular to the turbine nacelle direction. The third calibration step is a comparison between the spinner anemometer data and measurements at 2.5 rotor diameters in front of the rotor from a reference measurement device, i.e. met-mast or Lidar. The calibration constants are optimized during this step to account for the turbine geometry.[37]

2.3   Meteorological conditions

The meteorological conditions at a site indicate the wind speed and wind direction distribution during a measurement campaign. Measurements from a whole year are used as input to avoid seasonal variations, which could be used later to estimate the Annual Energy Production (AEP). Therefore, the measurements from the met-mast at hub height, which is in most cases installed at the site for longer than one year, shall be used as input.

One thing to take into account using hub height wind speed measurements from a met-mast, is the distortion of the mast itself on the cup anemometer measurements. At each time, the readings from the cup anemometer that is not behind the mast should be taken.

A wind rose will show the wind speeds distribution over the wind directions. Also, a wind speed distribution will be determined using a Weibull fit. The shape, k, and scale, A, parameters will be estimated using Equation 2.15[26]. In addition, a least-square estimation was done using a Matlab function developed by Bierbooms[5]. This function was based on the method from "Windklimaat van Nederland"[64].

$$k = \left(\frac{std(U_{10min})}{U} \right)^{-1.086} \tag{2.15a}$$

$$A = \frac{U}{\Gamma \left(1 + \frac{1}{k} \right)} \tag{2.15b}$$

Where Γ represents the so-called gamma-function:

$$\Gamma(y) \equiv \int_0^\infty exp(-x) x^{y-1} dx \tag{2.16}$$

2.4   IEC

The IEC provides a procedure to eliminate errors and uncertainties in power performance measurements due to disturbed and inhomogeneous wind conditions. The most relevant guidelines for this thesis will be presented in this section. Additionally, some parts will be discussed in Appendix A.

2.4.1   Developments within the IEC standard

The first edition, which was published in 2005, prescribed cup anemometers for measuring wind speed, since these instruments were robust and suitable for PCV of wind turbines. The second edition was published in 2013 and was focussed on power performance tests using nacelle anemometry. In this case wind conditions are measured on the nacelle. A transfer function is required to estimate the free wind speed from the measurements of the nacelle anemometer. These measurements are less affected by the surrounding terrain and obstacles, but care should be taken of the effects from the turbine's rotor and nacelle.

In 2016 a draft version was released in which remote sensing devices were introduced for measuring wind conditions. The new standard also recommended rotor equivalent wind speed (REWS), because the wind speed at hub height only does not represent the wind speed over the whole rotor height accurately, due to growing rotor diameters. Also, TI affects the averaging of power outputs for which a normalisation procedure is presented in this draft.

To conclude, a general assessment of wind distortions by topographical variations, wind turbines and obstacles should be performed to:

    (a) position the measurement device;

    (b) determine the undisturbed measurement sectors

    (c) check for site calibration requirements

    (d) determine uncertainties caused by wind distortions

Since both measurement campaigns that are discussed in this thesis were performed in a "flat terrain", no site calibration is needed and this section of the IEC standard will be omitted.

2.4.2 Method

Variations in wind shear and wind veer over the rotor area may influence the power curve significantly. As discussed above, the latest version includes REWS measurements for power performance testing. The wind veer is implemented by rewriting the equation for the kinetic energy flux, P_{kin}, through the rotor area (Equation 2.17) so that only the wind speed component perpendicular to the turbine rotor will be used.[22]

$$P_{kin} = \int_A \frac{1}{2}\rho V^3 dA = \int_A \frac{1}{2}\rho(V\cos(\phi - \phi_{hub}))^3 dA \qquad (2.17)$$

Where ϕ_{hub} equals the wind direction at hub height. To implement wind shear, more than three measurement heights are recommended. The REWS is further described in subsection 2.4.9. However, the wind speed at hub height should always be reported, because it has been used as the basis wind speed measurement since the first edition of the IEC standard. Furthermore, in homogeneous terrain the hub height wind speed can give a reliable representation of the wind speed over the whole rotor area.

The wind conditions that are measured by the instruments should be similar to the wind conditions that reach the turbine. If the test turbine or the instrument is in the wake for example, the data should be excluded from the analysis. Thus, the undisturbed measurement sectors should be determined which is further discussed in Appendix A.

In addition, the air density at hub height should be implemented in the calculations. This parameter changes with height, however the effect is negligible in power performance measurements. The procedure to perform air density normalisation of the measurements is described in subsection 2.4.10. Furthermore, TI affects the power curves considerably

due to averaging of the power output and wind speed measurements while there is a non-linear relationship between both parameters as will be discussed in subsection 3.1.1. Therefore, the IEC standard recommends a TI normalisation with a reference TI to eliminate its effect. It allows a comparison between power curves measured at different TI. The reference TI can be defined prior to PCV, as a function of the wind speed at hub height or a 10% value should be used. The procedure for TI normalisation of the power curve will be discussed in more detail in subsection 2.4.12.

2.4.3 Data collection

The data collected by the devices during a measurement campaign should meet some criteria to get power performance characteristics of the wind turbine with sufficient quality and quantity. For example, the wind turbine should operate normally without changing the machine configuration. Any maintenance of the turbines is supposed to be noted. The data from the wind and power measurements "shall be collected continuously at a sampling rate of 1 Hz or higher", while the other parameters like "air temperature, air pressure, wind turbine status and precipitation, if measured, may be sampled at a slower rate, but at least once per minute."[21, pp. 18] The datasets that are to be stored should be based on 10-minute averages of the mean wind speed, its standard deviation, maximum and minimum value.

2.4.4 Data rejection

Since the data requires to be obtained during normal operation and not corrupted, some sets need to be discarded. These sets occur under the following circumstances: external conditions beyond the turbine operating range, turbine is not in operating condition due to faults, a manual shut down, tests or maintenance, failure of test equipment, and when the wind direction is outside the measurement sector or site calibration sector.

2.4.5 Data base requirements

After filtering the data as discussed above, the data should be corrected for air density, wind shear and TI as discussed in the subsequent sections. Then, the database of all collected data should:

- be ordered via the "method of bins" procedure.

- "at least cover a wind speed range extending from 1 m/s below cut-in to 1.5 times the wind speed at 85% of the rated power of the wind turbine."[21, pp. 19]

- have bins of 0.5 m/s with centres as multiples of 0.5 m/s.

- include a minimum of 180 hours of sampled data.

- have bins with at least 30 minutes of sampled data.

2.4.6 Binning procedure

The power curve can be defined by using the "method of bins" as given in equation Equation 2.18[22]. Here, bins of 0.5 m/s are selected for which the mean of the normalised wind speed and power output are to be calculated.

$$V_i = \frac{1}{N_i} \sum_{j=1}^{N_i} V_{n,i,j} \tag{2.18a}$$

$$P_i = \frac{1}{N_i} \sum_{j=1}^{N_i} P_{n,i,j} \tag{2.18b}$$

Where V_i and P_i are the wind speed and power output representing bin i, $V_{n,i,j}$ and $P_{n,i,j}$ the wind speed and power output where j corresponds to the data set and i to the bin, and N_i describes the amount of 10-minute data sets.

2.4.7 Annual Energy Production

The AEP can be calculated with the binned wind speeds and corresponding power outputs using Equation 2.19[22, pp. 43]. In the case of an incomplete power curve up to cut-out wind speed, an extrapolation can be performed from the highest complete wind speed in the database up to cut-out wind speed.

$$AEP = N_h \sum_{i=1}^{N} [F(V_i) - F(V_{i-1})] \left(\frac{P_{i-1} + P_i}{2} \right) \tag{2.19}$$

Where N_h describes the hours in one year and $F(V)$ represents the Rayleigh cumulative probability distribution function as given in Equation 2.20[21, pp. 22].

$$F(V) = 1 - exp \left(-\frac{\pi}{4} \left(\frac{V}{V_{ave}} \right)^2 \right) \tag{2.20}$$

where V_{ave} is the average wind speed from one year data and V the normalised REWS. The average wind speed corresponds in this case to the wind speed at hub height.

2.4.8 Power coefficient

In addition, the power coefficient can be determined for each wind speed bin. It can be calculated with:

$$C_{P,i} = \frac{P_i}{\frac{1}{2} \rho_0 A V_i^3} \tag{2.21}$$

where $C_{p,i}$ is the power coefficient of bin i.

2.4.9 Wind shear correction

Vertical wind shear is described by the difference in wind speed over height. The wind shear coefficient can be calculated with Equation 2.22 using the wind speed at hub height, V_{hub}, and lower tip, V_{low}.

$$a = \frac{\log\left(\frac{V_{low}}{V_{hub}}\right)}{\log\left(\frac{h_{low}}{h_{hub}}\right)} \tag{2.22}$$

A wind shear correction can be applied by three different options: REWS, a wind shear correction factor and a wind shear corrected wind speed. In this thesis only the first option will be used to implement wind shear in PCV. The rotor area is divided into segments derived from the different measurement heights. The corresponding REWS, V_{eq}, is calculated as follows:

$$V_{eq} = \left(\frac{1}{A}\int_i (V_i \cos(\psi_i - \psi_{hub}))^3 dA_i\right)^{\frac{1}{3}} = \left(\sum_{i=1}^{n_h} v_i^3 \frac{A_i}{A}\right)^{\frac{1}{3}} \tag{2.23}$$

where i corresponds to a specific height, v_i is the wind speed at that height, A_i the corresponding area and n_h the number of segments. The segments are separated by a horizontal line in the middle of two measurement heights. The area of a segment can be determined by:

$$A_i = \int_{z_i}^{z_{i+1}} c(z)dz = g(z_{i+1}) - g(z_i) \tag{2.24}$$

where z_i is the height corresponding to segment i and should lie between $H - \frac{D}{2}$ and $H + \frac{D}{2}$, i.e. between the lowest and highest tip height. The rotor width at height z can be calculated with trigonometry:

$$c(z) = 2\sqrt{\left(\frac{D}{2}\right)^2 - (z - H)^2} \tag{2.25}$$

Finally, the integrated function is given by:

$$g(z) = (z - H)\sqrt{\left(\frac{D}{2}\right)^2 - (z - H)^2} + \left(\frac{D}{2}\right)^2 \arctan\left(\frac{z - H}{\sqrt{\left(\frac{D}{2}\right)^2 - (z - H)^2}}\right) \tag{2.26}$$

These steps can be used to calculate the REWS as defined by Equation 2.23. A validation for calculating the segment area using Equation 2.24 can be performed using the theory for calculating circle segments from the on-line computation website *Wolfram Alpha*. This theory uses the circular arc that describes the angle between the two chord points defining the segment.

2.4.10   Air density correction

Air density is a function of temperature, air pressure and relative humidity. As an alternative to the humidity measurement, a value of 50% relative humidity may be assumed if humidity is not measured. These parameters will be used as input to calculate the 10-minute average air density, ρ_{10min}, using Equation 2.27.

$$\rho_{10min} = \frac{1}{T_{10min}} \left(\frac{p_{air,10min}}{R_0} - \Phi p_w \left(\frac{1}{R_0} - \frac{1}{R_w} \right) \right) \tag{2.27}$$

Where R_0 and R_w are the gas constants of dry air (287.05 $J/(kgK)$ and water vapour (461.5 $K/(kgK)$), ϕ represents the relative humidity and p_w the vapour pressure which can be calculated with:

$$p_w = 0.0000205 \cdot \exp(0.0631846 \cdot T_{10min}) \tag{2.28}$$

The temperature should be corrected to hub height with $T_{10min} = T_{meas} + aH$, where T_{meas} corresponds to the temperature measured by the Lidar, $a = -0.0065°/m$ and H represents the height between the Lidar and hub. Furthermore, p_{10min} is the 10-minute average air pressure corrected to hub height using Equation 2.29. An average of the air density that is calculated from the measurements at the site should be used to normalise the data to this reference. Since the turbines in this thesis have active power control, the normalisation given in Equation 2.30 should be applied.

$$p_{air,10min} = p_{meas} \left(\frac{T_{meas}}{T_{10min}} \right)^{-\frac{g_0 M}{R*a}} \tag{2.29}$$

Where M represents the average molar mass of air equal to 0.02897 kg/mole.

$$U_n = \left(\frac{\rho_{10min}}{\rho_0} \right)^{\frac{1}{m}} \tag{2.30}$$

Where U_n is the normalised wind speed. In the IEC standard m was given to be 3, however according to Svenningsen this value results in an overestimation of maximum 5% in AEP. Therefore, an update for this method was proposed such that m:

- equals 3 until wind speeds of 7-8 m/s

- adjusts smoothly from 3 to 1/1.5 when the wind speed goes to 12-13 m/s

- equals 1/1.5 at wind speeds above 12-13 m/s

This update resulted in a reduction up to 1% error in AEP.

2.4.11   Tilt correction

The measurement height of a nacelle-based Lidar can vary when the turbine is operating. This results in bending of the turbine and tilting of the Lidar beams. Since the IEC dictates that PCV is performed with wind speed measurements within 2.5% of the hub height, a nacelle-based Lidar is pre-tilted to measure at hub height on average. In addition, a tilt correction can be applied using the difference between the tilt readings of the inclinometer and their average to calculate the measurement heights with Equation 2.31.

$$h_{Lidar} = h_{hub} + \sin(\beta - \beta_{mean}) \cdot R \tag{2.31}$$

Here, h_{Lidar} is the measurement height of the Lidar, β the tilt angle, β_{mean} the average tilt angle which is assumed to be applied during installation, and R the measurement distance. The measurement height as well as the shear coefficient, a, from Equation 2.22 can then be used as input in Equation 2.32 to calculate the corrected wind speed.

$$V_{hub} = V_{Lidar} \left(\frac{h_{hub}}{h_{Lidar}} \right)^a \tag{2.32}$$

2.4.12   Turbulence intensity correction

Next to the corrections discussed above, a turbulence normalisation has been reported in the IEC standard of 2016. It should be applied to take the TI effect into account, which is caused by averaging of the measured power and wind speed. The correction for TI depends on the TI at hub height as it will represent the TI along the whole rotor area. It will be assumed that the power curve followed by the turbine is independent of TI.

The normalisation only covers the effect of 10-minute averaging. This should result in a power curve independent of TI so that the power curve is corrected for the positive effects at the lower wind speeds as well as the negative effects at the higher wind speeds as discussed in subsection 3.1.1. As a result, the effects of different TI on the turbine performance can be compared. The process is further described in chapter 7.

2.5   Heterogeneity

The Lidar working principle is based on the assumption of homogeneous wind conditions[7]. In statistics, homogeneity relates to the assumption of having the same statistical properties in any part of a data set. This can be translated into wind conditions so that every part of the wind field has the same wind conditions as another part of the wind field. Regarding Lidar, the average wind speed and TI are assumed to be equal between two measurement points so that the HWS and direction measured by both Lidar beams would be equal to the HWS and direction at the centre line over 10 minutes (Figure 2.11a).

In reality a wind field is heterogeneous, so wind conditions will vary through a wind field (Figure 2.11b). Using a Lidar in turbine wakes for instance, where an inhomogeneous flow occurs, leads to uncertainties in the measurements. Cassola et al. investigated the case

(a) Homogeneous   **(b)** Heterogeneous
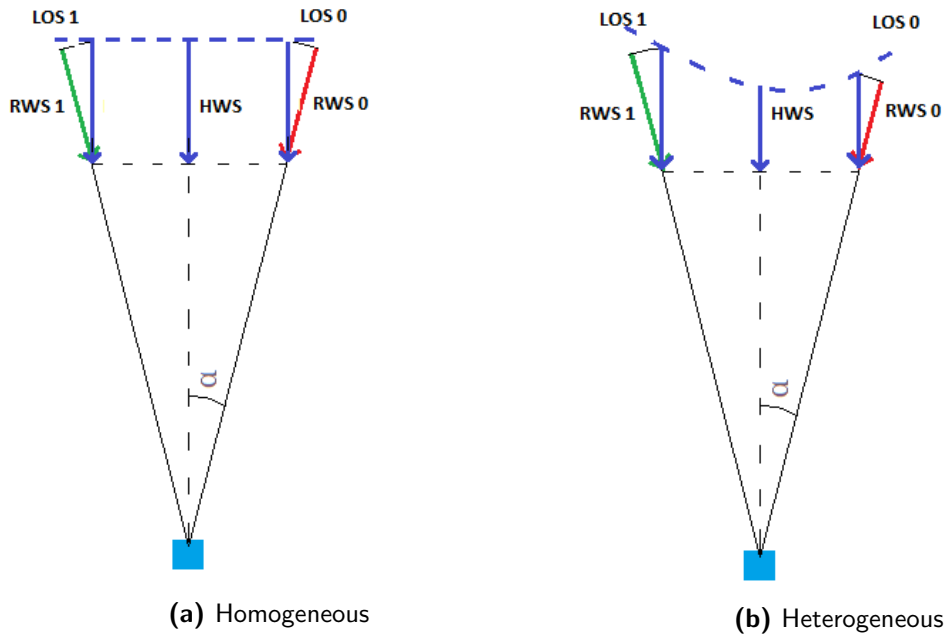
Figure 2.11: Lidar (blue square) measuring in homogeneous and heterogeneous wind conditions

in which a two-beam Lidar measured in free stream conditions, and another Lidar in free stream as well as in wake conditions. Interestingly, it was found that the measurements of both Lidars compared well.[10]

The principle of having different wind conditions in a wind field is further referred as heterogeneity. In this thesis, the effect of heterogeneity on the RWS measured by Lidar will be called X. As discussed above, heterogeneity affects the wind measurements of Lidar because its beams point into different directions. According to this, the accuracy of the Wind Iris in measuring YM as found by Goossens ($\pm 4°$) was questioned by the Lidar manufacturer. With the help of Avent Lidar, Wessels proposed a method to answer the following questions which will be further discussed in chapter 8:

1) How does heterogeneity affect Lidar measurements?

2) Is it possible to compensate for heterogeneity in the future?

2.5.1   Five-beam Lidar measurements

As discussed by Wessels, a five-beam Lidar should be able to measure heterogeneity more accurately than a two-beam Lidar. The data that can be measured by an Avent five-beam Lidar is described in section 5.2. In addition, the Lidar measured in the square configuration. Thus, the only beam that measured at hub height is the centre beam. As a result, the RWS measurements of the other 4 beams should be averaged to be able to determine the HWS and YM at hub height. Consequently, the uncertainty in the measurements will be increased due to this procedure.

Chapter 3

Literature Review

A literature review was performed in order to present an overview of research that has been done on Lidars and spinner anemometers. Also, their ability in measuring the different factors influencing turbine performance were examined. The main applications of Lidar and spinner anemometers will be discussed in the subsequent sections.

3.1 Power curve measurement

A primary characteristic of a turbine is the guaranteed power curve which applies under certain wind conditions. The power curve should be measured during operation for verification and optimisation. According to the IEC 61400-12-1 standard for power performance measurements, a met-mast should be located at a distance of 2.5 rotor diameters from the turbine[21]. The met-mast should contain the following devices: cup anemometers to measure wind speed, wind vanes to define wind direction and air temperature and pressure sensors to determine temperature and pressure. Then, the power curve can be determined from these parameters by following the guidelines in the standard. But, the wind speed at hub height does not represent the wind speed over the whole rotor area, because "the power output of a wind turbine depends on the kinetic energy flux, which itself depends on the wind speed profile, especially for large turbines"[58, pp. 993] as discussed in subsection 3.1.2.

It is expected that Lidar allows for more accurate power curve measurements, since the wind speed can be determined at different heights along the rotor swept area. Moreover, nacelle-based Lidar rotates with the turning turbine which could lead to a more correlated power curve than with cup anemometers or ground-based Lidar. This could also help to determine the effect of YM better as discussed in subsection 3.1.3.

Interestingly, Wagner et al. found a higher correlation between a nacelle-based Lidar and power curve measurements than with a met-mast. Another advantage was the larger usable dataset in the absence of the wake caused by the turbine that is tested. It must be noted that the Lidar tilted backwards when the wind speed was increasing which

resulted in deviations. It was also mentioned that current Lidars are not able to measure in complex terrain accurately due to the assumption of having homogeneous wind speed in horizontal direction.[60]

Recently, van der Velde investigated the difference in AEP between Lidar and met-mast measurements. A difference of 2.5% in AEP was found from measurements with a mean wind speed of 7 m/s and a Rayleigh distribution. He concluded that a comparison of power performance between turbines can be made with either a met-mast or Lidar, but not using a combination of both measurement devices.[51]

Regarding the guaranteed power curves, the specific wind shear and TI conditions under which they are typically guaranteed include shear exponents of 0.15-0.2 and TI of 10-12%, which are also referred as the "inner" conditions[49]. As a result, a significant amount of data could be excluded. For instance, 70% of met-mast data from a measurement campaign (February 3, 2015 until July 7, 2015) at Prinses Alexia wind farm had to be excluded[61]. This means that during 70% of the available time no power curve was guaranteed, i.e. the turbine was operating in the outer conditions. A similar result was found with a Lidar at Prinses Alexia wind farm by van der Velde where 41% of the data was collected during inner conditions. The effect of the filter for inner conditions was an increase of 0.8% in power performance[51]. This means that it can be valuable to demand power curves valid for (part of) the outer conditions.

As discussed above, power curves are guaranteed for a limited range of TI and wind shear conditions. To get a more refined overview of the turbine performance, the turbine manufacturer should guarantee power curves for more variable TI and wind shear conditions. The demand for strict guarantees in future contracts from wind farm operators such as Vattenfall raises, since it will result in more certainty. This requires also measurement devices that can accurately measure TI and wind shear to be able to monitor the turbine performance. To conclude, Lidar's ability to measure wind shear and TI is important for PCV. The effects of these parameters on turbine performance are discussed below.

3.1.1   Turbulence intensity

A turbine wake, complex terrain or high shear results in turbulent flow conditions which affect the turbine performance and loads on the turbine negatively. Quite a lot of research has been carried out on this topic[19][27][51][53][57][61], but the question whether Lidar can measure TI accurately is still in debate.

Following the research by Kaiser et al., TI affects the turbine performance such that "with increasing turbulence intensity the power output will be underestimated at rated wind speed and overestimated near cut-in wind speed"[27, pp.160]. This is caused by two factors as described by Villanueva Lopez: *bin-averaging* and *relaxation*. Turbulence leads to a higher power output at lower wind speeds, because in this region the power output increases with the wind speed cubed. This means that a similar increase as decrease in wind speed caused by turbulence results in a higher power output on average. However, at higher wind speeds the power curve slope is decreasing, which results in a contrary effect of TI on the power curve. Thus, the average power output in a specific wind speed bin cannot be representative for all data points in that bin. The second factor, relaxation, has a similar effect and is defined by the change in power output by inertia effects. At

rated wind speed, a maximum power output is achieved, thus a higher wind speed caused by turbulence does not result in a higher power output. A similar decrease in wind speed does result in a lower power output, and therefore this factor leads to a lower power output by 10-minute averaging. These effects will increase with a higher TI[53], which is shown in Figure 3.1.
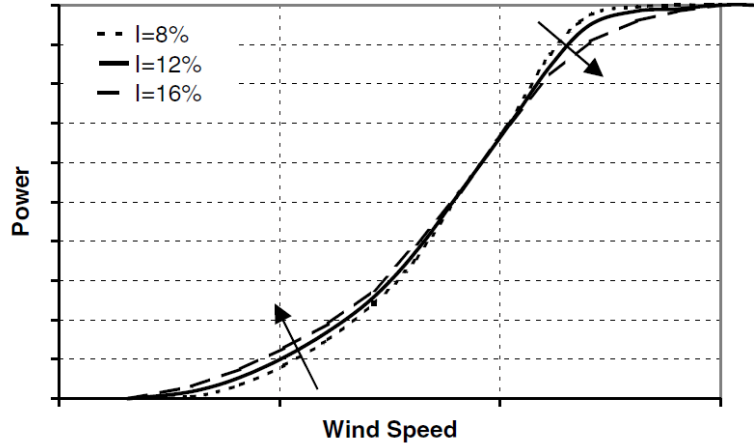
Figure 3.1: Effect of TI on power curve[27]

One thing to take into account when comparing TI measurements, is that the Lidar measures differently than a met-mast. For example, a two-beam Lidar takes the average TI of the measurements, which is considered as volume averaging, whereas the cup anemometer takes point measurements. Also, the two beams have different orientations as a result of the opening angle. These could be the main causes of the difference in the turbulence measurements between a Lidar and a met-mast.

Interestingly, Pedersen investigated the TI evolution with a met-mast and spinner anemometers. One of the advantages of spinner anemometers is that they measure the undistorted flow, because the spinner anemometers are located in front of the rotor. The following relation between the TI measurements was obtained: $TI_{spinner} = 1.11 \cdot TI_{met-mast}$. After applying a correction for the induction, the TI measured by the spinner anemometers correlated well with the met-mast.[35]

3.1.2 Wind shear

Besides the possibilities to measure TI with some uncertainty, it is also possible to determine wind shear with Lidar due to its ability of measuring at different heights (ground-based Lidar or two-beam nacelle-based Lidar). Shear causes a change in wind speed with change in height. Measurements should be taken at two different heights to calculate the wind shear. Wagner et al. demonstrated that using wind speed measurements at more points in the rotor swept area instead of only at hub height reduced the scatter in the power curve[56]. Subsequently, Wagner et al. suggested the implementation of the rotor equivalent wind speed into the power curve, because the difference between the wind speed at the minimum and maximum height of the rotor swept area due to wind shear will increase with bigger turbines.[58]

3.1.3   Yaw misalignment

In addition, wind direction, or YM in case of a nacelle-based Lidar, is one of the parameters that can be measured by Lidar, which is crucial for the alignment of the turbine with the wind to capture the maximum power available from the wind. Since a nacelle-based Lidar turns with the rotor axis and profiles the wind coming towards the turbine, it can be a suitable device for measuring YM.

Recently, the accuracy of a Wind Iris in measuring YM and power curves was investigated at wind farm Slufterdam by Goossens. Also, the effect of YM on the turbine performance was discussed. The relation between power loss and YM was expected to be a derivation from the misalignment of the rotor swept area with the wind ($A_{proj} = A \cdot \cos(\gamma)$). However, a more realistic relation was found from literature to be cos^2, which could be due to the flow component that is misaligned with the direction perpendicular to the rotor[38].

Following the straight-forward power equation and change in yaw angle of the turbine alignment with the wind equal to γ gives the following relation for maximum available power[29]:

$$\tilde{P}_{max} = \frac{1}{2}\rho A(U\cos^3(\gamma))C_P \tag{3.1}$$

where ρ is the air density, A the rotor area, U the free wind speed and C_P the power coefficient. From this relation can be seen that the power will be reduced by a factor of cosine cubed. Then, a root mean square YM of $10°$ results in a power loss of 4.6%[32]. Moreover, Fleming et al. stated that the relation depends on the aero-elastic properties of the turbine[18]. Nevertheless, YM leads to power loss and to limit this, a suitable device to measure it and a good control system to correct for it are required.

Following the research by Goossens, the Lidar was able to measure the power curve reliably, but a higher uncertainty than expected, $4°$ instead of $0.5°$, in YM was found. Furthermore, it was recommended to misalign the turbine intentionally between values of $-25°$ and $25°$ to determine the impact of YM on the power curve[19]. This experiment has been simulated with a varying YM from $-20°$ to $20°$ for wind speeds ranging from 4 to 25 m/s by Wessels. During the simulations the wind shear was set to 0, and the YM changed in steps of $0.5°$. From Figure 3.2 can be seen that an increasing YM leads to a reduction in the power curve as expected. Besides that, Wessels determined the effect of wind shear on the ideal yaw error by doing Bladed simulations with varying wind shear exponents (0, 0.2, 0.4 and 0.5) and smaller steps in YM of $0.25°$ from $-1°$ to $2°$. It was found that increasing wind shear results in a higher ideal yaw error ($0°$ for wind shear exponent equal to 0, $1°$ for 0.5), however this increase was considered to be negligible.[61]

To investigate this hypothesis from the simulations, the data set from Prinses Alexia was investigated with Boorsma's method. An ideal yaw error of $2.5°$ was detected for an increase in the wind shear exponent from 0.1 to 0.5. This value is significant higher than obtained from the simulations, but it is in agreement with the positive yaw error as expected for higher wind shear. Furthermore, it was concluded that the Lidar can measure YM accurately, but cannot be applied in PCV due to a high uncertainty in the measurement campaign. Finally, the recommendation of Goossens to misalign a turbine intentionally was processed into a proposal.[61]
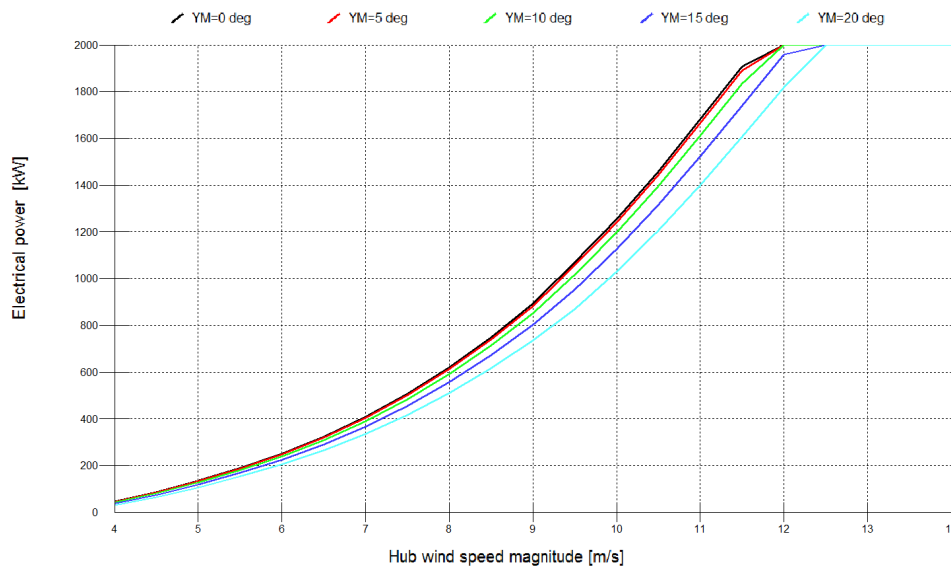
Figure 3.2: Power curves generated by Bladed with varying YM[61]

To summarise, measuring YM with Lidar should be further investigated. For example, spinner anemometers could help to validate the YM measurements in the consecutive research. In addition, an experiment with an intentionally misaligned turbine can be performed. This could demonstrate the effect of YM on turbine performance.

3.1.4 Wake research

Wake effects reduce the power output of downwind turbines[31] and affect the loads negatively[23]. Therefore, understanding the wake field can help to quantify deficits and extra structural loads in wake environments. To measure in the wake continuously, nacelle-based Lidar can be applied to look downwind. This could be interesting to monitor the wake and estimate its effect on downwind turbines in a wind farm for example.

Iungo and Porté-Agel demonstrated that wind turbine wakes should be taken into account for advanced wake models to minimise wake interactions and to optimise the power output. The wake of a utility-scale wind turbine (Enercon E-70 2 MW) under real atmospheric conditions was analysed by one Lidar that measured upwind flow conditions and two Lidars that measured 3D volumes downwind by changing the horizontal and vertical measurement angles continuously. The Lidars were deployed in the wake of the turbine at twelve rotor diameters away from the turbine. As can be seen from the measured velocity fields shown in Figure 3.3 and Figure 3.4, the deficits in wind speed reduce and the wake widens slightly moving downstream. Furthermore, it was found that "wind turbine wake recovers faster under convective conditions, compared with the neutral ones"[24, pp. 9-10]. This can be explained with the higher TI conditions in the atmospheric boundary layer (ABL) so that the mixing of ABL and turbine wake increases resulting in wake recovery.[24]

In recent years, the use of Large Eddy Simulations (LES) has increased for studying wind turbine wakes since it is thought that it would improve the turbulence evolution. The
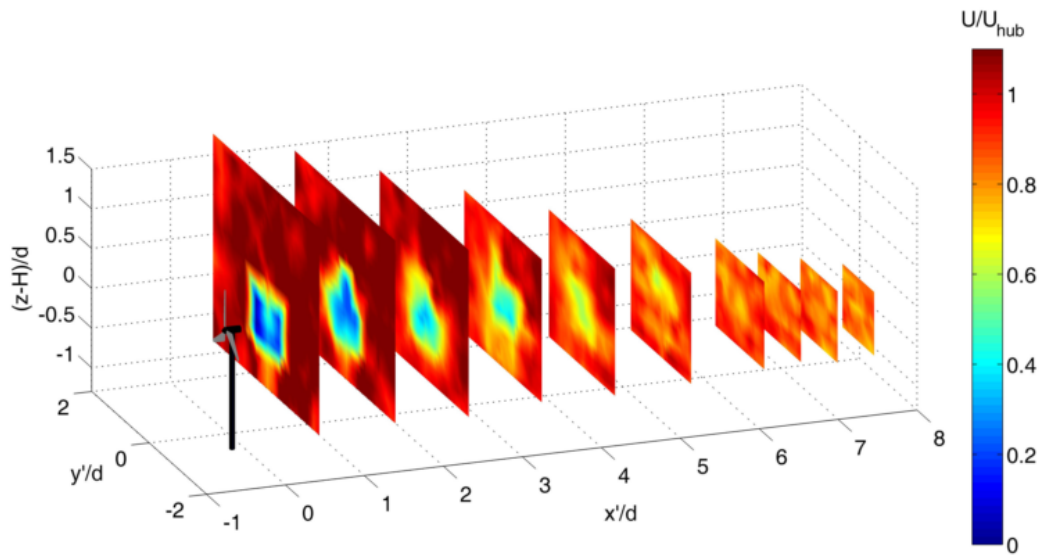
Figure 3.3: Velocity field at several distances downwind of the turbine[24]

main reason behind this thought is the potential to compute larger scales of turbulent motion and temporal information[25].

3.2 Wind turbine control

It is important to control a turbine sufficiently in order to reduce fatigue and extreme loads, but also to improve its efficiency. For instance, this can be done by preventing unnecessary emergency shut-downs due to over-speeding (feed-forward control) or aligning with the wind direction (yaw control). This means that the wind conditions upwind of the turbine, which are used as input for the controller, should be measured accurately.

Many different Lidar systems have been developed, but not particularly focused on control applications. Bossanyi et al. analysed several Lidar systems by simulation modelling and reported the most important characteristics of Lidar to be used in control applications. Besides that, it was found that a nacelle-based Lidar is able to improve collective pitch control, since it can measure wind conditions that will reach the turbine a few seconds later.[9]

3.2.1 Feed-forward control

Nacelle-based Lidar has been extensively investigated and used successfully for wind turbine control[32][42][43]. Schlipf et al. examined new control methods in which Lidar measurements were used as input. First, a non-linear model predictive controller was compared to a baseline controller. The controllers were tested by simulating gusts and turbulent wind fields from which 50% and 30% reductions resulted for extreme gusts and for lifetime fatigue loads.[42]
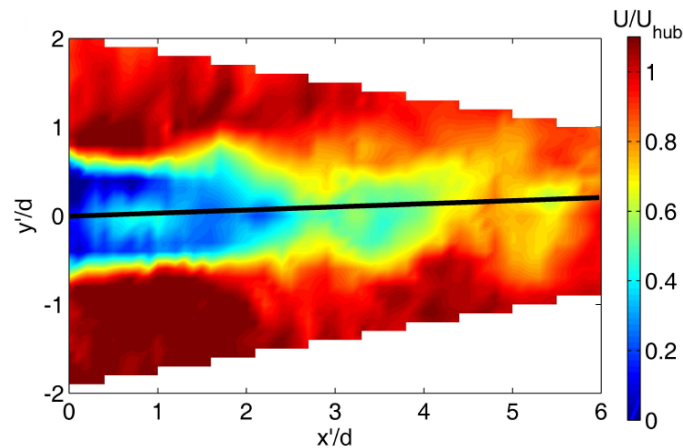
Figure 3.4: Velocity field at several distances downwind of the turbine over the horizontal plane[24]

However, the simulations do not fully represent the real conditions. Therefore, Schlipf et al. performed a field test in which a feed-forward collective pitch control was examined using a nacelle-based Lidar. In accordance with the simulations, reductions in the turbine loads ($\geq 10\%$) and in the pitch activity were accomplished[43].

3.2.2   Yaw control

As discussed in subsection 3.1.3, it is important to align a turbine with the wind direction. In 2014, Fleming et al. examined the use of a nacelle-based Lidar (Wind Iris) for improving the power capture. First, a significant difference in the wind vane anemometer measurements of 7.5° on average was observed by performing a measurement campaign of one month in normal operation with a nacelle-based Lidar and from this an error correction value was determined and implemented into the yaw controller. Hereafter, a field test was performed in which the effect of the correction on the power capture and loads was investigated. The results showed an increase of 2.4% in AEP and some positive and negative effects on loading. Finally, it was concluded that using a nacelle-based Lidar for correcting YM improves the turbine performance[18]. A field test conducted by Scholbrock et al. showed similar results in yaw correction and its effect on power capture[44].

3.3   Conclusions

Since 2006, the applications of Lidar have been investigated in the field of wind energy. Recently, the nacelle-based type of Lidar has emerged as potential measurement device for particularly site assessment and PCV. Previous research has not presented concluding results on TI effects and heterogeneity. However, power curve measurements, wake research and YM calculations have been done reliably. Although a few of these investigations were performed at wind farms of Vattenfall, gaining more experience in these measurements is valuable.

Chapter 4

Research Setup

This chapter discusses the sites at which measurement campaigns are performed as well as the simulation tools that were used. Also, the measurement instruments and the turbines under research are described.

4.1 Prinses Alexia

The first field test was performed at wind farm Prinses Alexia, which is located in the Dutch Flevopolder close to Zeewolde, the Netherlands, as shown in Figure 4.1. The wind farm is owned by Vattenfall and consists of three rows with each 12 Senvion 3.4M104 turbines. The measurement devices that were installed in the wind farm, which is depicted in Figure 4.2, are a ground based Lidar and met-mast. A list of the turbine specifications is given in Table 4.1.

Figure 4.1: Location of wind farm Prinses Alexia
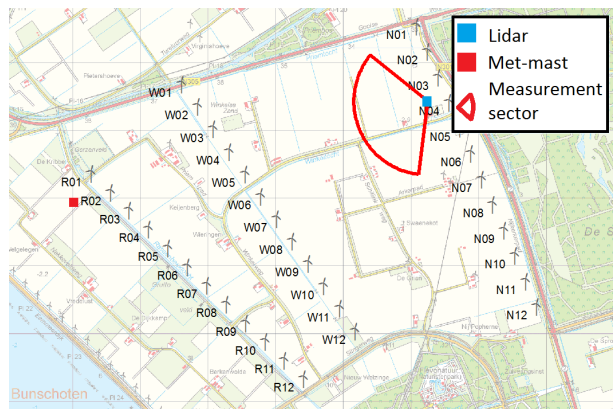
Figure 4.2: Site layout of wind farm Prinses Alexia

Table 4.1: Turbine specifications of wind farm "Prinses Alexia"

Parameter	Value
Type	Senvion 3.4M104
Hub height	98 m
Rotor diameter	104 m
Rated Power	3.37 MW
Rated wind speed	13.5 m/s
Cut-in, cut-out wind speed	3.5 m/s, 25 m/s

4.1.1 Ground-based Lidar

The type of Lidar that was installed is a cw Doppler Lidar from ZephIR. This Lidar, which is depicted as a blue square in Figure 4.2, was installed on the ground near turbines N03 and N04, 5 km east of the met-mast. The device was configured to measure at the following heights: 10, 38, 45, 55, 76, 97, 117, 138, 149, 174 and 199 m. It measured wind speed, wind direction, wind speed standard deviation and TI directly. The Lidar also contained a meteorological station which provided measurements of temperature, pressure and humidity. The measurements were sampled at 50 Hz and each second the averages were logged.[65]

Since the Lidar can measured at different heights, the measurements can be used to calculate wind shear or REWS. The ability of Lidar to measure TI accurately is not yet determined. TI can also be calculated with Equation 4.1 as function of wind speed and standard deviation. This results in a different TI compared to the measurements. However, the value measured by the Lidar was corrected by implementing a factor in the Lidar system, which was based on a comparison with TI measurements from a met-mast as discussed in subsection 5.1.5.

$$TI = \frac{\sigma}{\mu} \tag{4.1}$$

4.1.2 Measurement sector

For this location, the measurement sectors were determined for the Lidar and turbines to be investigated by using the method of the IEC[22], which was explained in section 2.4. First, all turbines in the surroundings were listed. The distance to the turbines to be investigated and to the Lidar were measured. Also, their dimensions, height and diameter were determined. Then, using the procedure in section 2.4 the undisturbed sectors were determined. For both turbines in addition to the Lidar, the undisturbed sector covered a range from 187° up to 306° as shown in red in Figure 4.2.

4.1.3 Measurement campaign

The Lidar was installed at its second location the 13th of January in 2016 while the met-mast has been in operation since January 2015. Since the met-mast is located 5 km away from the Lidar a validation with the met-mast for the Lidar measurements will be unreliable. Therefore, the nacelle anemometers at the two turbines under investigation

were used to validate the measurements which is shown in chapter 5. The data of the measurement campaign is limited by the measurement period of the Lidar, so it ranges from the 13$^{\text{th}}$ of January until the 17$^{\text{th}}$ of April in 2016.

4.1.4 Data

The data from the Lidar, met-mast and wind turbines was collected via different sources. For example, the turbine data was obtained from the Wind Power Data Center (WPDC) of Vattenfall, which is supplied by the Supervisory Control And Data Acquisition (SCADA) system of the wind farm. The turbine data contains turbine parameters as well as wind conditions. Wind Consult collected the met-mast data and provided it to Vattenfall. Finally, the Lidar data collection was arranged by Ecofys and also sent to Vattenfall.

Each measurement contains a time stamp, but the measurement devices measured in different time zones. Therefore, the data sets will first be synchronised to the same time zone. When at least one of the data parameters, which are considered, from the devices is missing for a specific time stamp, the data set that belongs to this time stamp will be neglected. The synchronisation of all data will be presented in subsection 5.1.1.

4.1.5 Meteorological conditions

The meteorological conditions during the measurement campaign at Prinses Alexia are shown in Figure 4.3a and Figure 4.3b. The Weibull distribution estimated with the least-square method results in $k = 2.09$ and $A = 8.00$. Looking at the Weibull fit using the method of Justus[26], it seems to fit the histogram better with $k = 2.17$ and $A = 8.04$. The prevailing wind direction at this site is from South-West, which was also found by van der Velde[51] and Wessels[61]. Furthermore, the mean wind speed and wind direction at Prinses Alexia are 7.12 m/s and 196° respectively.

4.1.6 Validation approach

A validation had been performed during a measurement campaign at Prinses Alexia where the Lidar was installed close to the met-mast by van der Velde. The measured parameters that were compared between the met-mast and Lidar are the wind speed, wind direction, air density and TI.

The wind speed validation was based on the Norsewind criteria because of its frequent use in the field of wind energy[20]. It was found that the Lidar underestimates the wind speed slightly, but the regression also showed high correlation. The air density comparison showed worse correlation, but the power performance test is less affected by this parameter. Furthermore, an offset of 180° in the wind direction measurements of the Lidar occurred during some periods. This was caused by the fact that Lidar measures only the magnitude of the LOS velocity without its direction. An adjustment was made using the met-mast measurements to remove this offset resulting in a good fit. On the other hand, large scatter was observed in the TI comparison.[51]

(a) Wind speed distribution   **(b)** Wind rose
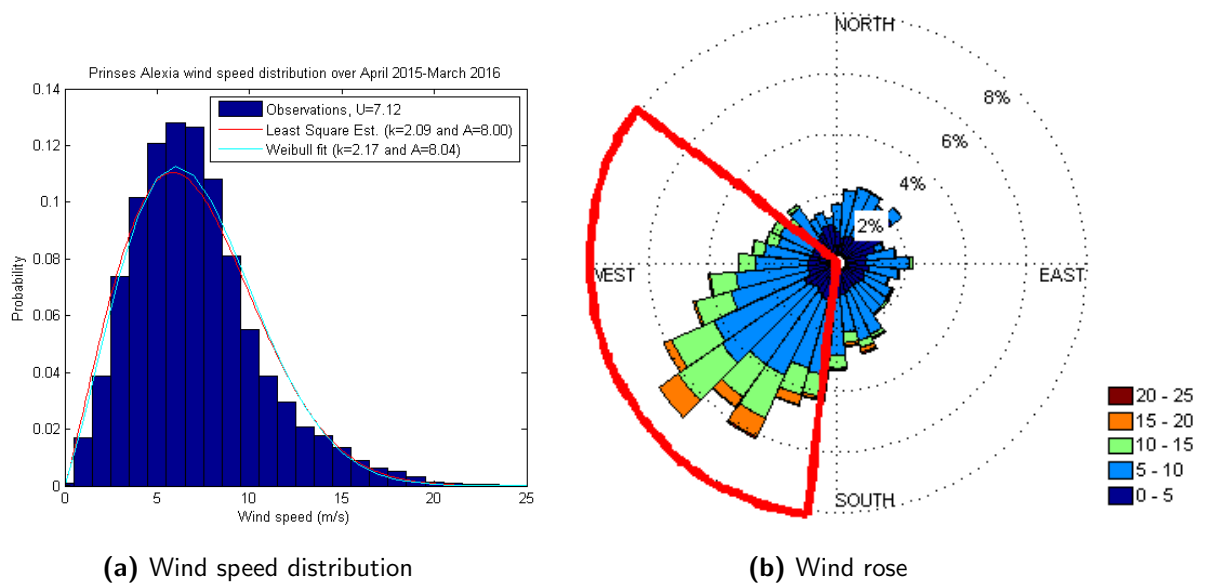
Figure 4.3: Meteorological conditions at Prinses Alexia

In this thesis, a brief validation is performed by comparing the Lidar measurements to the nacelle anemometers at the turbines due to the distance between the Lidar and met-mast. The validation is done by comparing wind speed, wind direction, air density and TI measurements of the Lidar with turbine data. Also, met-mast measurements are used to check errors. The results of the validation are discussed in section 5.1.

4.2   Nørrekær Enge

The second field test was performed at wind farm Nørrekær Enge, which is located in Northern Jutland, Denmark, as shown in Figure 4.4. The wind farm is owned by Vattenfall and consists of 13 Siemens SWT 93 2.3MW turbines. The measurement devices that were installed at the farm, which is depicted in Figure 4.5, are two nacelle-based Lidars, 13 sets of spinner anemometers and a met-mast. The nacelle-based Lidars were installed on turbine 4, which is close to the met-mast. The specifications of the turbines are given in Table 4.2.

Table 4.2: Turbine specifications of wind farm "Nørrekær Enge"

Parameter	Value
Type	Siemens SWT 93 2.3MW
Hub height	80 m
Rotor diameter	93 m
Rated Power	2.3 MW
Rated wind speed	13-14 m/s
Cut-in, cut-out wind speed	4 m/s, 25 m/s

Figure 4.4: Location of wind farm Nørrekær Enge
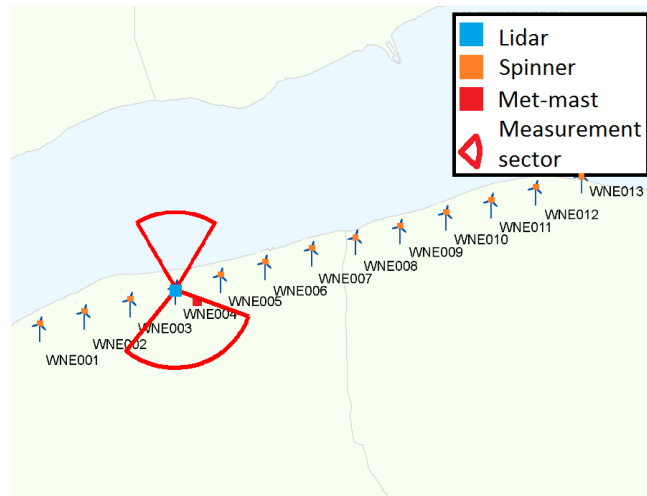
Figure 4.5: Site layout of wind farm Nørrekær Enge

4.2.1 Nacelle-based Lidar

A ZephIR Dual Mode in combination with an Avent five-beam Lidar were installed on the 22nd as wind measurement devices at turbine 4, which are depicted as a blue square in Figure 4.5. The Avent five-beam Lidar was configured to measure at the following ranges: 10, 20, 30, 40, 50, 60, 80, 100, 120 and 140 m. The ZephIR Lidar measured at: 10, 30, 95, 120 and 235 m. The Lidars collected wind speed, direction, wind speed standard deviation and TI measurements directly. The ZephIR Lidar also contained a meteorological station which provided measurements of temperature, pressure and humidity.

4.2.2 Spinner anemometers

Spinner anemometers were installed in August 2014 at turbine 4 and in October and November 2014 at the rest of the wind turbines of the wind farm. The type of the installed spinner anemometers are ROMO Wind sonic spinner anemometers. The spinner anemometers measured wind speed in front of the rotor, YM and TI. They also contained a meteorological station to determine air temperature and pressure from which air density was calculated.

4.2.3 Measurement sector

The wind farm is mainly surrounded by farm land and water. In this case, only the disturbance by other wind turbines have to be considered. The wind turbine to be investigated is turbine 4, since the Lidars were installed at this turbine. This turbine as well as the met-mast should not be in the wake of other turbines. Also, the Lidar beams which measure at several ranges in front of the turbine, as displayed in Figure 4.6a and Figure 4.6b, should not be in the wake of other turbines. Therefore, the measurement sectors determined by other turbines affecting turbine 4 according to the IEC standard should be adjusted.

(a) ZephIR DM Lidar   **(b)** Avent five-beam Lidar
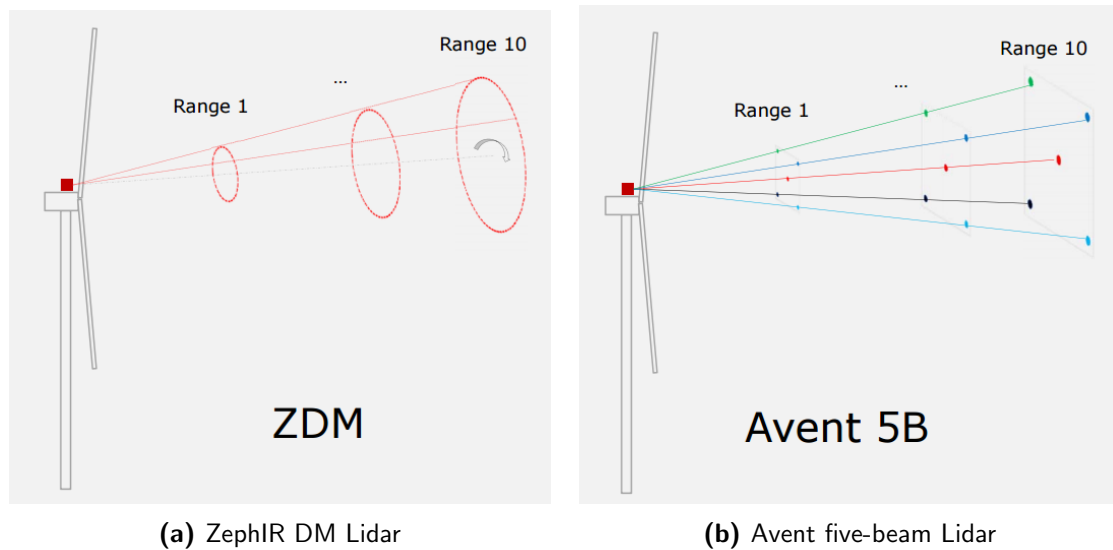
Figure 4.6: Lidar profile ranges in front of turbine[52]

Wessels determined the measurement sector to be between 95° and 225° and 330° and 30°. From the lay-out in Figure 4.5 can be seen that the Lidars on top of turbine 4 will be less affected by the wind turbines next to the turbine under investigation in the sector between 330° and 30° than between 95° and 225°. This was confirmed by Slinger, who determined the southern measurement sector to be between 110° and 219°. To conclude, the latter in addition to the sector between 330° and 30° will be considered as undisturbed measurement sectors.

4.2.4   Measurement campaign

The Lidars were installed on the 22nd of May in 2015 while the met-mast has been in operation since October 2014. The spinner anemometers have been operating since 2014, but no data is available from May 2015 until the end of August 2015. The measurement campaign is limited to the available data from all measurement devices and ranges from 1 September 2015 until 6 January 2016.

4.2.5   Data

The data was collected via similar sources as for the measurement campaign at Prinses Alexia. However, the data from the spinner anemometer was provided to Vattenfall from ROMO Wind. The data sets were first synchronised to the same time zone and missing data was reported. The detailed synchronisation will be presented in subsection 5.2.2.

As in the case of Prinses Alexia, the data sets will first be synchronised to the same time zone. Also, when at least one of the data parameters, which are considered, from the measurement instruments and turbines under research is missing for a specific time stamp, the data set that belongs to this time stamp will be removed.

(a) Wind speed distribution **(b)** Wind rose
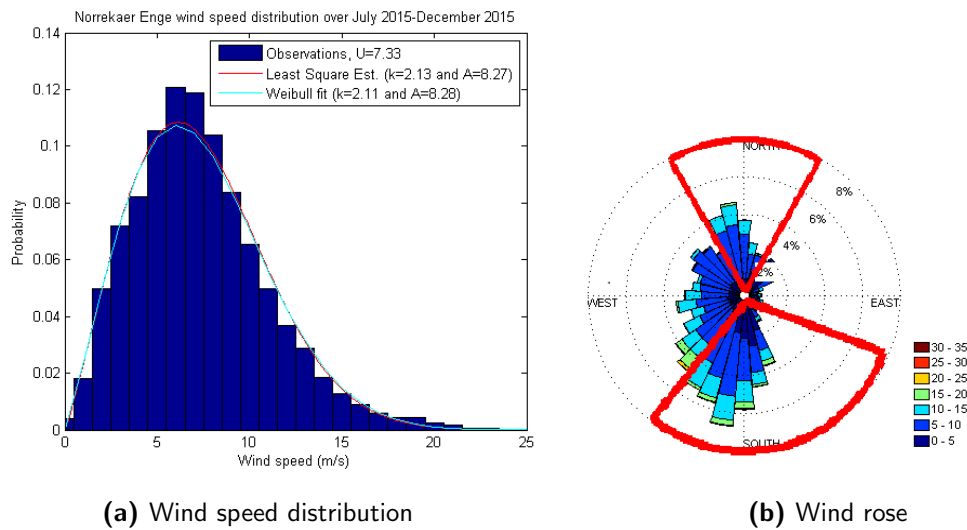
Figure 4.7: Meteorological conditions at Nørrekær Enge

4.2.6 Meteorological conditions

The meteorological conditions at Nørrekær Enge are shown in Figure 4.7a and Figure 4.7b. The conditions are based on met-mast measurements from July 2015 until December 2015, because no data was available from a whole year. During this measurement period a mean speed of 7.33 m/s was obtained and the prevailing wind came from South-West direction. It is assumed that the wind distribution can be a described by a Weibull fit which was estimated by the least-square method. From this method was obtained that $k = 2.13$ and $A = 8.27$. Another fit was made using the method of Justus[26] which compared well with the least-square method ($k = 2.11$ and $A = 8.26$).

4.2.7 Validation approach

A validation will be performed for the measurement campaign at Nørrekær Enge. The measurements of the following devices should be validated: ZephIR DM Lidar, Avent five-beam Lidar, ROMO Wind spinner anemometers as well as instruments on the met-mast and turbines. The following parameters measured by the met-mast, Lidars and spinner anemometers will be compared to each other: wind speed, wind direction or YM, air density and TI.

4.3 Simulation tools

In this section, the simulation tools which were used for the research are discussed.

4.3.1 Matlab

A general *Matlab* code was written to function as basis for all the outputs that had to be generated. The general data flow of this code is shown in Figure 4.8. First, the data
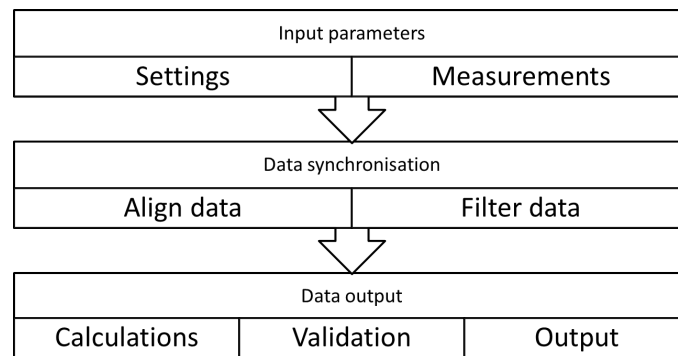
Figure 4.8: Data flow

obtained via different sources as discussed in subsection 4.1.4 and subsection 4.2.5 were implemented. Also, relevant parameters such as wind turbine dimensions were determined as settings. Hereafter, the data from the different sources were to be synchronised. When all data sets were aligned with each other using the same time zone, the data was filtered according to section 2.4 depending on the purpose of the calculations. Finally, calculations and subsequently validations could be performed. These were used to support the outputs of PCV for example.

4.3.2 Bladed

To investigate the effect of heterogeneity on Lidar measurements, an analysis was performed with a synthetic wind field generated by *GH Bladed* from DNV-GL. This wind turbine modelling tool is primarily developed to optimise turbines during the design phase. As part of this tool, a 3D turbulent wind field can be generated. The generated wind field was used as input in Matlab via a conversion tool made by Bierbooms.

A wind field was created using the wind turbine dimensions of Nørrekær Enge to make a comparison with the measurement data possible. The process is further described in section 8.2.

Chapter 5

Validation

Data validation is performed before analysing data to maintain reliability. The validation consists of data synchronisation and filtering for disturbed or incorrect measurements. Also, the wind speed, wind direction or YM, air density and TI measurements will be analysed. The wind farms which are analysed in this thesis will be discussed separately.

5.1 Prinses Alexia

The validation for Prinses Alexia consists of data alignment and comparisons between Lidar and turbine data of wind speed, wind direction, air density and TI. When it is needed, the measurements from the met-mast are used to compare with. It should be mentioned that the wind speed measurements of the Lidar are first corrected according to the validation of van der Velde, who found that the Lidar measured the wind speed with a factor of 0.989 lower in comparison with the met-mast that is located at Prinses Alexia.

5.1.1 Data alignment

The first step in processing all data is to align the data sets. The Lidar data was collected in the Coordinated Universal Time (UTC) time zone whereas the met-mast data had time stamps in the UTC+1 zone. On the other hand, the turbine data was collected with time stamps of the local time such that the shift to the summertime had to be incorporated. Since all data was synchronized with the UTC time, only the met-mast data was shifted. Consequentially, the time stamps of the met-mast, recorded as the middle of a time interval instead of the beginning, were neglected.

It was also observed that time stamp "06-Mar-2016 10:10:00" was not chronically ordered. This revealed missing Lidar measurements from "05-Mar-2016 22:30:00" until "06-Mar-2016 10:00:00" and from "06-Mar-2016 17:20:00" until "07-Mar-2016 09:00:00". The

(a) Complete period   **(b)** Partial period
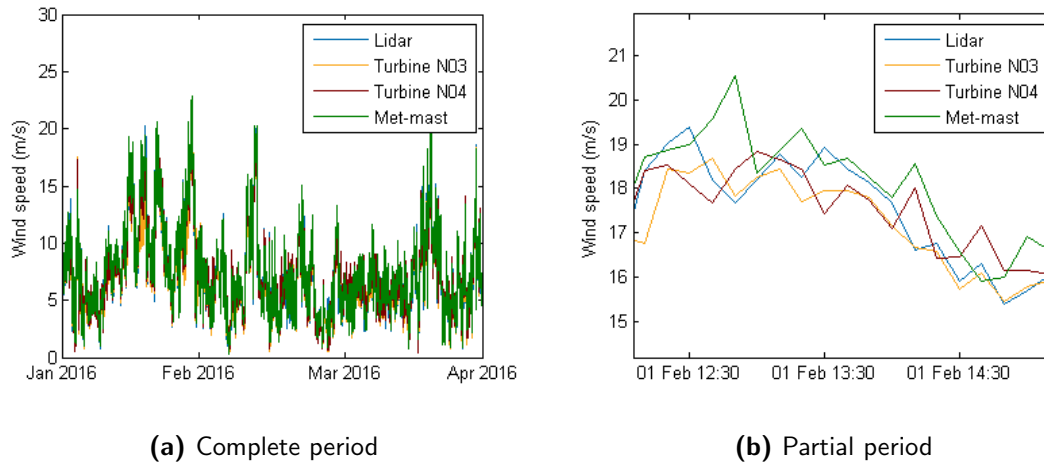
Figure 5.1: Data synchronisation check between met-mast, Lidar and turbines N03 and N04

corresponding data from the other data sets were removed and the time stamps were ordered chronologically for alignment.

The alignment was checked by comparing the wind speeds from the different measurement devices. The measurements during the complete measurement campaign can be seen in Figure 5.1a. Since the met-mast was located at a significant distance away from the Lidar and turbines, an offset between the wind speed measurements as seen in Figure 5.1b was expected. The wind speed measurements of turbine N03 and the Lidar at 98 m show a good alignment.

5.1.2 Wind speed

First, the wind speed measurements of the Lidar and turbines N03 (Figure 5.2a) and N04 (Figure 5.2c) are compared to each other. Wind speeds below the cut-in wind speed at hub height are of less interest, because PCV is performed with wind speeds above this wind speed. It can be seen that at lower wind speeds the difference is up to 5 m/s. This could be caused by the turbines that cannot accurately measure the free-stream wind speed since they are located behind the rotor. Another factor could be wake effects from other turbines affecting the Lidar or turbine or even both measurement devices.

To check this, a comparison is made after excluding data when the wind is coming from the disturbed sectors. As can be seen from Figure 5.2b and Figure 5.2d, the wind speed measurements from the Lidar and turbines compare better to each other after excluding disturbed measurements. The results differ by approximately 4%, which is low compared to literature in which deviations up to 9% were presented[47]. Since the nacelle anemometer at the turbines are located behind the rotor and therefore measures disturbed flow, it is not recommended as reference measurement device. This explains also the lack of research into wind speed measurements using nacelle anemometers. However, it can be concluded that turbine wakes affect the measurements significantly.

(a) Turbine N03

(b) Turbine N03

(c) Turbine N04

(d) Turbine N04
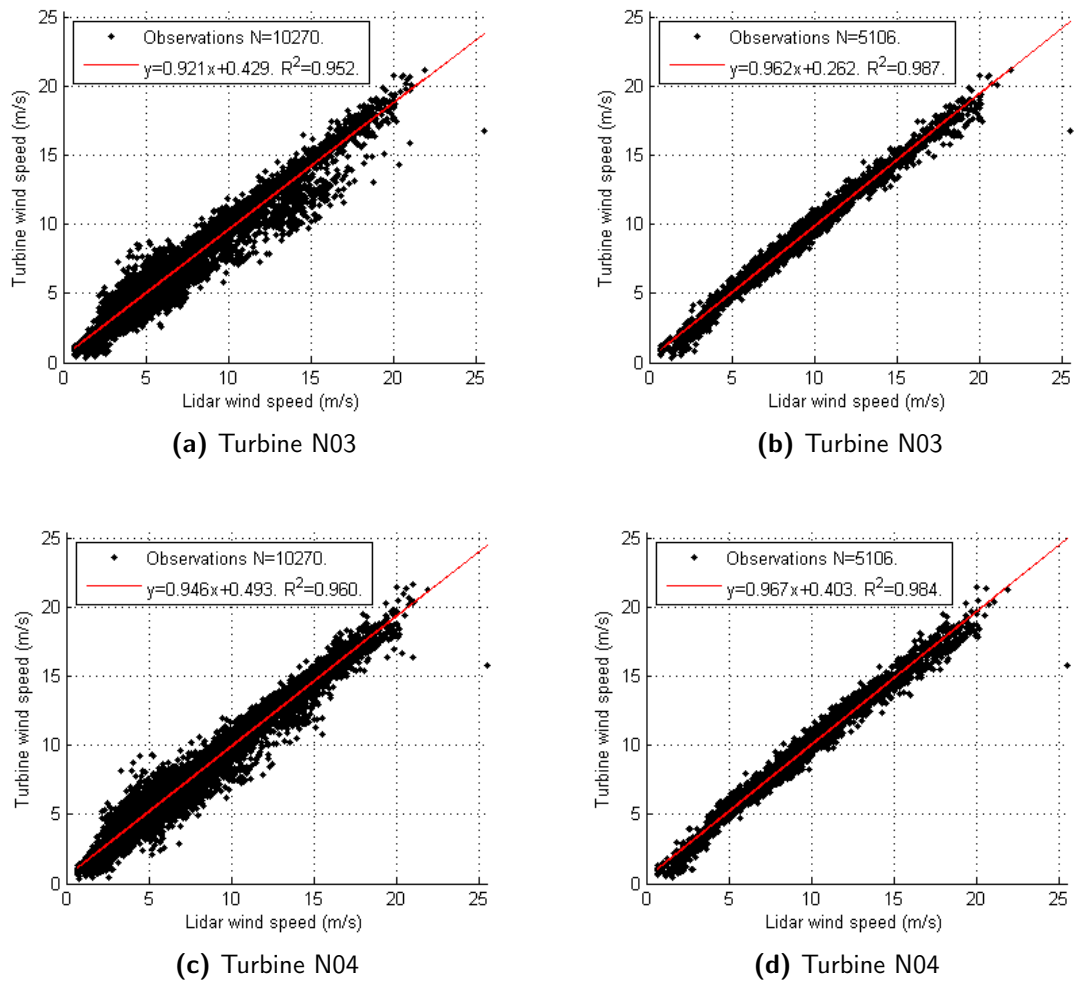
Figure 5.2: Validation of wind speed measurements by Lidar against turbines

(a) Full period   **(b)** Partial period
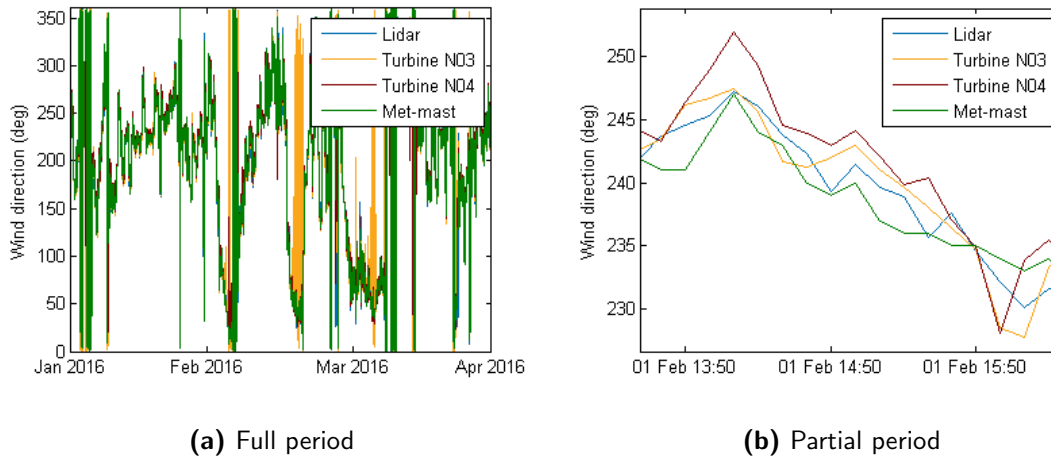
Figure 5.3: Validation of wind direction

5.1.3   Wind direction

An overview of the wind direction measurements made by the Lidar, nacelle sonic anemometers at turbines (N03 and N04), and met-mast can be seen in Figure 5.3a. The Lidar offset was sometimes near 180°, which was also discussed in subsection 4.1.6. The measurements of the met-mast or turbines were investigated to adjust this, because correct wind direction measurements are needed to exclude data collected during wind coming from disturbed sectors in PCV.

Also, an offset in the measurements from turbine N03 can be seen in Figure 5.3b. This is a common problem at operational wind farms[62]. It is resolved by adding the difference between the mean direction measured by turbine N03 and turbine N04. The mean is only taken from the measurements where the difference between the measurements of both turbines was lower than 90°, so that significant errors are not taken into account. Turbine N03 measured approximately 35° lower than turbine N04. A more detailed investigation into the measurement offset is performed in Appendix B. It should be noted that the rotors were orientated correctly in the wind, the direction measurements are only relative offsets from the calibrated north.

Hereafter, the wind direction measurements from the Lidar and turbines are compared again using scatter plots. In Figure 5.4a and Figure 5.4c, the scatter plots are shown between the measurements of the Lidar and turbines N03 and N04. In case of turbine N03 (Figure 5.4a), it did not measure wind directions between 20° and 45°. On the other hand, the nacelle sonic anemometer at turbine N04 did not measure wind directions above 340°. The Lidar and met-mast measurements were investigated to check if the Lidar was working sufficiently. This was checked with the scatter plot in Figure 5.5 which confirms that the Lidar measurements of the wind direction are correct. Therefore, the errors in the turbine direction measurements are presented to the SCADA team of Vattenfall. More details concerning the erroneous measurements of turbine N03 are presented in Appendix B.

Since the erroneous measurements of the turbines affect the comparison, another scatter plot is made for both turbines after filtering with the measurement sectors. In Figure 5.4b

(a) Turbine N03   (b) Turbine N03

(c) Turbine N04   (d) Turbine N04
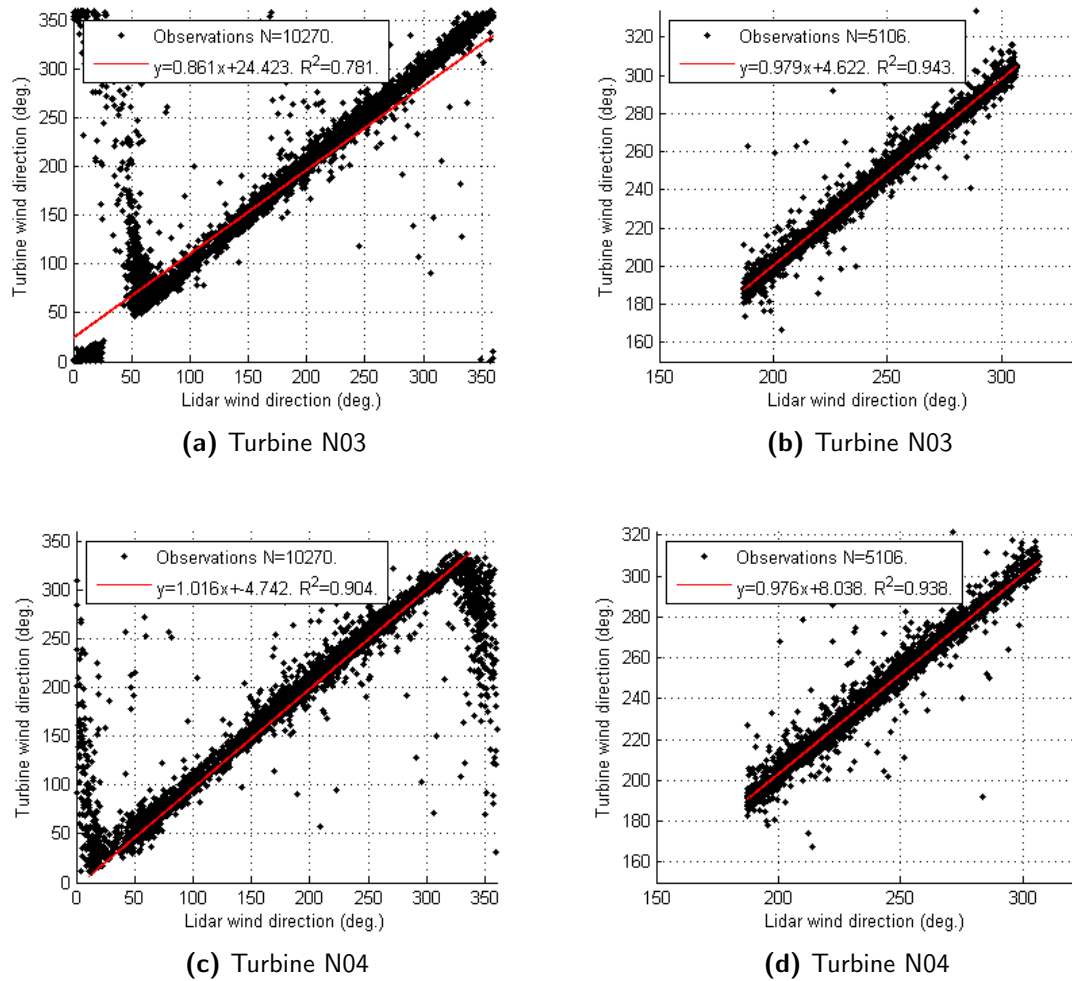
Figure 5.4: Validation of wind direction measurements by Lidar against turbines

and Figure 5.4d can be observed from the difference of approximately 1% that the wind direction measurements compare better.

5.1.4 Air density

The meteorological station of the Lidar measures the conditions that are required to determine the air density with Equation 2.27: temperature, pressure and humidity. In this case the air density is corrected to hub height, since the Lidar is located on the ground including its meteorological station. Since the turbines do not contain a meteorological station, the air density measurements of the Lidar are validated by the met-mast. The air density measurements during the campaign are shown in Figure 5.6a. It was found that the Lidar measured approximately 0.021 kg/m^3, or 1.68%, higher air density than the met-mast. This is in agreement with the results of van der Velde.

The scatter plot, Figure 5.6b, shows the difference between the air density measurements of the Lidar and met-mast as well. An important difference between the meteorological
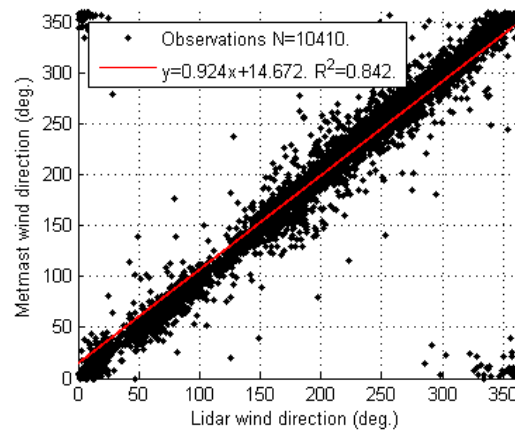
Figure 5.5: Wind direction measurements from Lidar and met-mast

(a) Air density measurements at hub height

(b) Scatter plot of air density measurements
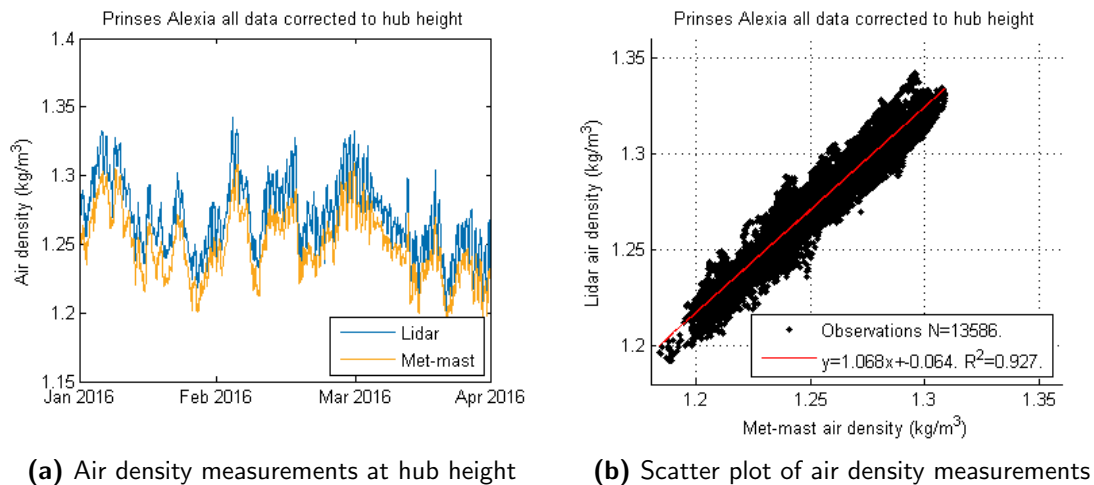
Figure 5.6: Validation of air density measurements by Lidar against met-mast

stations of both measurement devices is the location as the Lidar is installed on ground level including the meteorological station while the met-mast contains meteorological equipment near hub height. This can influence the temperature measurements due to heat supply from the ground for example. Villanueva Lopez found that density changes 2% with a 5°C (±2%) change in temperature in dry air at 1 atm and 15°C[53]. Also, a relative pressure change has the same effect on air density as the temperature. On the other hand, humidity has a negligible effect on the air density.

In Appendix C, the temperature, pressure and humidity measurements are presented. This helps to clarify the deviation in the air density measurements between the Lidar and met-mast. The 1.68% higher air density measured on average by the Lidar results from the 0.40% lower temperature and 1.23% higher pressure ($\frac{1}{0.9960}1.0123 = 1.64\%$), including some rounding errors.

(a) Met-mast at 46 and 98 m

(b) Lidar at 11, 57, 98, 150 and 200 m
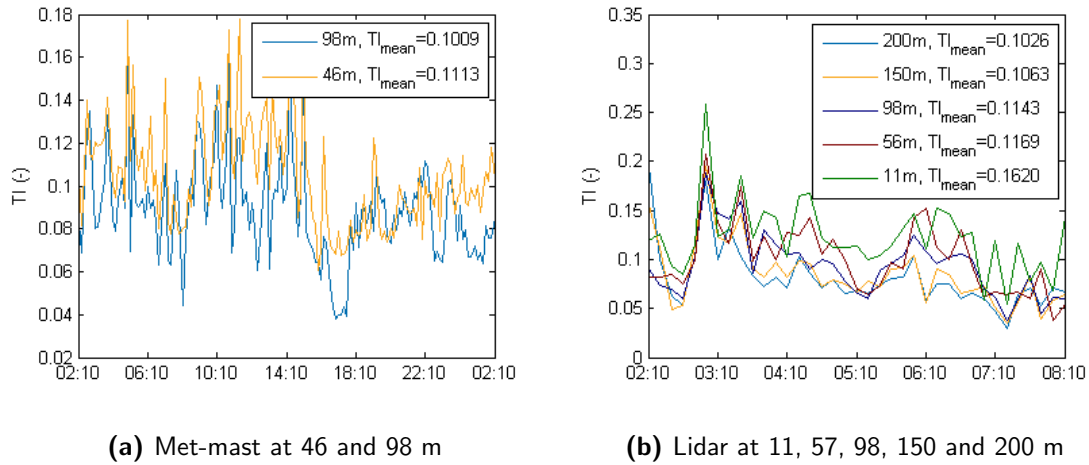
Figure 5.7: Turbulence intensity measurements of met-mast and Lidar at several heights

5.1.5 Turbulence intensity

The TI is a direct output of the Lidar, but the turbine and met-mast data does not include this parameter. TI can also be calculated using Equation 4.1 for which the mean wind speed and the standard deviation are required. In fact, the TI measurements of the Lidar are based on the same principle. First, using the standard deviation and RWS measured by each beam the TI can be calculated. Then, these two TI values are averaged to obtain the actual TI. Since the standard deviation is only measured by the met-mast, the TI measurements of the Lidar can only be compared to the met-mast. However, the large distance between the met-mast and Lidar can result in significant differences. Also, there is no consensus about the accuracy of measuring TI with cup anemometers.

First, the TI at different heights are analysed to check the TI change with height. The met-mast measures TI at 46 m and 98 m (hub-height) and the measurements during the campaign at Prinses Alexia can be seen in Figure 5.7a. The Lidar measures TI at every measurement range, but the following heights are plotted in Figure 5.7b: 11, 57, 98, 150 and 200 m. From both figures can be seen that the TI decreases with height, which is expected due to the lower influence of the terrain. This can be clearly seen from the TI measurements at 11 m of the Lidar. Also, after filtering for the undisturbed measurement sectors, the mean TI measured by the met-mast at 46 and 98 m reduce to 0.1022 and 0.0896. This can be explained by the increase in turbulence when obstacles disturb the wind flow.

Before the Lidar measurements are compared to the met-mast TI measurements, the TI is also calculated using Equation 4.1 to verify the output TI of the Lidar. Interestingly, a difference was found between both values. Below 20 m a factor of 0.96 was found between the output and calculated TI. Above hub height a factor of 1.09 was defined and between 20 m and hub height a linear increase was found. The offset was checked with the Lidar manufacturer (ZephIR) to ensure that the Lidar measurements were trustworthy The answer was that the TI measurements were defined using Equation 4.1 including a correction factor as determined from a comparison with a cup anemometer. These correction factors were equal to the differences that were found during the comparison.

(a) Linear regression

(b) Linear regression forced through origin
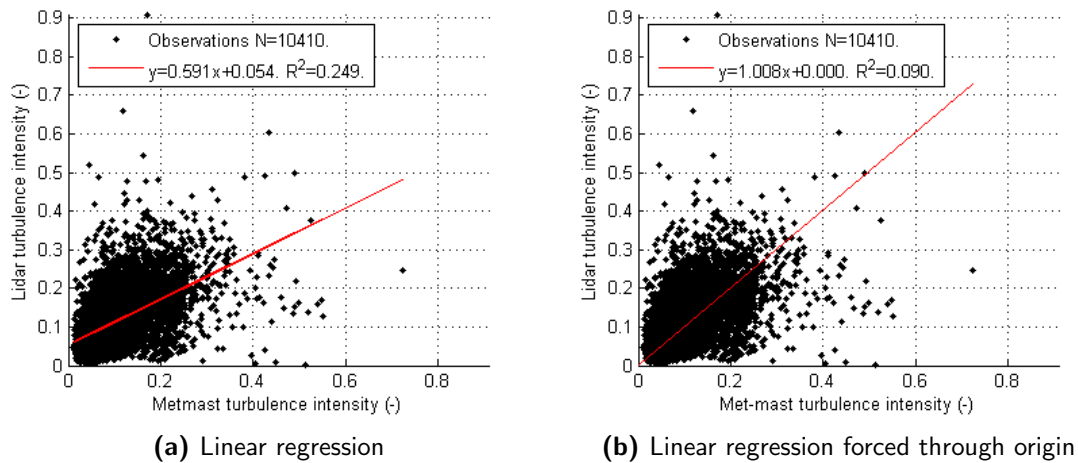
Figure 5.8: Validation of turbulence intensity measurements by Lidar against met-mast

Hereafter, the Lidar measurements can be compared to the met-mast. The scatter plot of the TI measurements is shown in Figure 5.8a to give an indication about the Lidar's ability in measuring TI. A large scatter can be seen which is caused by the large distance between both measurement devices. For example, wind conditions experienced by the met-mast could flow through the whole wind farm before they reach the Lidar. This means that a lot of obstacles disturb the flow while the met-mast measured undisturbed flow. A similar result was seen by Goossens, who compared Lidar and Sodar TI measurements to each other. In Figure 5.8b, the regression line is forced through the origin, which affects the coefficient of determination negatively. Although the trend is similar on average, the TI measurements show large scatter. In addition, van der Velde obtained comparable results with less scatter. An important difference was the location close to the met-mast resulting in a better comparison.

5.2   Nørrekær Enge

The validation of Nørrekær Enge includes data alignment and comparisons of different data sources. Measurements of two nacelle-based Lidars and spinner anemometers will be compared to met-mast measurements. Also, an overview of the five-beam Lidar measurements and its availability are given.

5.2.1   Five-beam Lidar

Measurement parameters

Before the validation is performed, the measurement parameters of the Avent five-beam Lidar are presented. The output signals that are collected by the Lidar are listed in Table 5.1. The parameters that will be used for this thesis are the following: *Name*, *LOS*, *Range*, *Speed*, *V_shear*, *V_shear_avail*, *RWS*, *dRWS*, *CNR*, *LOS_avail*, *Tilt*, *H_dir* and

Table 5.1: Output signals including units and description by the Avent five-beam Lidar[3]

Signal	Unit	Description
Timestamp	[s]	Coordinated Universal Time (UTC)
LOS index	[-]	Beam number
Range	[m]	Lidar measurement range
Speed	[m/s]	Rotor averaged longitudinal wind speed
H_shear	$[s^{-1}]$	Longitudinal wind speed horizontal slope
V_shear	$[s^{-1}]$	Longitudinal wind speed vertical slope
H_shear_avail	[-]	Data availability for horizontal wind shear exponent
V_shear_avail	[-]	Data availability for vertical wind shear exponent
RWS	[m/s]	Radial wind speed
dRWS	[m/s]	Radial wind speed standard deviation
CNR	[dB]	Carrier to noise ratio
LOS_avail	[-]	Availability LOS
Tilt	[rad]	Tilt angle
Roll	[rad]	Roll angle
free_spd	[m/s]	Free wind speed
L_shear	$[m^2/s]$	Longitudinal wind shear
H_shear1	$[m^{-1}]$	Global horizontal shear
V_shear1	$[m^{-1}]$	Global vertical shear
H_dir	[rad]	Horizontal wind direction
V_dir	[rad]	Vertical wind direction
Available	[-]	Availability

Available. As the Avent Lidar data does not contain temperature, pressure and humidity, the air density cannot be measured.

Availability

The availability of the Avent Lidar depends on the availability of each beam, which is related to failures in the measurements. Another factor determined by the amount of backscattering signals is the Carrier-to-Noise Ratio. The focus will lie on the Lidar measurements at 235 m, since these will be validated and used for PCV.

The same filters as applied on the data by Borraccino and Courtney will be used, so the data is filtered for a minimum availability of 95% and a minimum Carrier-to-Noise Ratio of -18 dB[8]. The resulting percentage of filtered data is only 2.7%, which is caused by the significant amount of 93% filtered due to the low Carrier-to-Noise Ratio of LOS 3. Also, the Carrier-to-Noise Ratio of LOS 0 and LOS 4 is low, around 27%, compared to the overall availability of 65%. However, the Carrier-to-Noise Ratio threshold was mentioned as arbitrary and unit specific so that it could be adjusted.

A different threshold of -21 dB, which was used by Wessels, filtered out 75% of the data. Again, only one beam has a significant influence while other beams filtered only 50% of the data which is closer to the overall availability of the Avent Lidar. Interestingly, Borraccino and Courtney found that the availability threshold of 95% filtered only 15% out and the minimum Carrier-to-Noise Ratio of -18 dB 1%. Therefore, it can be questioned

whether these thresholds are too high or that the measurements of the Lidar, or only one beam of the Lidar, were faulty. Thus, the measurements will be filtered using a minimum availability of 70% to take a sufficient amount of data into account for the next analyses.

5.2.2 Data alignment

Before measurements could be compared, the data sets had to be aligned since they were collected in different time zones. The met-mast data had time stamps in the UTC+1 zone which was used as reference. Compared to this time zone, the SCADA data was collected in the same time zone but included the shift to summertime. Therefore, the time stamps till 3:00 AM on the 25th of November had to be adjusted by subtracting one hour.

The Avent Lidar and ZephIR Lidar collected data in the same time zone as the met-mast, but the time stamps were defined as the end time of the 10-minute measurement intervals. This was corrected by subtracting 10 minutes from the time stamps of both Lidars. The same difference in the time stamp definition held for the spinner anemometer data, but they were collected in the UTC time zone. Consequentially, 50 minutes were added to the time stamps.

In addition to the difference in time zones or time stamp definitions (time stamp at the start or end of a 10-minute measurement interval), the data sets of the Lidars were not chronically ordered. For instance, different groups of a few hours of measurements were located at the wrong location in the data set. This could corrected by sorting the complete data sets by time to obtain chronologically ordered data sets.

Hereafter, the completeness of each data set was determined by looking for missing time stamps. Only the time stamps that were present in each data set are used for comparisons with other measurement devices. Finally, the data sets were aligned and chronically ordered so that the validation process could be performed more easily. A first comparison of the wind speed at hub height measured by the different measurement devices is shown in Figure 5.9a. A part of this time series is displayed in Figure 5.9b to show the synchronised data sets in more detail. In this case, the measurements of the spinner anemometer at turbine 4 are considered, because the Lidars were also installed at this turbine.

From the wind speed time-series in Figure 5.9b cannot be clearly seen that the data is sufficiently aligned. To check if the time stamps were adjusted correctly, scatter plots were made for several adjustments in the time ranging from -20 to 20 minutes in steps of 10 minutes. Comparisons are made of the wind speed measurements between each measurement device and the met-mast and shown in Appendix D. It can be seen that the data was aligned correctly, since the scatter plots show the highest correlation without any further adjustments in all cases.

5.2.3 Wind speed

In this section, the wind speed measurements of the Lidars, spinner anemometer and wind vane on turbine 4 will be compared to the met-mast. Filters were applied to exclude disturbed wind speed measurements as well as errors in the Lidar readings. The Lidar measurements are taken at 2.5 rotor diameters in front of the turbine. The tilting of

(a) Complete period   (b) Partial period
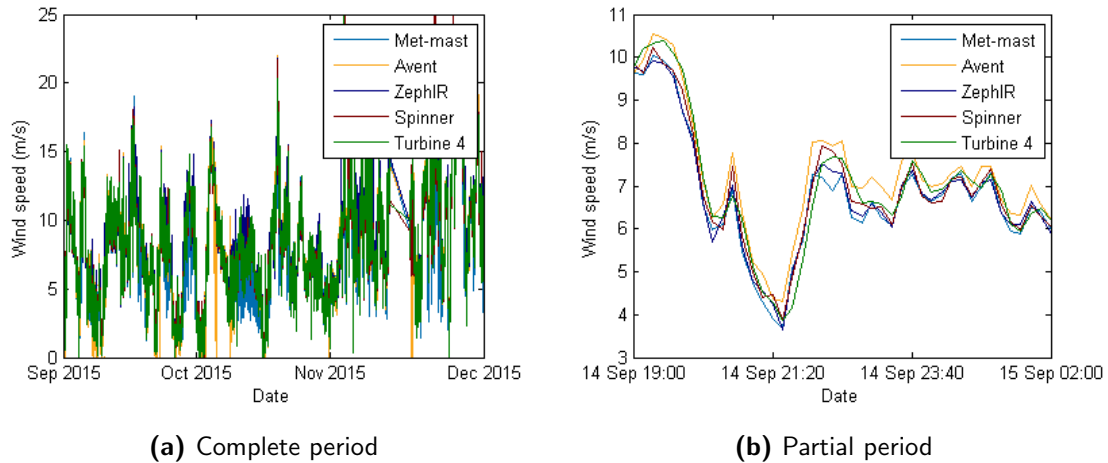
Figure 5.9: Data synchronisation check between met-mast, Lidars, spinner anemometer and turbine 4

the Lidars as discussed in subsection 2.4.11 is taken into account so that the Lidar wind speed measurements are corrected to hub height. The scatter plots for the comparisons of the wind speed at hub height are shown in Figure 5.10. From the scatter plots can be seen that the wind speed measurements of each measurement device compare well to the met-mast.

5.2.4 Yaw misalignment

Next, the YM measurements are analysed in more detail. Before this, the turbine direction was checked since at Prinses Alexia the turbine direction was measured incorrectly. Again, an offset of 9.9° in the average wind direction measured by the turbine in the undisturbed measurement sectors was found compared to the met-mast. The same deviation was found in the turbine direction measurements by comparing the wind direction measurements of the turbine to the turbine direction. A correction was applied using the IEC-compliant met-mast as reference, since the other turbines had also erroneous direction measurements which could thus not be used for the correction as done for the turbine direction readings of Prinses Alexia. Therefore, 9.9° was subtracted from the wind and turbine direction readings.

Hereafter, the YM measurements are presented in a histogram to show the measurement distribution over the different YM angles in Figure 5.11. Before the distributions were made, the measurements were filtered for the measurement sectors, and corrected if the YM was 180° or 360° off compared to the YM measured by other devices so that errors did not have significant impact on the analysis.

In Figure 5.11, the differences in the mean and standard deviation between the measurement devices can be observed. It can be seen that the Lidars perform similar as their mean and standard deviation lie close to each other. The spinner anemometer shows the smallest standard deviation whereas the mean of the met-mast measurements is closest to zero. However, the mean of the met-mast measurements was biased due to the correction in the turbine data using the met-mast measurements as described above. A lower

(a) Avent five-beam Lidar

(b) ZephIR Lidar

(c) Spinner anemometer

(d) Turbine 4
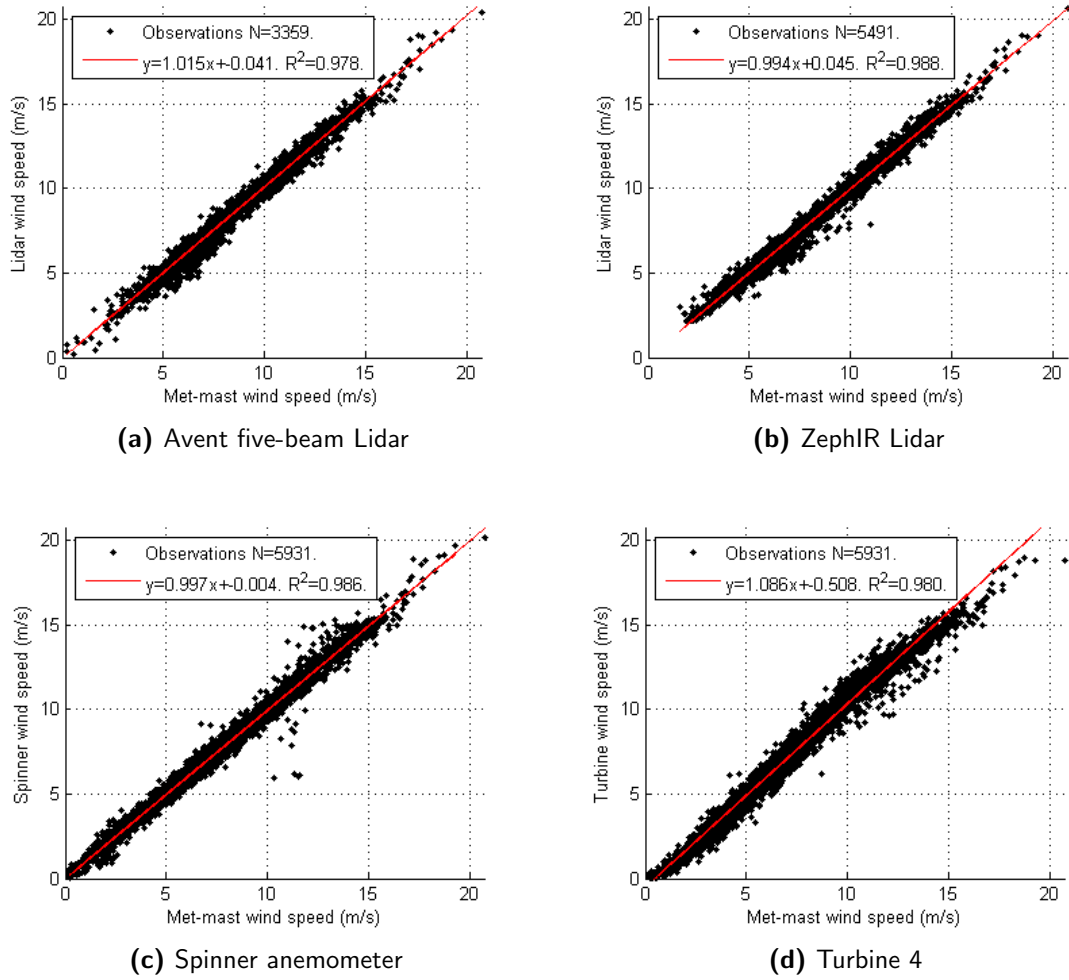
Figure 5.10: Validation of wind speed measurements from measurement devices against met-mast
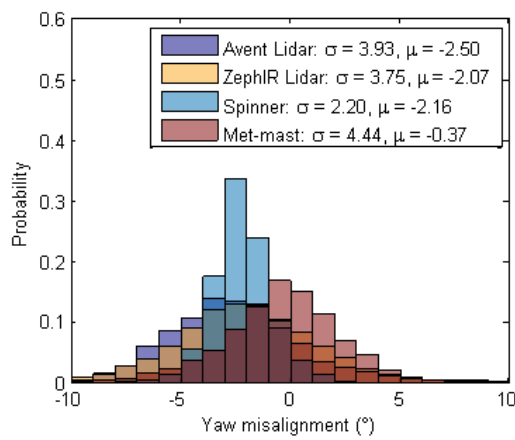
Figure 5.11: Distribution of YM measurements from each measurement device

(a) Avent Lidar

(b) ZephIR Lidar

(c) Spinner anemometer
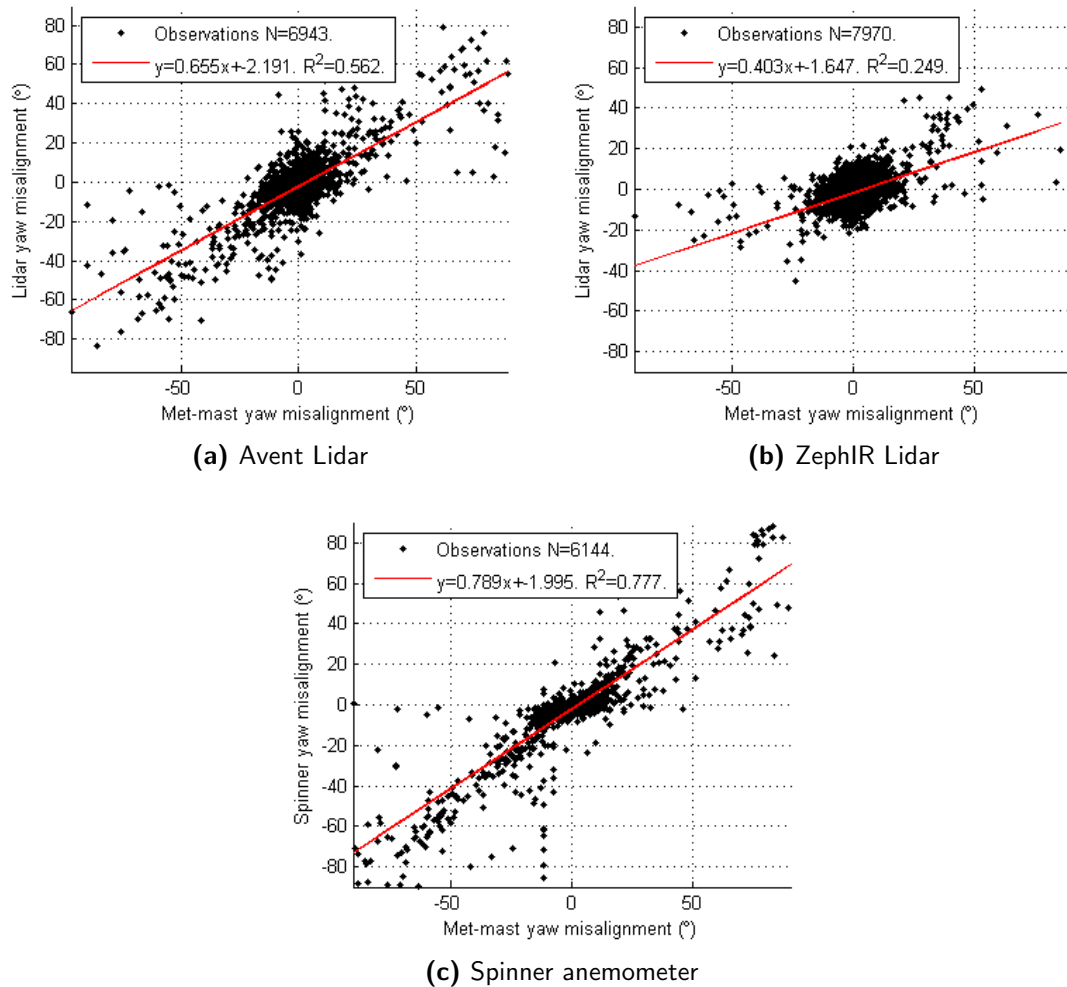
Figure 5.12: Comparison of YM measurements from Lidars and spinner anemometer against met-mast

standard deviation could indicate a lower uncertainty in determining YM compared to another measurement device.

In addition, scatter plots are made to examine the YM measurements better. The YM measurements of the Lidars and spinner anemometer are compared to the met-mast measurements in Figure 5.12. A filter is applied for the undisturbed measurement sectors so that a reliable comparison can be made without disturbed measurements. It can be seen that the correlation between the YM measurements of the Avent Lidar and the met-mast is significantly better than the ZephIR. The correlation of the Avent five-beam Lidar is also better compared to previous studies in which a nacelle-based Avent two-beam Wind Iris was examined[19][61]. The better measurements of the Avent Lidar could be caused by the more beams it contains so that a lower uncertainty can be obtained. Furthermore, the spinner anemometer compares well with the met-mast, which could support its ability to measure YM more accurately than Lidar. Finally, the measurement devices measure a lower YM than the met-mast, which was also found by Wessels.
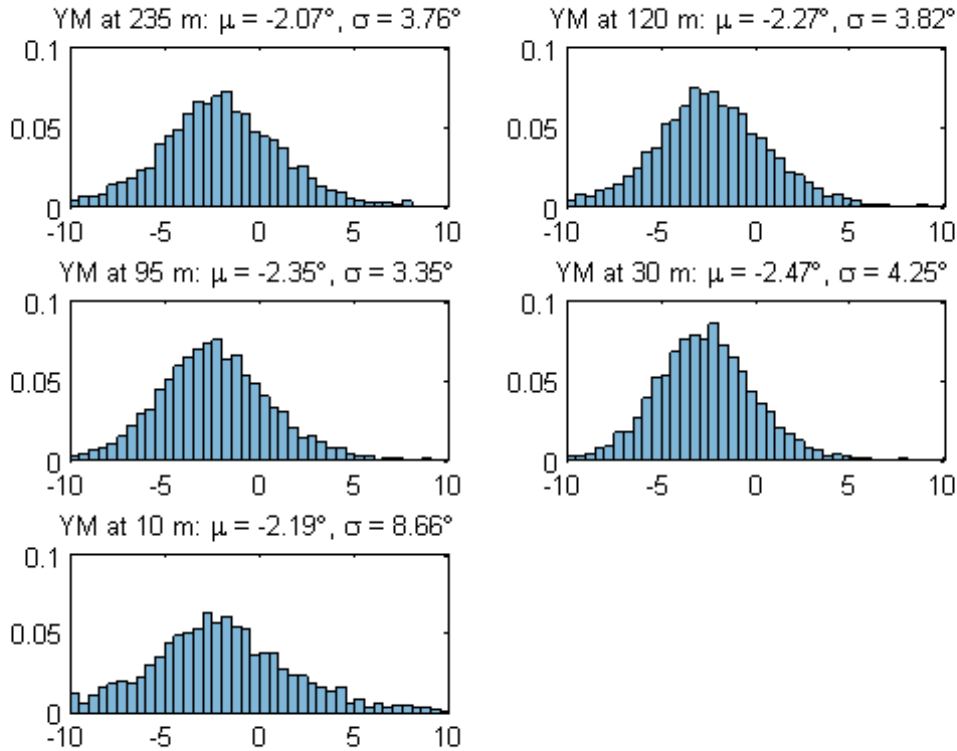
Figure 5.13: Distribution of YM measurements at different ranges from the ZephIR Lidar

As Goossens and Wessels discussed, wind direction will change with distance in front of the rotor. This is examined by looking into YM measurements by the ZephIR Lidar at different ranges. As expected, the mean YM varied up to $0.40°$ from 10 m to 235 m in front of the rotor. In addition, the measurements of the ZephIR Lidar are shown at 5 different ranges in Figure 5.13 including the standard deviation. From 235 to 90 m, the standard deviation decreases which is in accordance with literature. Closer to the turbine, the validity of having better YM measurements disappears. Consequently, a measurement range around 90 m seems reasonable to detect YM and to correct the turbine alignment with the wind. Nonetheless, it should be mentioned that the reaction time should be improved when measuring closer to the rotor if direct response is required. To conclude, nacelle-based Lidar is a valuable tool for detecting of and correcting for YM but can be done more accurately with spinner anemometers. Furthermore, using nacelle-based instruments will solve the problem of having a mis-calibrated SCADA signal of the turbine direction.

Furthermore, wind direction or YM measurements have been put in doubt by the Lidar manufacturer Avent Lidar Technologies. Goossens found that the accuracy of the Wind Iris in measuring YM was equal to $±4°$. It would therefore be interesting to compare the YM measurements of the five-beam Lidar to the met-mast or spinner anemometer. From the comparison to the met-mast was found that the average difference between the measurements and the standard deviation of the differences were equal to $4.4°$ and

(a) ZephIR Lidar **(b)** Spinner anemometer
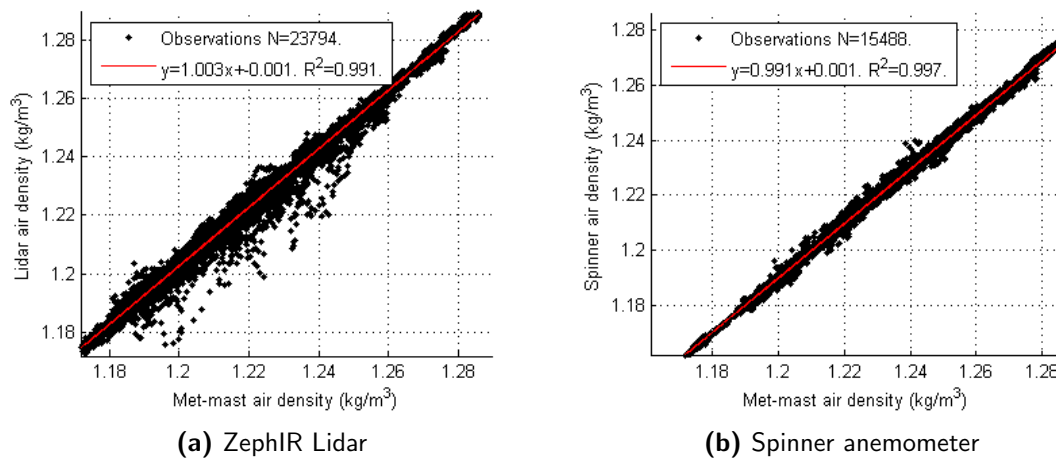
Figure 5.14: Validation of air density measurements by Lidar and spinner anemometer at turbine 4 against met-mast

5.1° respectively. A similar standard deviation was found from the comparison to the spinner anemometer while the average difference was equal to 3.5°. Interestingly, these results lie close to the findings of Goossens. Since a two-beam Lidar would be affected by heterogeneity as discussed in [61], the uncertainty of the five-beam Lidar YM measurements could also be questioned. The effect of heterogeneity on Lidar measurements will be further discussed in chapter 8.

5.2.5 Air density

The air density can only be measured when a meteorological station is present. At Nørrekær Enge, the spinner anemometers and ZephIR Lidar contained a meteorological station. However, the spinner anemometers did not measure humidity. Since humidity has a low effect on air density measurements as discussed in Appendix C, a relative humidity of 80% was assumed which seemed to be reliable as this value was close to the average humidity measured by the met-mast. Also, in contrast to Prinses Alexia, all meteorological stations are located at hub height. Thus, improved correlations of the air density measurements between the Lidar or spinner anemometer and the met-mast are expected.

The air density measurements of the Lidar and spinner anemometer are compared to the met-mast as shown in Figure 5.14a. A good correlation between the measurements can be observed (R>0.99) for both devices. A small difference can be seen in the measurements of the spinner anemometer, but it is less than 1% which has a negligible effect on the wind speed correction for example. The effect of the height at which the meteorological station is located can be seen from the larger scatter around the linear regression line in Figure 5.6b where the meteorological station was located on the ground.

5.2.6   Turbulence intensity

As discussed in subsection 5.1.5, the TI of Lidars can be calculated by taking the average of the TI measured by each beam. The Avent Lidar data does not contain the actual TI, but it did measure the RWS and its standard deviation. The TI is then calculated from the values collected with only beam 0, since only this beam was pointed at hub height. The TI had also to be calculated for the met-mast whereas the data of the ZephIR Lidar and spinner anemometer contained TI measurements. The TI values of the spinner anemometer and ZephIR are internally calculated by dividing the standard deviation by the wind speed. However, it should be noted that the measurements of the ZephIR Lidar are affected by volume-averaging and the different orientation of the two beams as discussed in subsection 3.1.1.

Finally, the measurements of the Lidars and spinner anemometer are compared to the met-mast as presented in Figure 5.15. The filtered measurements are obtained after applying a filter which excludes the disturbed measurement sectors. Also, the availability of beam 0 of the Avent Lidar is checked. Only the measurements with an availability of at least 80% are taken into account to ensure a reliable analysis. Furthermore, TI values above 0.5 are neglected for the comparison to the met-mast, because these values seem to be incorrect and affect the fit significantly. Large scatter can be seen in the original scatter plots as shown by the low R^2-values. A similar result was obtained at Prinses Alexia, however the distance between the measurements influenced the comparison negatively. Furthermore, it seems that the ZephIR Lidar underestimates TI compared to met-mast as the slope of the fit is close to 0.5. Interestingly, the Avent Lidar and spinner anemometer also show this behaviour but less significant.

In the filtered data, the effect of excluding disturbed conditions can be clearly observed from the significant lower scatter. The slopes of the Avent Lidar and spinner anemometer are improved and approach unity, but the ZephIR Lidar still shows problems with measuring TI as discussed by literature[41]. The scatter of the Avent Lidar is similar to comparisons between Lidar and met-mast from literature as shown in Figure 5.16[51][61]. Also, the correlation between the spinner anemometer and met-mast shows comparable results[61].

5.2.7   Alternative comparisons

In addition to the comparisons of the Lidars and spinner anemometer against the met-mast, the Lidars and spinner anemometer are compared to each other as presented in Appendix E. Although it cannot be concluded which measurement device measured most accurately, the comparisons of both Lidars to the met-mast and spinner anemometer show that the Avent Lidar is better in measuring wind speed, wind direction/YM or TI than the ZephIR Lidar.

(a) Avent Lidar

(b) ZephIR Lidar

(c) Spinner anemometer
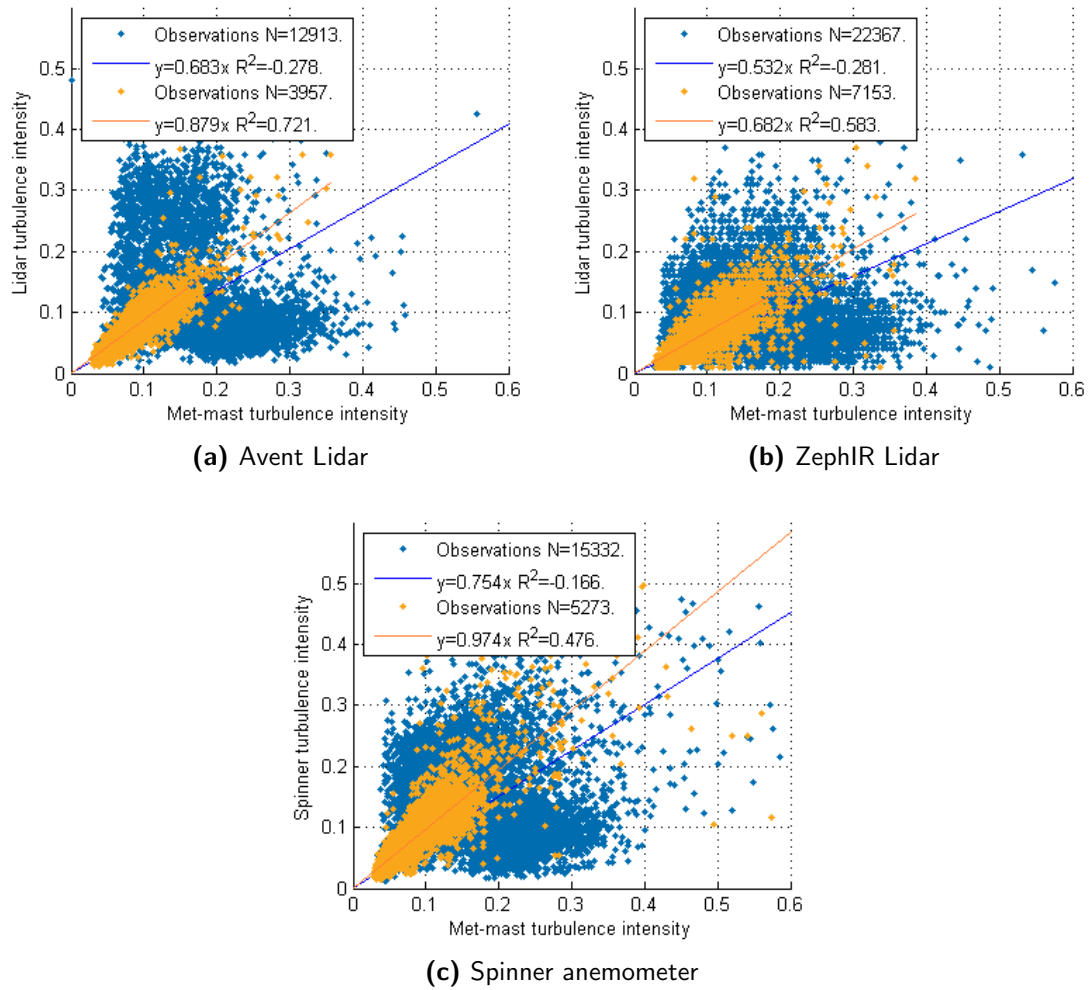
Figure 5.15: Comparison of TI measurements from Lidars and spinner anemometers against met-mast
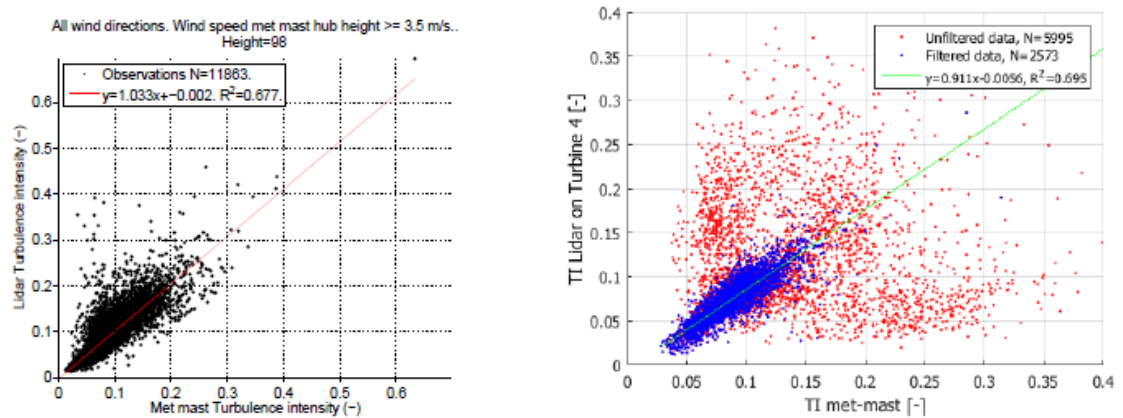
(a) TI validation of a ZephIR Lidar with a met-mast at Prinses Alexia[51]

(b) TI validation of a Wind Iris Lidar with a met-mast at Nørrekær Enge[61]

Figure 5.16: Correlation between met-mast and Lidar TI measurements from literature

Chapter 6

Power Performance Testing

The power performance of the wind turbines will be tested by PCV according to the IEC. Thus, PCV will be performed by following the steps that are listed in section 2.4. Two turbines at Prinses Alexia will be analysed by using ground-based Lidar measurements only. One turbine at Nørrekær Enge will be investigated with met-mast, nacelle-based Lidars and spinner anemometers.

The purpose of the PCV at Prinses Alexia is to analyse the ability of a ground-based Lidar, validated with a met-mast, to perform PCV as well as to investigate the effect of REWS, YM and TI on turbine performance. At Nørrekær Enge, the focus will lie on the comparison between different measurement devices for PCV.

6.1 Prinses Alexia

In this section, the PCV of turbines N03 and N04 at Prinses Alexia using ground-based Lidar measurements is presented.

6.1.1 Rotor Equivalent Wind Speed

Since a Lidar is used for wind speed measurements at different heights, it is possible to determine the power curve as function of REWS. Also, the power curve as function of the wind speed at hub height can be determined so that the effect of REWS on PCV can be investigated. First, a comparison between the hub height wind speed and REWS will be given. Secondly, the difference in power curves and AEP will be shown.

A scatter plot of the hub height wind speed against the REWS measured by the Lidar is shown in Figure 6.1. A small difference can be seen between both wind speeds. The REWS is calculated with Equation 2.23 using the following measurement heights: 56, 77, 98, 118, 139 and 150 m. Each segment can be calculated with Equation 2.24, which is validated with a different theory according to the on-line calculation program *Wolfram Alpha*.
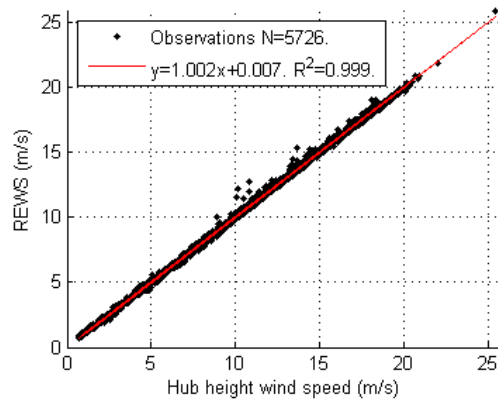
Figure 6.1: Scatter of hub height wind speed and REWS measured by Lidar
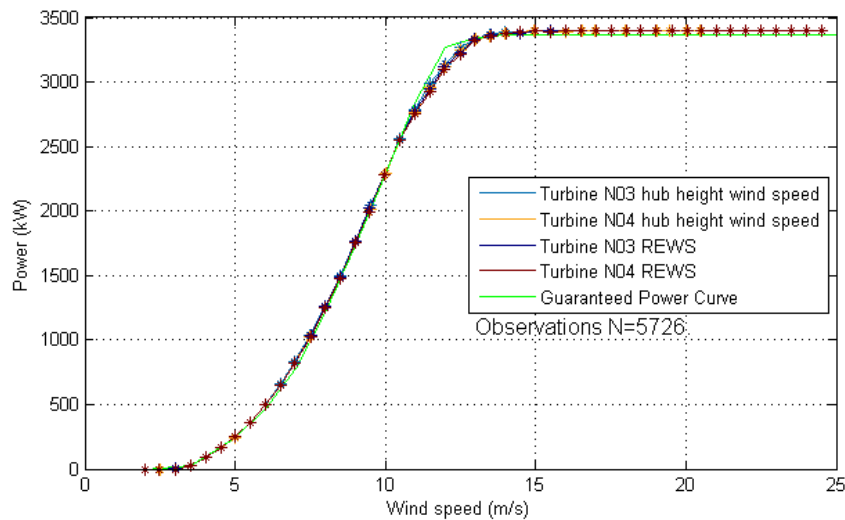
Figure 6.2: Comparison of power curves based on hub height wind speed and REWS

The power curves made with hub height wind speed and REWS show a good correlation as seen from Figure 6.2. They are compared to the guaranteed power curve from which it can be seen that the turbines perform well as the power curves lie close to the guaranteed power curve. However, a better comparison can be made by looking into the AEP in Figure 6.3. The AEP of turbine N04 is up to 1.65% lower than guaranteed, but the wind conditions that were used to determine the power curve do include outer envelope conditions where the power curve is not guaranteed. On the other hand, turbine N03 performs close to the guarantees. In subsection 6.1.5, another comparison will be made using inner envelope conditions which can have a positive effect on the power curves as discussed by Wessels.

The AEP based on the hub height wind speed and REWS are also compared to each other. The results are shown in Figure 6.4 for annual mean wind speeds between 4 and 11 m/s. Using REWS leads to a similar decrease in AEP for both turbines, which was expected because of the higher wind speed measured as seen from Figure 6.1.
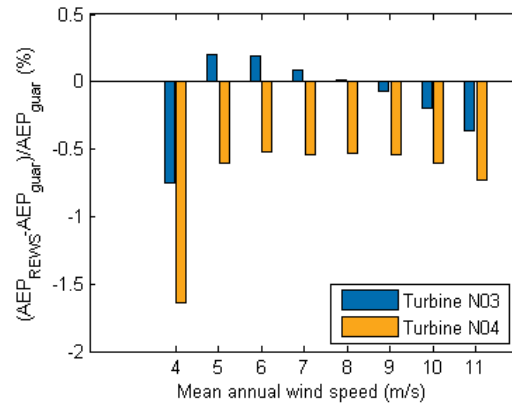
Figure 6.3: Difference between the AEP calculated with REWS and the guaranteed AEP
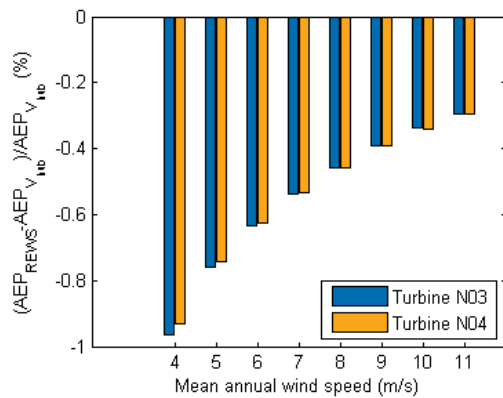
Figure 6.4: Difference between AEP based on REWS and hub height wind speed
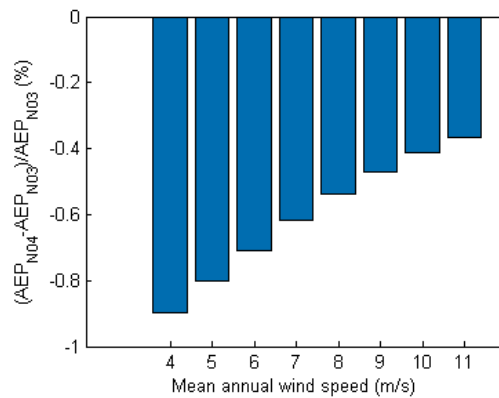
Figure 6.5: Difference between AEP of turbines N03 and N04 using REWS

In addition, the AEP of the two turbines are compared to each other using REWS as recommended by the IEC. In Figure 6.5, the difference in AEP for several annual mean wind speeds is shown. A maximum of 1% difference can be seen at the lowest annual mean wind speed that is considered.

To conclude, REWS will give a more realistic representation of the wind speed experienced by the whole rotor area than hub height wind speed. Since Lidar can measure wind speed accurately, as discussed before, the implementation of REWS using Lidar measurements can lead to better PCV. In general, due to the small increase in wind speed the power curve will reduce slightly up to rated wind speed.

6.1.2 Veer

The Lidar measured not only wind speed at several heights, but also wind direction. This allows for wind veer correction as discussed in section 2.4. In this way, the wind speed perpendicular to the rotor can be calculated, so that the effect of changes in wind direction along the height, i.e. veer, can be taken into account resulting in an even better
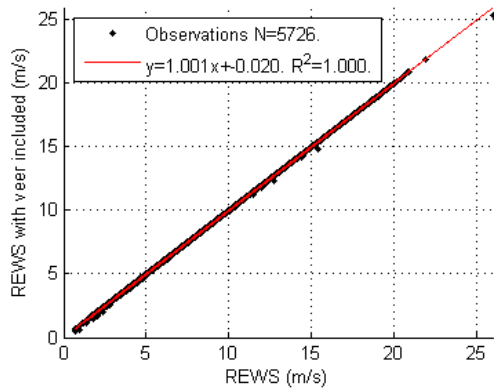
Figure 6.6: Scatter of REWS and REWS with veer included measured by Lidar
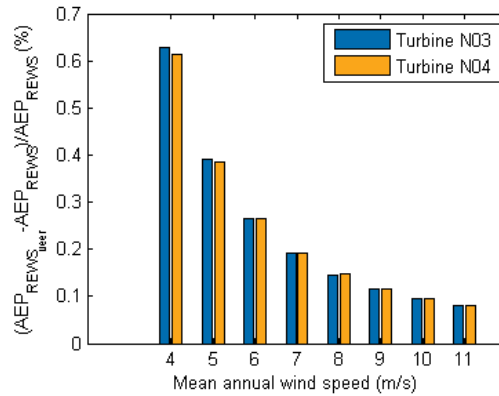
Figure 6.7: Difference between AEP based on REWS and REWS with wind veer included

wind speed representation experienced by the whole rotor area. The difference in wind direction at different heights compared to hub height is small as can be seen from the scatter plot of the REWS and REWS with veer included in Figure 6.6. As a consequence of the wind veer, a slightly smaller REWS is found.

Consequentially, a comparison between the power curves will not give a large difference. However, the difference of the AEP based on REWS with veer included to the AEP based on REWS is calculated to show the effect of wind veer. In Figure 6.7, the relative increase in AEP can be seen for several annual mean wind speeds. The increase in AEP was expected since wind veer inclusion leads to lower wind speeds while the corresponding power outputs remain the same, which improves the power curve. This compensates the decrease in power curve and AEP by using REWS instead of hub height wind speed partly.

6.1.3 Yaw misalignment

YM is a factor that can result in power losses as discussed in subsection 3.1.3. Therefore, it is interesting to look into this parameter and its effect on the power performance. First, the YM of the turbines during the measurement campaign is determined by subtracting the nacelle direction from the wind direction measured by the Lidar at hub height. It should be noted that the nacelle direction and wind direction measurements of turbine N03 were first adjusted as discussed in subsection 5.1.3 using the measurements of turbine N04.

Before YM distributions for both turbines are made, the data is filtered. The YM effect on power loss is the largest between 4, just above cut-in wind speed, and below 16 m/s, which is above rated wind speed. Below 4 m/s the turbine does not produce significant power, so YM will not result in large power losses. Also, when YM above rated wind speed occurs, the wind speed perpendicular to the wind turbine will still be sufficient so that the turbine can produce the maximum, i.e. rated, power. In addition to the wind speed filter, the measurement sectors are filtered, because in disturbed wind conditions the real

(a) Histogram of YM   (b) Scatter plot of YM against wind speed
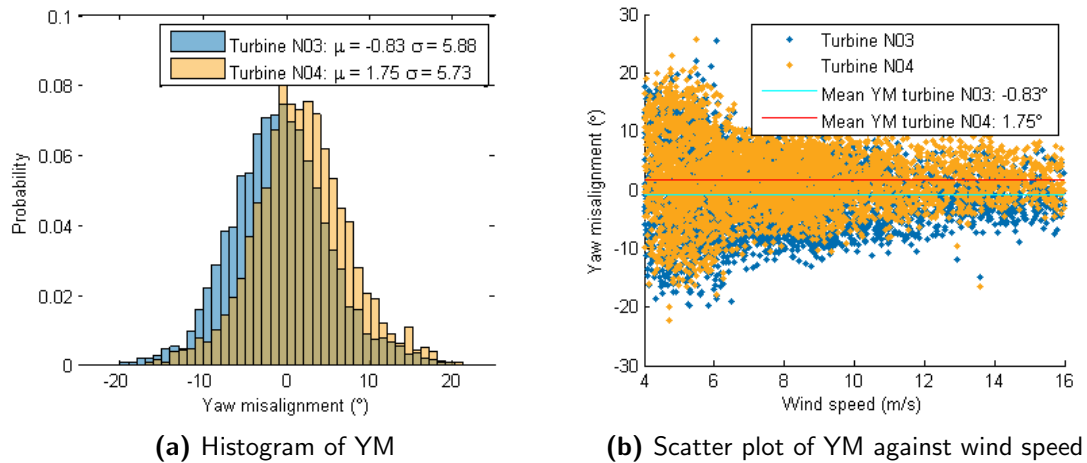
Figure 6.8: Filtered YM measurements of turbine N03 and N04 using Lidar

wind direction cannot be measured accurately. The histograms with the filtered data are shown in Figure 6.8a. Also, the YM is plotted against the wind speed in Figure 6.8b including the mean YM of both turbines.

The histograms show a normal distribution with a similar spread, but turbine N04 is slightly shifted to the right. This is caused by the higher mean YM of turbine N04 as seen in the scatter plot, although this value is precarious due to the manual adjustment. It can also be seen that at lower wind speeds higher YM occurs as a result of the turbine starting up for example. When this is the case, the turbine starts yawing into the right direction, which leads to a temporal YM. At higher wind speeds, the turbine is continuously in operation and yawing which results in lower YM and subsequently less scatter around the mean YM.

The mean YM values are low compared to earlier studies, but a difference between the mean values can be observed. Turbine N04 has a larger YM on average than turbine N03, which could explain the lower AEP values from the previous sections. However, the effect of YM on the power curves should first be investigated more extensively before this can be concluded. This will be done by evaluating power curves for different YM bins.

A Matlab function developed by Goossens is used to evaluate the behaviour of the power curve for several YM bins. Each bin contains wind speed measurements of the Lidar, corresponding to the air-density normalized REWS measurements, and power outputs from the turbine data. From these measurements, a cubic least squares fit is performed on all measurements below rated power for each bin as indicated by the following equation:

$$P = cV^3 \tag{6.1}$$

where c represents the cubic fit parameter. Before the calculations are made, additional filters are applied to the data next to the measurement sector and wind speed as discussed above. First, the maximum wind speed is reduced to 13 m/s. Also, the turbine should produce below rated power. A minimum number of data points in each YM bin is set to 25 and the R^2-values are only plotted above 0.7 to maintain a sufficient fit. An example is shown in Figure 6.9 with YM between 2° and 6° for turbine N03.
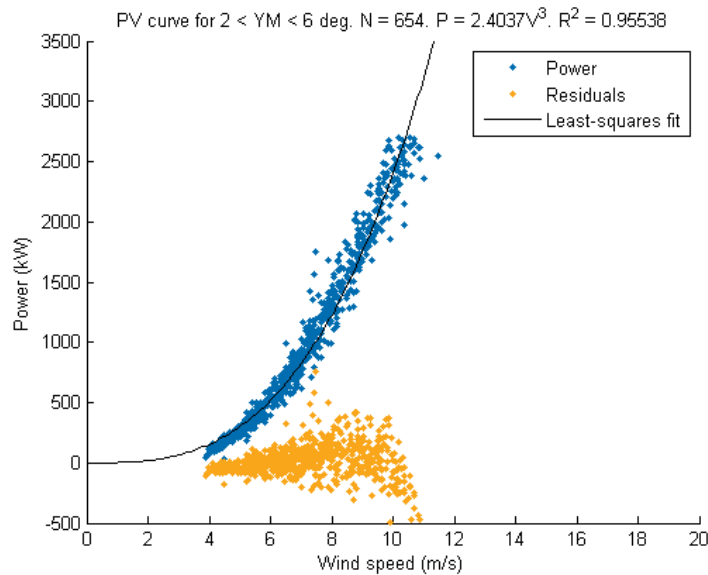
Figure 6.9: Power curve fit using cubic least squares method with YM between 2° and 6° for turbine N03

The calculations are performed for several YM bins between -18° and 18° with a 4° width and for both turbines. Hereafter, the effect of YM on the power curve can be calculated and compared to other studies that were discussed in subsection 3.1.3. To keep the graphs clear, the power losses as well as the R^2-values are displayed for each turbine individually in Figure 6.10a and Figure 6.10b.

The power losses are plotted as the ratio of the cubic fit parameter over the normalized power output for zero YM. The curves seem to follow the cos^2 as found by Pedersen et al.[38] or cos^3 as found by Kragh and Hansen[29] quite well with a small shift in the YM. So, the same analysis was performed as by Goossens but with a different outcome. The shift can be observed by the peaks around -5° for turbine N03 and around 5° for turbine N04. This means a higher power output under a YM of ±5°. Since the directions of the wind speed and nacelle from turbine N03 are adjusted, it is not recommended to analyse the behaviour of this turbine under YM further. Therefore, a concluding result cannot be made yet on the lower performance of turbine N03 compared to turbine N04.

Interestingly, the results of turbine N04 are in accordance with Goossens as he suggested a power increase with a small positive YM. This is explained by the favourable angle of attack at the higher half of the rotor swept area as a result of the positive YM. In combination with the wind shear, which leads to higher wind speeds at higher heights, this results in a higher power output. To conclude, the suggestion of Goossens seems legit from the results at Prinses Alexia.

Furthermore, the effect on the AEP will be touched upon. In this case, all wind speeds are taken into account. First, the data is filtered for several YM bins using a 4° bin width. Only the YM bins where the power output reaches rated power at rated speed are analysed. An annual mean wind speed of 7.12 m/s is chosen, since this is the mean wind speed at Prinses Alexia from one year measured by the met-mast. Turbine N03 is also evaluated to see its performance at a specific YM, although the exact YM is still unknown

(a) Turbine N03 power loss   **(b)** Turbine N04 power loss
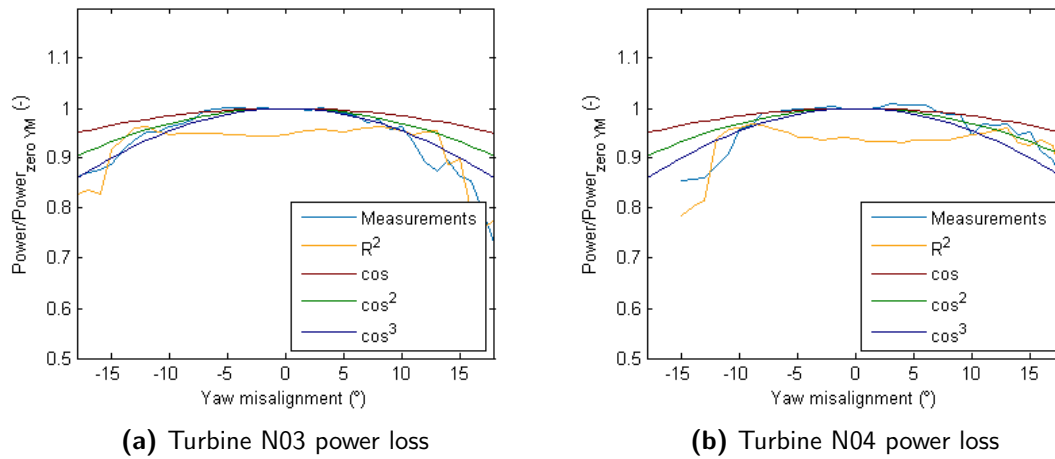
Figure 6.10: Effect of YM on power loss in comparison with $\cos^n$-relations
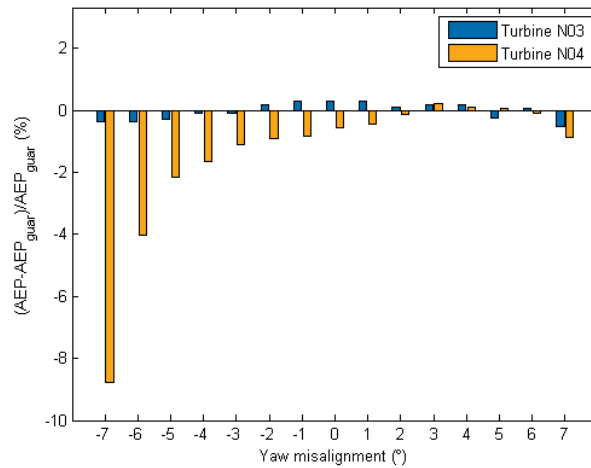
Figure 6.11: Difference between AEP as function of YM with bins of $4°$ width and the guaranteed AEP

due to the adjustment in turbine direction. The differences between the AEP calculated for YM bins between $-7°$ and $7°$ and the guaranteed AEP are shown in Figure 6.11, because the larger YM bins contained significant less data.

As can be seen in Figure 6.11, a small gain for turbine N04 in AEP is reached at $4°$ YM and for turbine N03 around $0°$ YM. However, the AEP calculations depend significantly on the minimum number of observations per bin, which was defined to be 3 (30 minutes of sampled measurements). In the wind speed bins above rated wind speed, where the power output is relatively high, a single measurement has a large effect on the bin average of the bins with a low number of observations. This occurs at higher YM, since the turbine tries to minimise this. Consequently, the AEP calculation can be skewed by this effect. Looking back to the negative AEP difference between REWS and hub height wind speed in Figure 6.3 and the small positive effect on AEP by including veer, filtering for YM has mostly a positive effect between $3°$ and $5°$. Thus, the suggestion of Goossens that a small

YM increases power performance is not undermined.

6.1.4   Turbulence intensity

Another factor that affects the power curve is TI as discussed in subsection 3.1.1. The effect of it will be investigated by analysing power curves measured by Lidar for different TI values as done in the previous section for YM as well. Also, a normalisation of the power curve to a reference TI as well as to the site specific TI will be applied which will be discussed in chapter 7.

Figure 6.12 shows the TI distribution during the measurement campaign at Prinses Alexia from Lidar measurements at 98 m. The filtered and unfiltered measurements are shown from which can be seen that for example wakes result in high TI values. The histogram seems to follow a Weibull distribution where a TI of approximately 0.095 has the highest occurrence in case of all measurements and 0.085 for the filtered measurements.
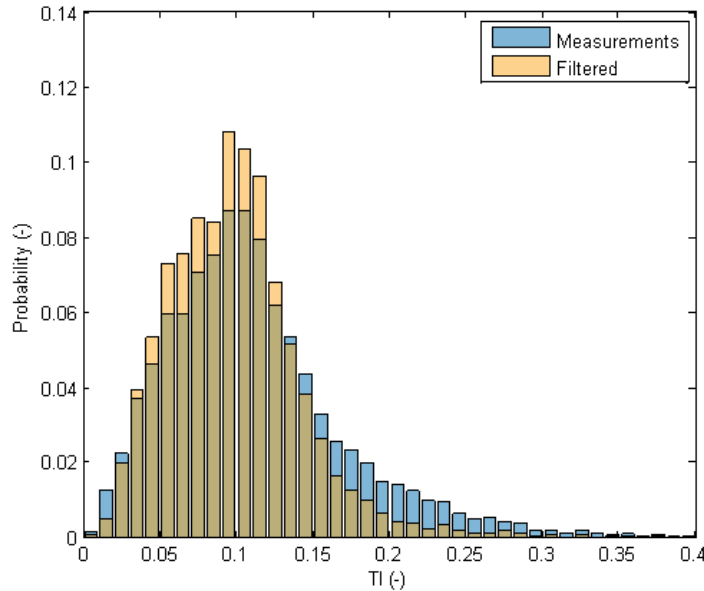
Figure 6.12: Histogram of TI measurements using Lidar at Prinses Alexia

The scatter plot in Figure 7.7 shows the TI measurements after filtering for the measurement sectors. Also, the mean is given to show the scatter around this value. In addition, the TI values binned for wind speed bins with a 0.5 m/s width are shown. These values are compared to the binned values from the met-mast to see the difference in TI measurements. Interestingly, a similar comparison was made by Wagenaar et al. shown in Figure 6.13b. Again, it is important to take the large distance into account which was not the case in [55]. This can cause the larger difference between the TI values, but a similar trend can be observed. To conclude, the TI measurements of the Lidar should be used with care as explained above.

The Matlab function for analysing power curves under YM developed by Goossens is adjusted to analyse the effect of TI on the power curves similarly. A cubic least square

(a) TI measurements at Prinses Alexia

(b) TI measurements of a Wind Iris and met-mast from Wagenaar et al.[55]
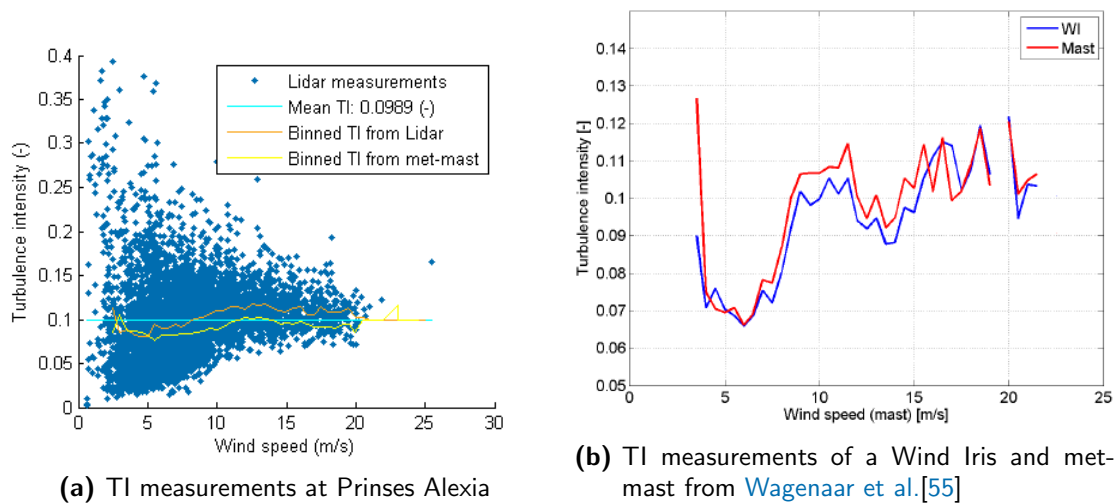
Figure 6.13: Comaprison of TI measurements at Prinses Alexia using Lidar and met-mast against literature

fit is performed for TI bins with a 0.02 width. This fit is used to find a constant that relates power to the wind speed cubed ($P \sim V^3$). The calculated power curve at zero TI is taken as reference and the ratios of each power curve over this reference are shown in Figure 6.14a and Figure 6.14b. A similar trend can be observed for both turbines while the effect of TI is slightly larger on the power ratio of turbine N03. It can also be seen that the optimal TI is determined to be 0.07 or 0.24. The latter TI primarily occurs at low wind speeds as shown in Figure 7.7. Consequently, this peak can be explained by Figure 3.1 which shows a higher average power at low wind speed due to TI. So, this peak does not represent the whole power curve well. A TI of 0.07 would therefore be seen as the optimal TI at wind speeds up to rated wind speed.

Next, the effects of TI on the AEP is examined by calculating the AEP for different TI bins with a 0.04 width and an annual mean wind speed of 7.12 m/s at Prinses Alexia. In Figure 6.15, the differences are shown between the AEP of different TI bins and the AEP calculated for TI between 0.08 and 0.12, which is close the average TI measured at Prinses Alexia of 0.099. It can be seen that a TI of 0.08 is optimal for both turbines. Higher TI values affect the turbine performance negatively, as well as a too low TI. This is confirmed when looking at the ratios for the power curves. Since the optimum TI value is 0.08, it is expected that for this value the positive effect on the power output at the lower wind speeds exaggerates the negative effect around rated wind speed.

6.1.5 Inner vs outer envelope conditions

A power curve delivered by a turbine manufacturer is only guaranteed under certain TI and wind shear conditions, so-called 'inner-envelope' conditions. The individual effects of these parameters on the power curve are discussed in subsection 6.1.1 and subsection 6.1.4. It has not yet been discussed what inner-envelope conditions mean for the power curve guarantee. In this section the combined effect of the parameters will be presented to indicate the consequences of a limited power curve guarantee.

(a) Turbine N03   **(b)** Turbine N04
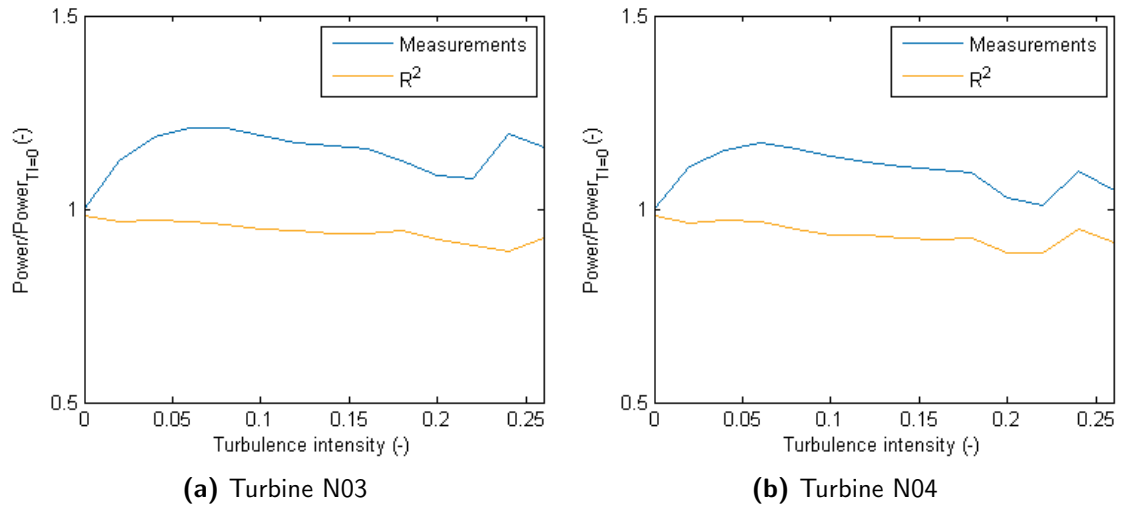
Figure 6.14: Power as function of TI normalised over power at TI=0.10
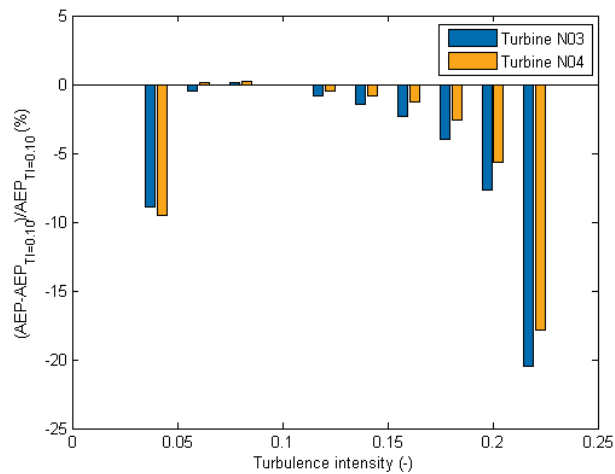
Figure 6.15: Difference between AEP as function of TI and AEP for TI=0.10

(a) Lidar   **(b)** Met-mast
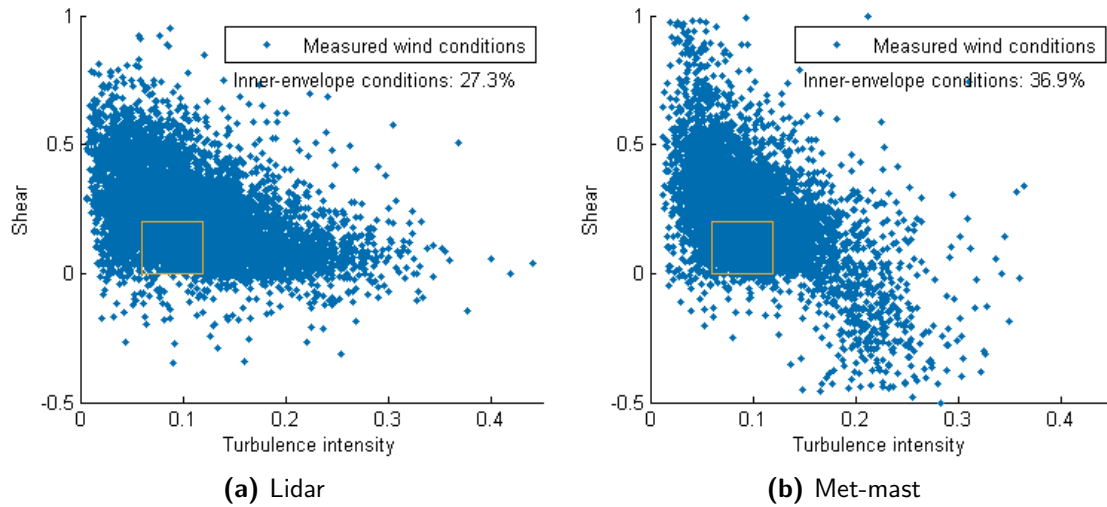
Figure 6.16: Wind shear and TI measurements at Prinses Alexia including an 'orange' contour around the inner conditions

In Figure 6.16a, the filtered Lidar measurements of wind shear and TI are shown with a square defining the conditions under which the power curve is guaranteed (TI: 0.06-0.12 and shear: 0-0.2). Only 27.3% of the filtered Lidar measurements with wind speeds above 3.5 m/s during the measurement campaign at Prinses Alexia is valid to compare with the guaranteed power curve. This is lower in comparison with the ratios as found by Wessels and van der Velde. However, these analyses were performed with met-mast data which could cause some differences in TI and wind shear measurements. To check this, the same scatter plot is made using the measurements of the met-mast at Prinses Alexia in Figure 6.16b from which it can be seen that the ratio found by using the met-mast measurements compares better. This could be caused by the location of the Lidar, which was between two rows of wind turbines, resulting in a higher disturbance in the wind field compared to the location of the met-mast. Therefore, a higher wind shear and TI would be measured by Lidar.

The binned power curves from the inner-envelope conditions are plotted against the power curve of the filtered Lidar measurements. It can be seen in Figure 6.17a and Figure 6.17b that they compare well. A more detailed comparison is made by comparing the AEP for different annual mean wind speeds in Figure 6.18. The AEP is up to 2% higher within the inner-envelope conditions compared to that of the filtered measurements. When taking into account the ratio of 27% between the inner-envelope conditions and the complete range of wind conditions, the turbine generates approximately 0.75% less in AEP than guaranteed at a annual mean wind speed of 7 m/s.

(a) Turbine N03

(b) Turbine N04
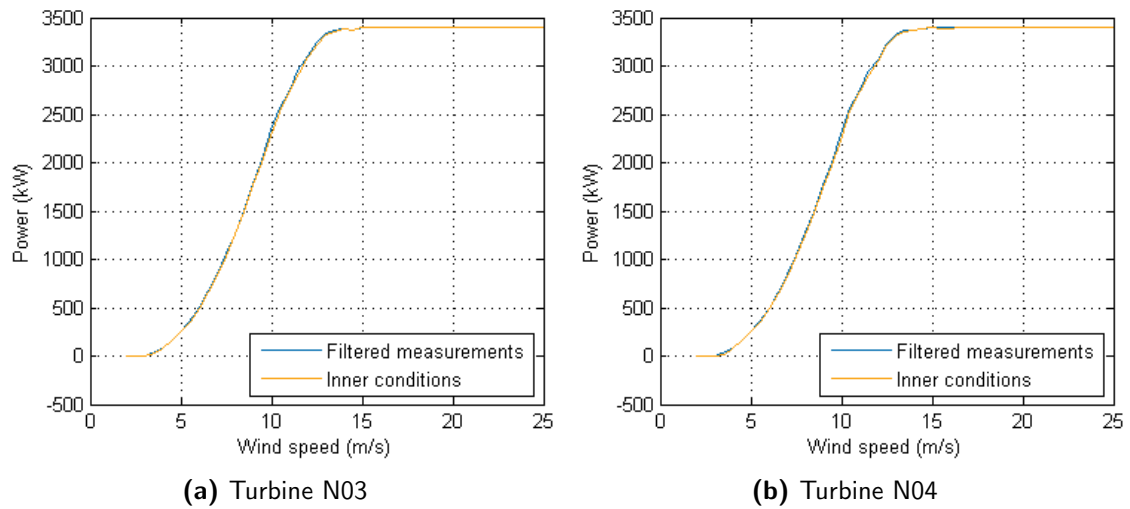
Figure 6.17: Power curves of filtered measurements and inner-envelope conditions
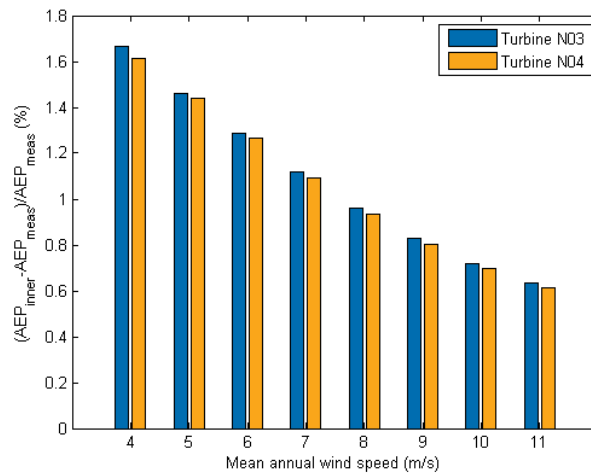
Figure 6.18: Difference between AEP of inner-envelope conditions and AEP of complete envelope using filtered Lidar measurements

6.2   Nørrekær Enge

In this section, the PCV of turbine 4 at Nørrekær Enge is presented using different measurement devices. In this way, it is possible to compare PCV with Lidar and spinner anemometers to an IEC-compliant met-mast. Also, the effect of TI on the turbine performance is investigated.

6.2.1 PCV comparison

Each measurement device used at Nørrekær Enge measured hub height wind speed or REWS and will be used to generate a power curve. The wind speed measurements are filtered according to the IEC standard, so the data measured within the disturbed measurement sectors is excluded as well as erroneous measurements. In addition, air density and, if applicable, tilt corrections are performed according to subsection 2.4.11.

The first power curve is obtained using the hub height wind speed measurements of the met-mast (Figure 6.19a). Hereafter, the REWS measurements of the two Lidars are used to plot the power curves in Figure 6.19b and Figure 6.19c. The last power curve is plotted in Figure 6.19d with the free wind speed measurements of the spinner anemometer. It can be seen that the unfiltered power curve of the met-mast shows large scatter, but this is reduced by filtering the data. This can also be observed in the power curve obtained with the ZephIR Lidar. So, when the met-mast and ZephIR Lidar measure in the disturbed measurement sectors, the measurements are significantly affected. On the other hand, the scatter in the power curves of the Avent Lidar and spinner anemometer remains similar after filtering. However, the number of data points before filtering in case of the Avent Lidar is already lower than the other measurement devices. This could cause the lower scatter in the power curve of the Avent Lidar since disturbed measurements, which may be collected during low availability as a result of disturbed wind conditions, could be excluded.

Next, the binned power curves are shown in Figure 6.20. The power curves compare well to each other, but the power curve determined with the Avent Lidar lies slightly lower. This is caused by the small overestimation of the wind speed measurements compared to met-mast as discussed in subsection 5.2.3. To analyse the power curves better, the difference between the binned power outputs from the measurement devices and the guaranteed power curve is presented in Figure 6.21a. The differences are presented for wind speeds below rated, since above rated wind speed the power does not change. According to the higher binned power between 6 and 11 m/s in case of the met-mast, ZephIR Lidar and spinner anemometer, the turbine seems to perform better than guaranteed. The ZephIR Lidar and spinner anemometer compare well to the met-mast. The effect of the overestimation in wind speed by the Avent Lidar can also be clearly seen from the differences for each wind speed bin. At low wind speeds, the effect of a wrong measurement with a large power output is significant which could cause the positive difference of the Avent Lidar at 5 m/s.

Also, the differences in AEP are given in Figure 6.21b. Again, the negative effect on turbine performance using the REWS measurements can be observed. The AEP calculations using the measurements of the ZephIR Lidar lie close the met-mast. As a consequence of the higher power output from the spinner anemometer measurements compared to the other measurement devices between 7 and 11 m/s as seen in Figure 6.21a, the AEP is significant higher.

Furthermore, the scatter around the power curves is compared for the different measurement devices in Figure 6.22. A low scatter can help to improve turbine monitoring as well as to find causes of underperformance. As can be seen, the spinner anemometer shows the lowest scatter at low wind speeds, but around rated wind speed a peak was observed. A smaller peak also occurs for the other measurement devices around rated

(a) Met-mast

(b) Avent Lidar

(c) ZephIR Lidar

(d) Spinner anemometer
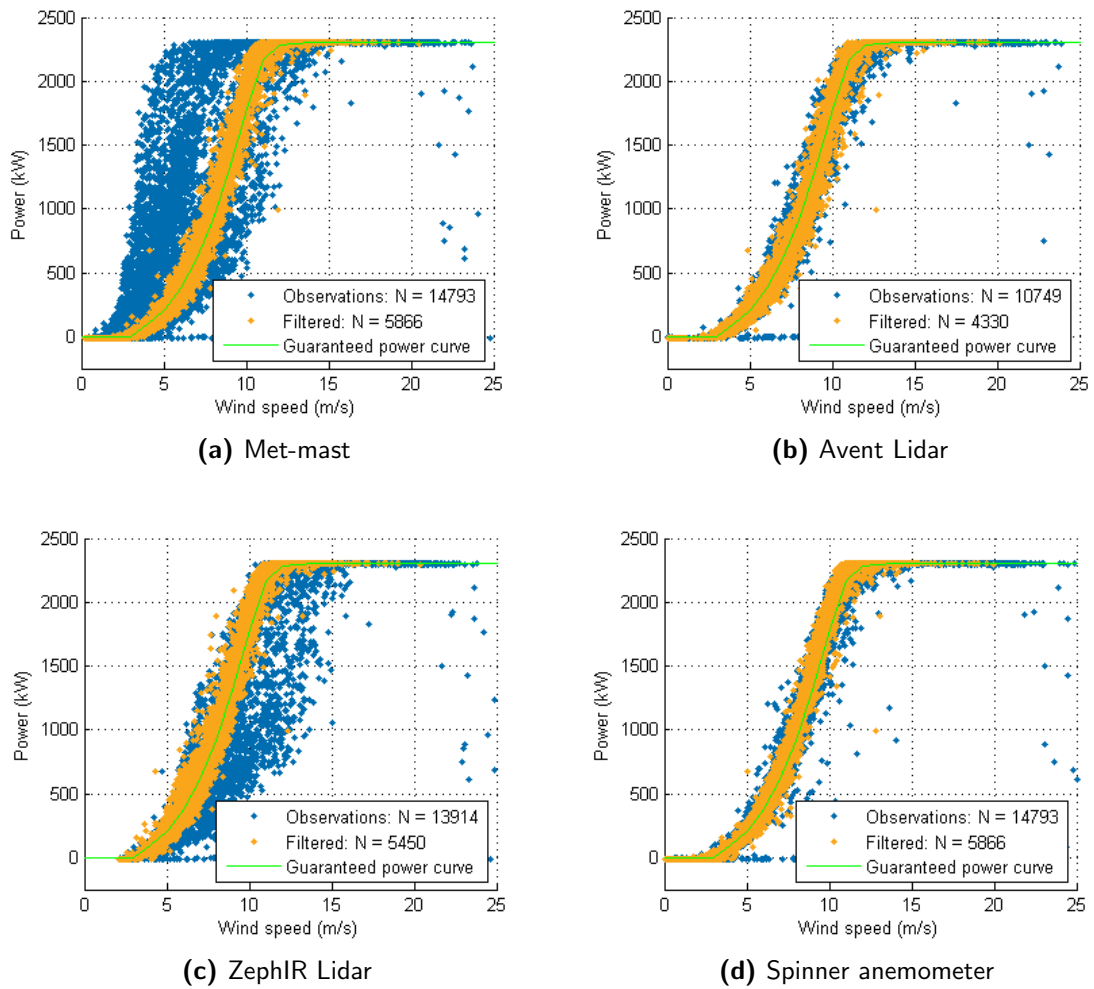
Figure 6.19: Power curves obtained with the measurement devices at Nørrekær Enge
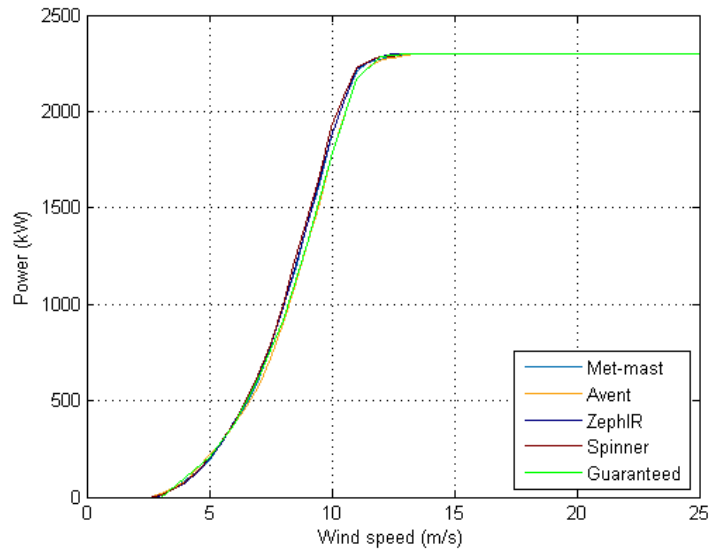
Figure 6.20: Binned power curves

(a) Power curves

(b) AEP
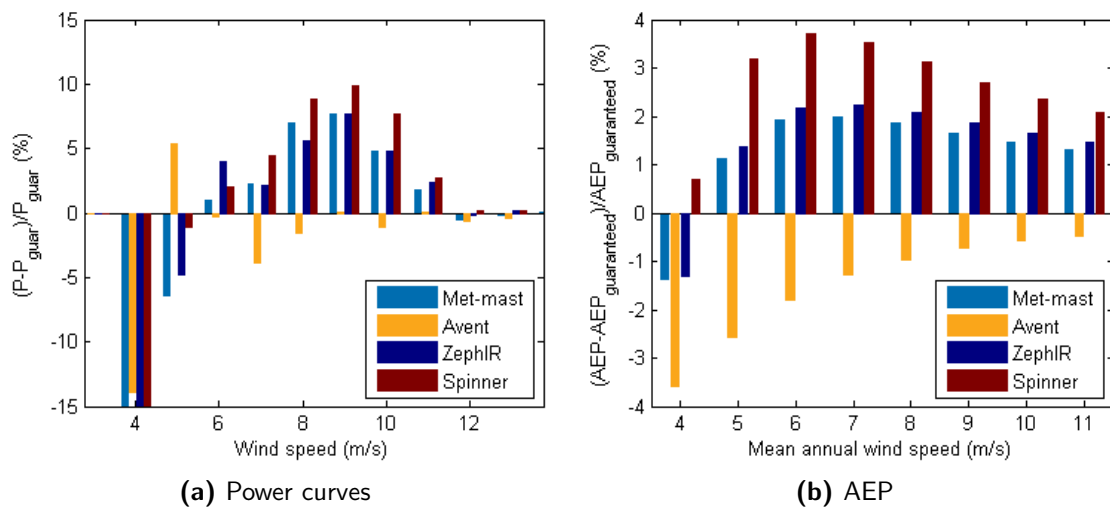
Figure 6.21: Comparison between the measured and guaranteed power curve and AEP
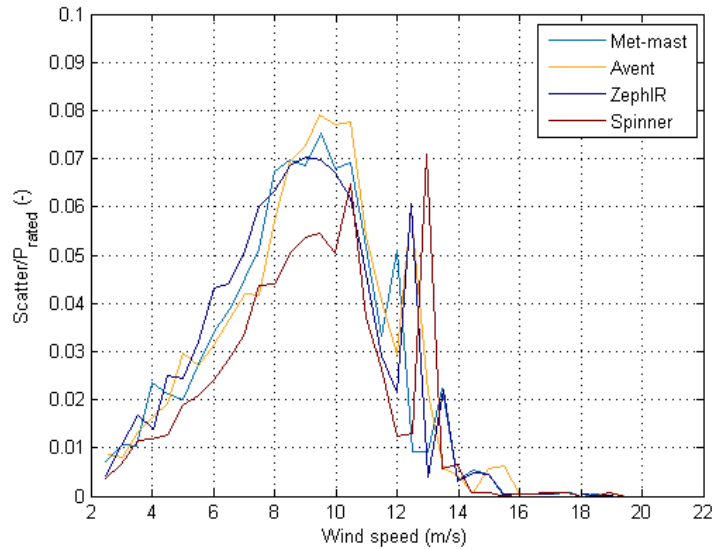
Figure 6.22: Scatter power curves

wind speed. The reduction in scatter around the power curves after correcting for REWS as found by van der Velde cannot be confirmed from the comparison in Figure 6.22 as the scatter calculated for the Avent and ZephIR Lidar power curves, which measured REWS, is similar to the met-mast.

6.2.2 Turbulence intensity

As done for Prinses Alexia with measurements from a ground-based Lidar, the effect of TI on power curves will be investigated on turbine 4 of Nørrekær Enge. Now, it is possible to perform the analysis using different measurement devices. Also, a normalisation of the power curve to a reference TI as well as to the site specific TI will be applied as well for Nørrekær Enge which will be discussed in chapter 7.

Figure 6.23 shows the TI distribution during the measurement campaign at Nørrekær Enge from met-mast measurements. The histogram seems to follow a Weibull distribution where a TI of approximately 0.095 has the highest occurrence in case of all measurements and 0.085 in case of the filtered data. The next analysis will be performed with filtered data because the unfiltered data showed large scatter as seen in Figure 5.15.

First, the effect of TI on the power curves is investigated by performing a cubic least square fit for TI bins with a 0.02 width which was also done for Prinses Alexia. The ratios of the different power curves over a reference power curve are shown in Figure 6.24 for all measurement devices. The power curve at a TI of 0.10 is taken as reference, because there was not enough data at zero TI. Overall, a similar trend can be observed, but the Avent Lidar and spinner anemometer show a bigger decrease at higher TI.

Looking at the scatter plots in Figure 5.15, the Avent Lidar compared better to the met-mast than the ZephIR Lidar and spinner anemometer. Interestingly, the optimal TI for wind speeds up to rated wind speed using the met-mast measurements lies close to 0.10
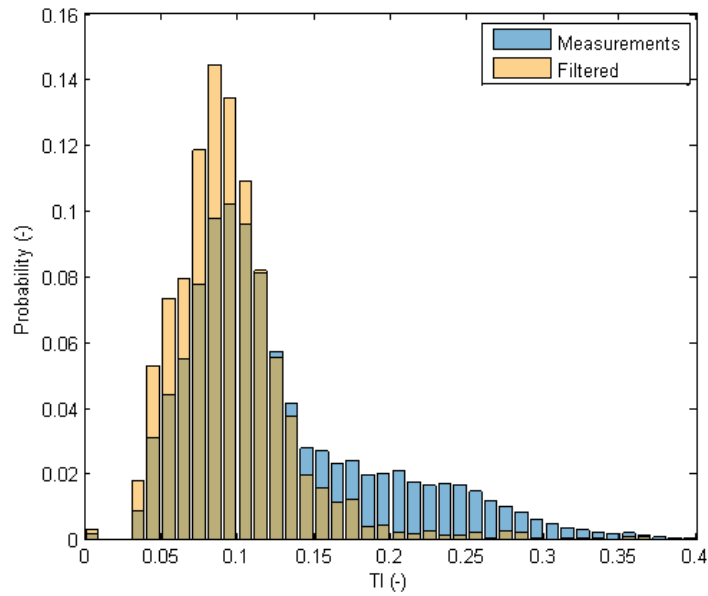
Figure 6.23: Histogram of TI measurements using met-mast at Nørrekær Enge

while the optimum from the Avent Lidar is at 0.02. Furthermore, the optimal TI found for the turbines at Prinses Alexia was 0.08.

Hereafter, the effect of TI on the AEP is investigated as was also done for turbines N03 and N04 at Prinses Alexia. Again, the measurements of all measurement devices are analysed. The AEP calculated for TI between 0.08 and 0.12 is used as reference so that the AEP from the other TI bins can be normalised. From Figure 6.25 can be seen that an average TI of 0.12 would lead to the highest AEP according to most devices. Therefore, it could be suggested that the optimal TI that should be strived for when looking at turbine performance is around 0.10 when taking the optimal TI at Prinses Alexia also into account.

(a) Met-mast

(b) Avent Lidar

(c) ZephIR Lidar

(d) Spinner anemometer
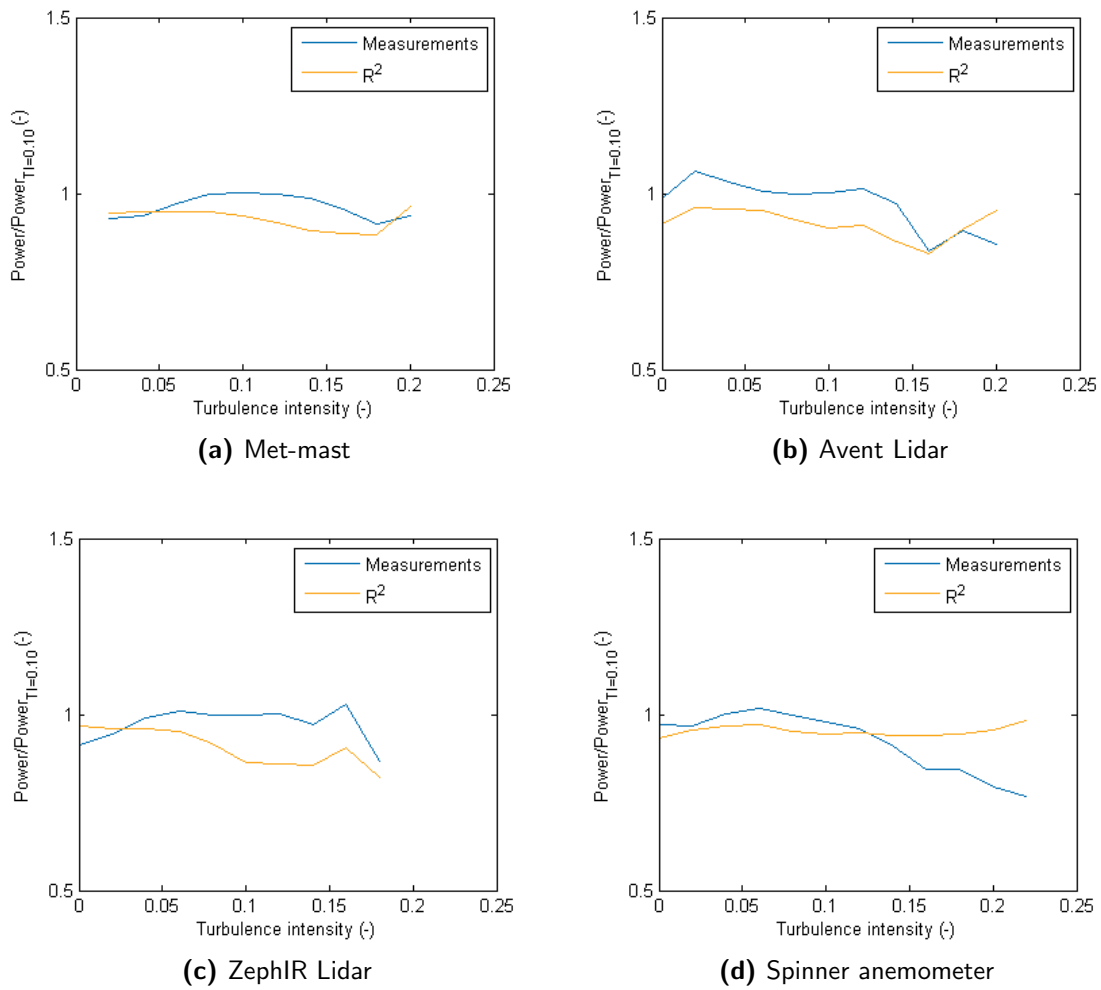
Figure 6.24: Power as function of TI normalised over power at TI=0.10
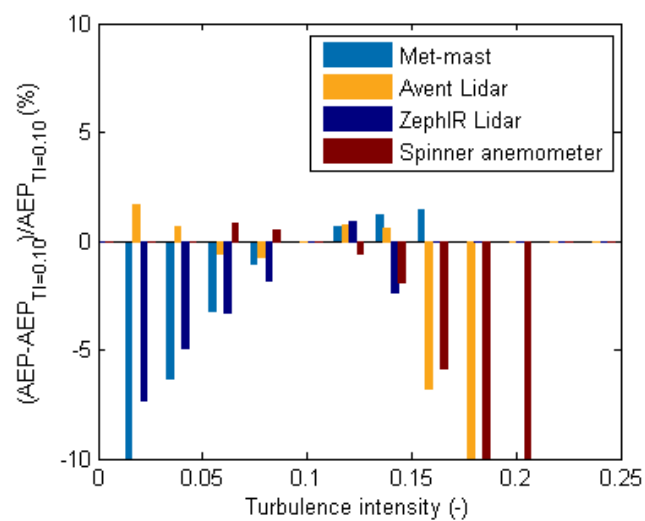
Figure 6.25: Difference between AEP as function of TI and AEP for TI=0.10

Chapter 7

Power Curve Turbulence Normalisation

As mentioned in the previous chapter, turbulence normalisation of power curves will be discussed in this chapter. Power curves for different TI can be obtained by performing measurement campaigns and filtering the measurements in TI bins. The resulting power curves corresponding to a specific TI can be compared to each other so that the effect of TI can be determined. Then, it is possible to provide TI and subsequently site specific power curves. However, this process is time-consuming since TI is not the only parameter that influences turbine performance. Therefore, a procedure was presented in the IEC standard of 2016 which provides a turbulence normalisation of power curves based on simulated power curves. The turbulence normalisation will be performed on power curve measurements from two turbines at Prinses Alexia and one at Nørrekær Enge.

7.1 Turbulence normalisation method

The steps of the normalisation process to be performed described by the IEC standard are as follows:

a) Determine reference TI

b) Determine initial zero turbulence power curve parameters

c) Determine initial zero turbulence power curve

d) Iterate to obtain zero turbulence power curve

e) Simulate power curves with measured and reference TI

f) Obtain power curve for specific TI

Step a) will be performed by calculating the average TI at the site which will be used as reference or site-specific TI. Hereafter, an initial zero turbulence power curve can be obtained. In this case, a zero turbulence power curve is a representation of a measured power curve under the condition that the TI is zero. This power curve can be determined from the binned power curve which is obtained from measurements.

Setting up the initial zero turbulence power curve starts with defining the rated power $(P_{rated,th})$, which is equal to the maximum binned power value. The wind speed at which the first power from the binned values is larger than $0.001 \cdot P_{rated}$ represents the cut-in wind speed $(v_{cut-in,th})$. Furthermore, the rated wind speed is calculated using equation Equation 7.1[22]. Finally, power has a cubic relationship with wind speed between cut-in and rated wind speed. It should be mentioned that a wind speed distribution between 2.5 and 100 m/s with 0.1 m/s difference is required so that it can be implemented in the next steps.

$$V_{rated} = \left(\frac{2P_{rated}}{\rho_0 C_{P,max} A_{swept}} \right)^{1/3} \tag{7.1}$$

Here, $C_{P,max}$ corresponds to the maximum power coefficient obtained from the measured binned power curve. An example of a first approach, step c), is shown in Figure 7.1. This approach should satisfy the following requirements:

a) A maximum difference of 0.1% between the maximum power of the simulated power curve and the maximum bin average of the measured power curve

b) Less than 0.5 m/s difference between the cut-in wind speed of the simulated power curve and the cut-in wind speed of the bin average of the measured power curve

c) A maximum difference of 0.01 between the maximum power coefficient of the simulated power curve and the maximum power coefficient of the measured power curve

The simulated power can be obtained using Equation 7.2 for all bin-averaged data. Next, using the simulated power as input for Equation 2.21, the simulated power coefficient can be determined.

$$\hat{P}(i) = \int P_{0,th}(v_i) f(v_i, TI_i) dv \tag{7.2}$$

Where $f(v, TI)$ represents the wind speed distribution within a 10-minute period determined by the average wind speed and standard deviation within these 10 minutes. Unless convergence occurred, the rated power, cut-in wind speed and maximum power coefficient should be updated, as these parameters depend on the TI and do not correspond to zero TI, using the following equations:

$$P_{rated,th} = P_{rated,th} - max(\hat{P}) + P_{rated} \tag{7.3a}$$

$$v_{cut-in,th} = v_{cut-in,th} - \hat{v}_{cut-in} + v_{cut-in} \tag{7.3b}$$

$$C_{P,th} = C_{P,th} - max(\hat{C}_P) + max(C_P) \tag{7.3c}$$

Here, P_{rated}, V_{cut-in} and C_P correspond to the values from the measured binned power curve. Via the updated rated power $(P_{rated,th})$ and power coefficient $(C_{P,th})$, the rated wind speed $(v_{rated,th})$ should be updated as well. On the other hand, $\hat{v}_{cut-in}$ is obtained
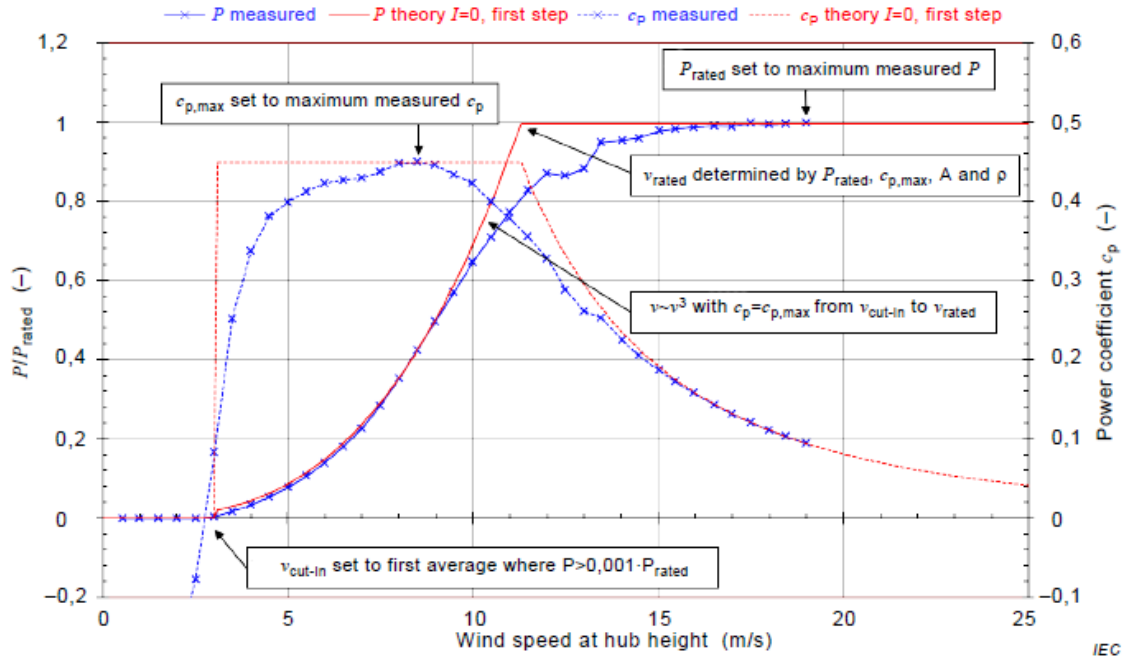
Figure 7.1: Power curve including its initial zero turbulence power curve[22]

from the wind speeds of the simulated power curve using the same requirement as for the initial zero turbulence power curve: the first wind speed corresponds to a power larger than $0.001 \cdot P_{rated}$. The process should be iterated until convergence is reached, which normally occurs after one or two iterations as illustrated in Figure 7.2. Hereafter, a final normalisation should be performed to obtain the zero turbulence power curve using Equation 7.4[22], which should be bin-averaged in wind speed bins of 0.5 m/s. An example of the final result compared to the initial zero turbulence power curve is shown in Figure 7.3.

$$P_0 = \overline{P(v)} - \hat{P}(v) + P_{0,th}(v) \tag{7.4}$$

Here, P_0 represents the final normalised zero turbulence power, $\overline{P(v)}$ the 10-minute average measurements, $\hat{P}(v)$ the simulated power, which is defined by Equation 7.2[22] using the measured wind speed and TI, and $P_{0,th}(v)$ is the initial zero turbulence power. In the ideal case, the 10-minute averages are equal to the simulated power so that the final zero turbulence power curve is equal to the converged zero turbulence power curve, which also implies that the measurements follow the theory.

Finally, the zero turbulence power curve can be used to obtain the measured output normalised to the reference TI. It functions as input for two simulated power outputs using Equation 7.2[22]. The first simulated power curve, $\overline{P_{sim,TI}(v)}$, is based on the wind speed and TI measurements whereas the second one, $\overline{P_{sim,TI_{ref}}(v)}$, is determined by the wind speed measurements and a reference TI corresponding to the specific site. These simulated power curves will be used to normalise the measured power output to a
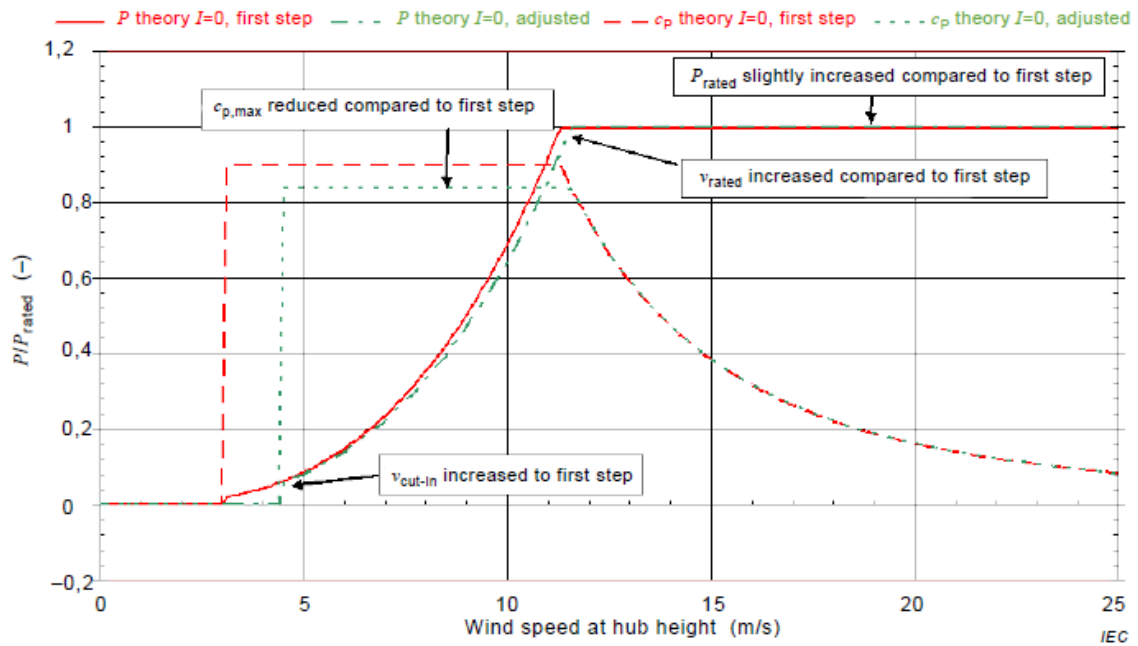
Figure 7.2: Adjusted initial zero turbulence power curve[22]
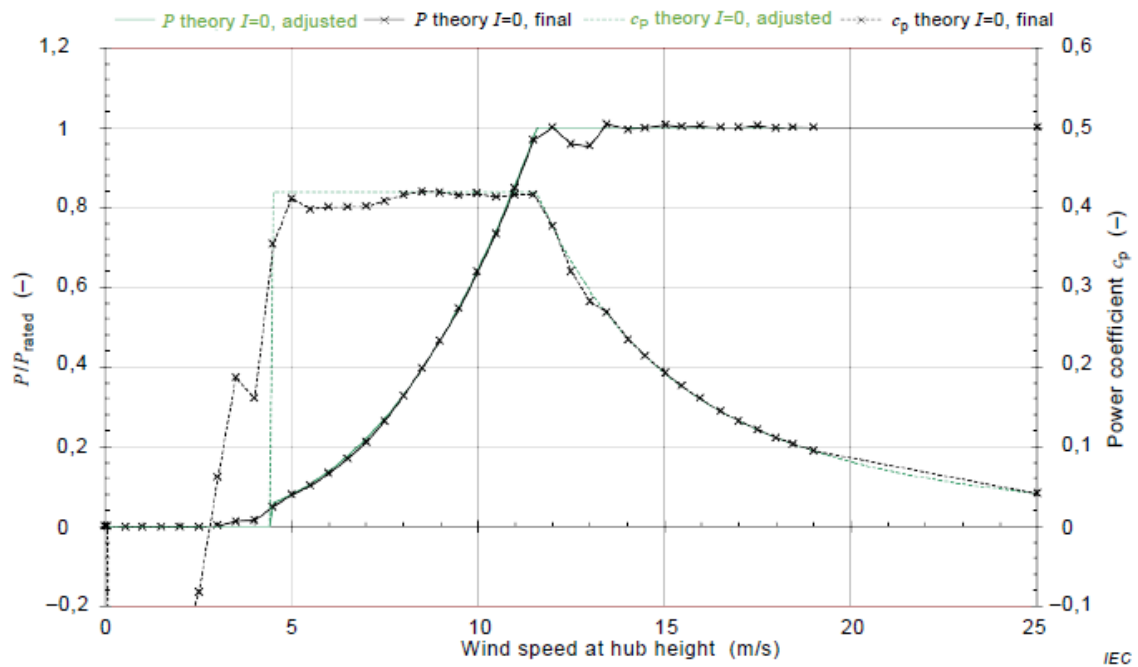
Figure 7.3: Final zero turbulence power curve compared to adjusted initial zero turbulence power curve[22]

reference TI according to the IEC standard (Equation 7.5).

$$\overline{P_{TI_{ref}}(v)} = \overline{P(v)} - \overline{P_{sim,TI}(v)} + \overline{P_{sim,TI_{ref}}(v)} \tag{7.5}$$

A turbulence normalisation is performed in Appendix F to clarify the process and to show the effects of the normalisation on a power curve. From this example can be seen what can be expected in reality when performing a turbulence normalisation of power measurements. This will be used as background to verify the turbulence normalisations that will be performed with real measurements in the following sections.

7.2 Prinses Alexia

For Prinses Alexia, Lidar measurements will be used to perform the power curve turbulence normalisation on turbines N03 and N04, because a met-mast was too far located from the turbines. Moreover, the focus of this thesis is on the applicability of Lidar in wind turbine monitoring. The reference TI used for the normalisation is determined to be 0.099, which is equal to the mean TI measured by the Lidar at Prinses Alexia. It should be noted that the TI measurements of Lidar are still in debate as discussed in subsection 3.1.1.

7.2.1 Zero turbulence power curve

Next, the initial approach of a zero turbulence power curve and power coefficient are defined and shown in Figure 7.4a and Figure 7.4b as the 'blue' lines. Also the measured and binned power curves of the turbines are plotted in 'red'. Only one iteration was required for both turbines for sufficient convergence and the adjusted power curves are represented by the 'green' lines in the figures. Comparing the initial and iterated zero turbulence power curve with literature as presented in subsection 2.4.12, a similar result is obtained.

The adjusted zero turbulence power curve was corrected once more to obtain the final zero turbulence power curve as illustrated by the 'black' lines in the figures. It is compared to the measured power curve by calculating the difference between the power outputs within the relevant wind speed range for TI effects. As discussed in subsection 3.1.1, a higher TI would increase the power at lower wind speeds and reduce the power at higher wind speeds. As a result, the zero turbulence power curve should show the opposite effect when it is compared to the measured power curve which is affected by TI.

Figure 7.5a and Figure 7.5b clearly show this behaviour, however at 4 m/s the sign changes. This means that the measured bin-average power at 4 m/s is lower than the normalised power. This can be caused by averaging of the data, since at low wind speeds the turbine could be turned off due to too low wind speeds within the 10-minute period while the 10-minute average wind speed could be above cut-in wind speed. Since at low wind speeds the power output is relatively low, a small difference can have large effects.

The initial zero turbulence power curve is zero below cut-in wind speed. As a result, a wind speed distribution around cut-in wind speed will have a lower average power output

(a) Turbine N03   **(b)** Turbine N04
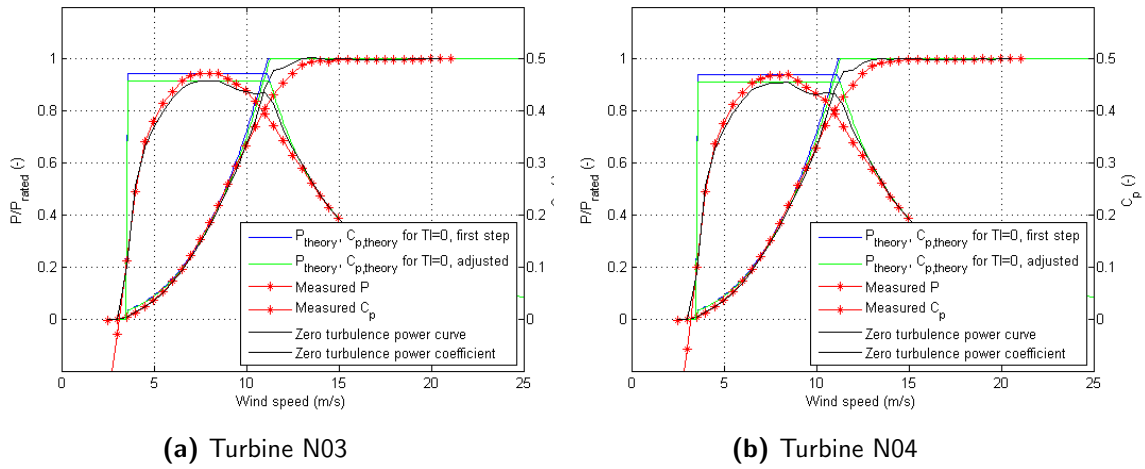
Figure 7.4: Zero turbulence power curve (adjusted and final) compared to initial zero turbulence and measured power curve

than a measured average power output at the same average wind speed close to cut-in. Therefore, Equation 7.4 results in a significant lower power output for the zero turbulence power curve compared to the measured power curve at 3.5 m/s.

The previous results are compared to the simulation results in Appendix F. From the similarities can be stated that the turbulence normalisation to zero TI was performed correctly. Also, the TI effect can be clearly observed when analysing real measurements.

7.2.2 Reference turbulence power curve

The next step is to normalise the power curve to a TI value of interest. This TI value is for example the average TI of a site to analyse the site-specific turbine performance. A comparison is made to the original measured power curve to observe the effects of TI normalisation. This is done by calculating the difference between the power normalised to a specific TI and the measured power curve. The wind speed range is chosen between cut-in and just above rated wind speed, because these were described in subsection 3.1.1 to be of most interest. As seen from Figure 3.1, a higher TI increases power at low wind speeds and reduces power at higher wind speeds. Also, contrary effects can be observed for lower TI values than the measured TI of 0.099. This effect can also be observed in Figure 7.6a and Figure 7.6b when comparing the effects from different TI on the power output. Again, for low wind speeds no clear conclusion can be drawn.

The positive effect on the power curve at low wind speeds seems to improve the turbine performance. However, TI increases the loads on the turbine blades and tower resulting in faster turbine degradation. Also, the unfavourable effects around rated power, where the power is significantly higher than at lower wind speeds, overrule the positive effects. Therefore, a low TI is preferred and should be strived for when allocating wind farm sites. It can be concluded from the results, although consensus is still lacking on the Lidar's ability to measure TI, that Lidar is able to identify the effects of TI on power curves.

(a) Turbine N03   (b) Turbine N04
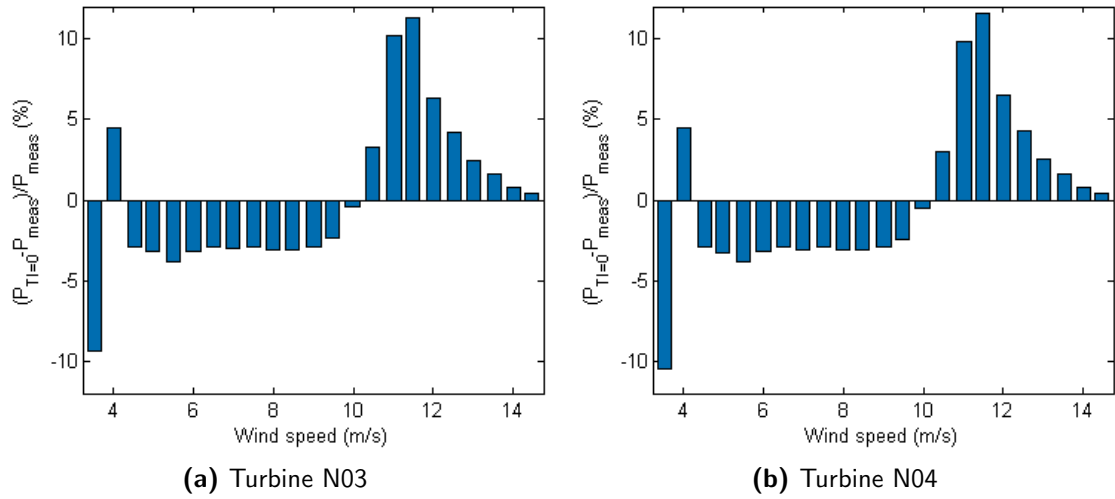
Figure 7.5: Difference between zero turbulence power curve over measured power curve

(a) Turbine N03   (b) Turbine N04
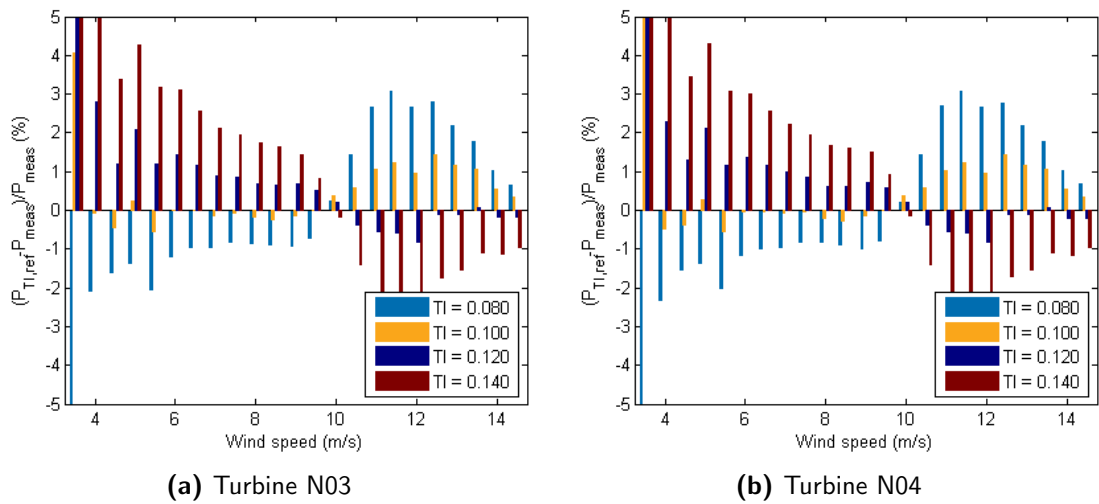
Figure 7.6: Difference between reference turbulence power curve over measured power curve

(a) Turbine N03　　　　　　　　　　　**(b)** Turbine N04
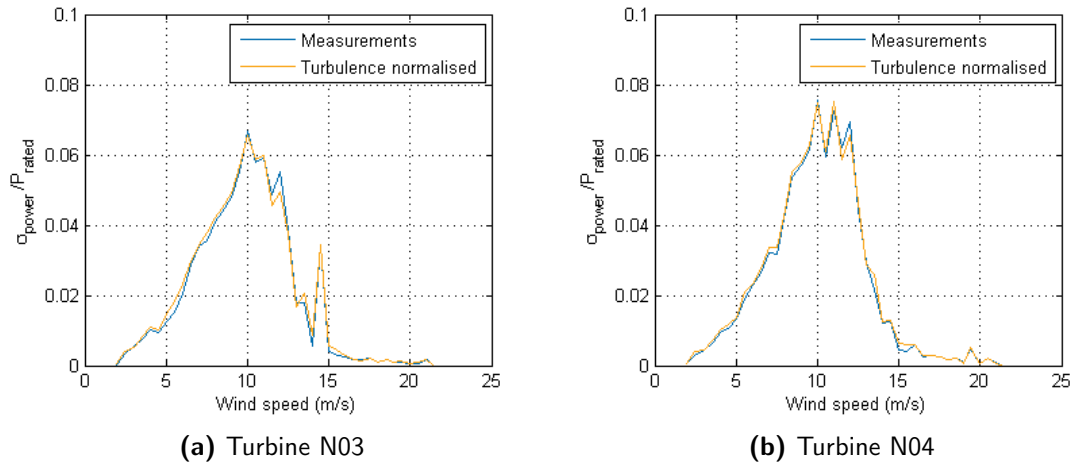
Figure 7.7: Scatter around power curve before and after turbulence normalisation

7.2.3　Scatter around power curve

To answer one of the research questions, the change in scatter around the power curve is checked. When the TI normalisation would improve the approximation of the power in the wind extracted by the turbine, it would be expected that some of the 10-minute power outputs change in a way that they lie closer to the power curve since the TI effect is taken into account. As a result, the scatter would be less compared to the scatter of the measured power curve which was also found in Appendix F by applying the theory of the turbulence normalisation procedure to simulated power measurements. The scatter can be determined by taking the standard deviation of the errors from the power outputs compared to the linear interpolated power curve, where interpolation is performed between each wind speed bin of the bin-averaged power curve.

In Figure 7.7, the scatter shows no significant difference after the turbulence normalisation. Moreover, no improvement was obtained so that the effect of the normalisation on the power curve scatter would be questioned. However, the simulation in Appendix F showed clearly an improvement in the scatter around the power curve. On the other hand, the simulations were made without including other factors such as YM that could influence turbine performance. Therefore, it can be that in reality the scatter around the power curve does not improve because it is affected by other factors than TI only.

7.2.4　AEP

Finally, the effect of turbulence on the AEP is analysed using the normalisation instead of the obtained power curves per TI bin from the measurements as discussed in subsection 6.1.4. The question is whether the negative effect at higher wind speeds around rated will be compensated by the positive effect at lower wind speeds. First, the AEP is calculated for each different power curve that corresponds to a specific TI. Hereafter, each AEP will be compared to the AEP calculated for a TI of 0.10.

The AEP is calculated for two different annual mean wind speeds, because one does not give enough information about the TI effect as seen from Figure 7.8. Two opposing

results are caused by different wind speed contributions. The results of the lower annual mean wind speed show a positive effect for higher TI values, which means that the positive effect of TI at lower wind speeds on the power output exceeds the negative effect at higher wind speeds. It can also be observed that a higher annual mean wind speed affects AEP negatively when TI increases, which is caused by the negative TI effect on the power curve at higher wind speeds. An explanation can be that a higher annual mean wind speed leads to a larger contribution of the power curve at higher wind speeds, hence the negative effect of TI on the power output and subsequently AEP will increase as well. These results are in accordance with the simulation discussed in Appendix F.
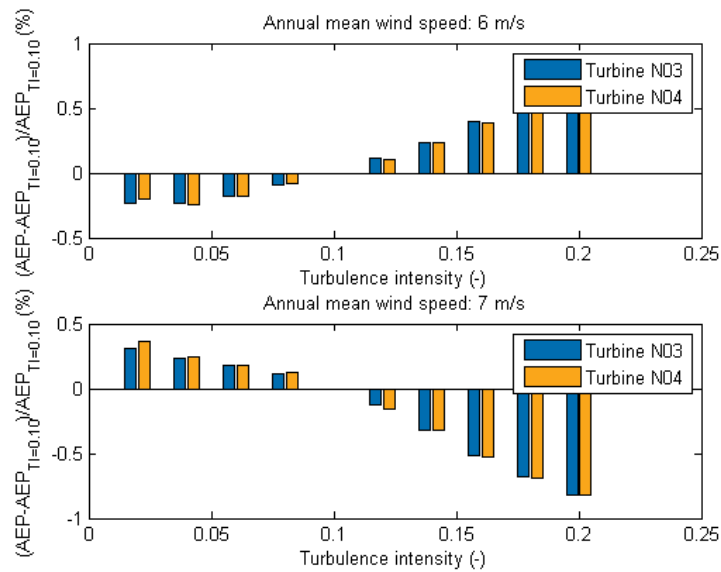
Figure 7.8: Difference between AEP as function of TI and AEP for TI=0.10

7.3 Nørrekær Enge

Several measurement devices were measuring at Nørrekær Enge. In this section, the results of turbulence normalisation between the different devices will be compared to each other. For the calculations, the average TI measured by the met-mast in the undisturbed measurement sectors is used as reference and equal to 0.099, which is accidentally similar to the average TI at Prinses Alexia.

7.3.1 Zero turbulence power curve

The zero turbulence power curves are obtained for all measurement devices by following the procedure from subsection 2.4.12. From the plots in Figure 7.9 can be seen that the zero turbulence power curves compare well to each other. However, the power coefficient plot obtained using the Avent Lidar is slightly higher up to 5 m/s whereas between 5 and 10 m/s it is lower. This can be explained by the fact that the Avent Lidar underestimates wind speed up to 3 m/s as well as TI compared to the met-mast. Since a higher TI at

(a) Met-mast

(b) Avent Lidar

(c) ZephIR Lidar

(d) Spinner anemometer
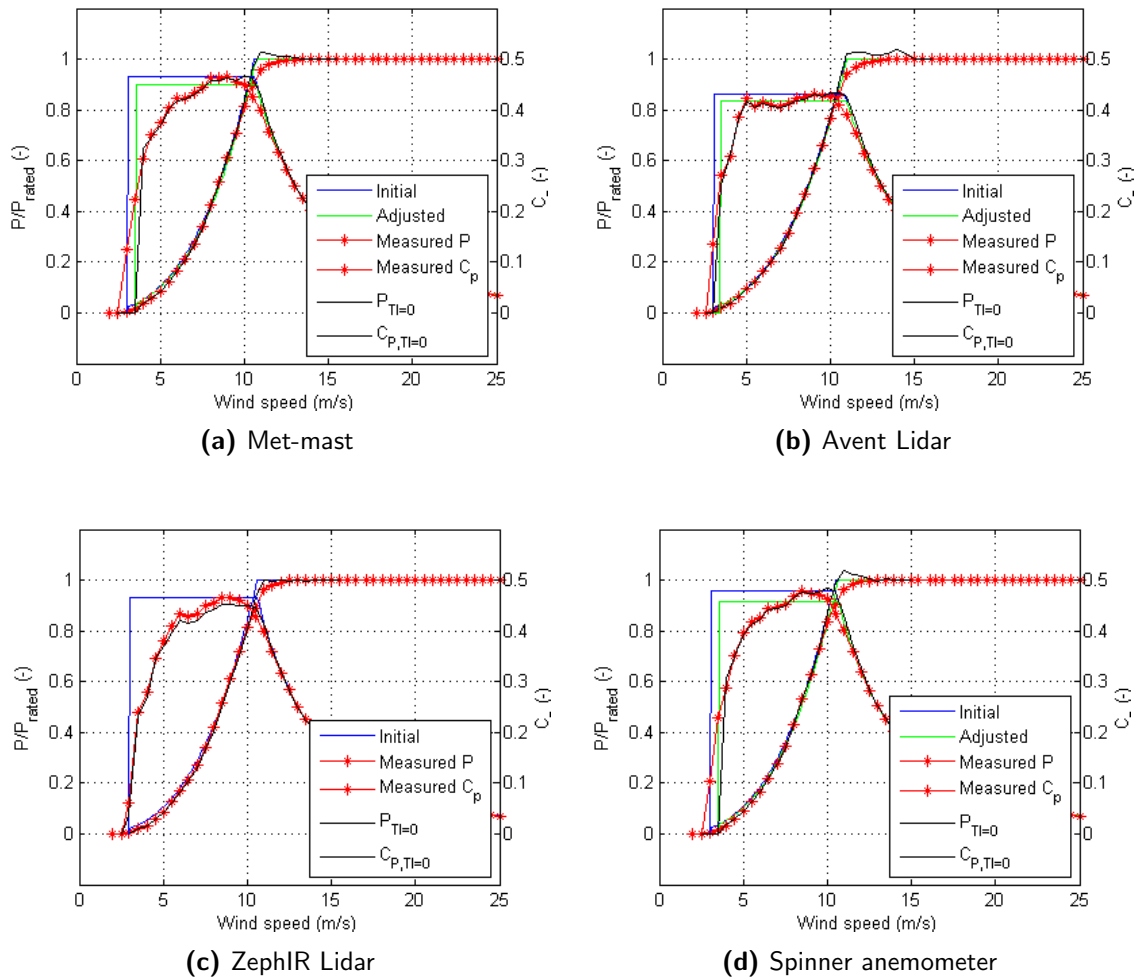
Figure 7.9: Zero turbulence power curve (adjusted and final) compared to initial zero tur-
bulence and measured power curve

low wind speeds affects the power curve positively, a lower TI will result in a smaller
decrease of the power output if it is normalised to zero TI. This results in a slightly larger
power output up to 5 m/s in case of the Avent Lidar compared to the other measurement
devices. At higher wind speeds the Avent Lidar overestimated the wind speed which leads
to a lower power output compared to the met-mast and thus a lower power coefficient.

Similarities in the normalised power curves between the met-mast and the ZephIR Lidar
as well as the spinner anemometer show that the latter two can be used to normalise power
to zero TI. Since the wind speed measurements were found to correlate slightly worse with
the met-mast than the ZephIR Lidar and spinner anemometer as illustrated in Figure 5.10,
care should be taken when using the Avent Lidar for turbulence normalisation.

Also, the difference between the zero turbulence and measured power curves is calculated
to show the changes more clearly. Similar results can be observed in Figure 7.10 for
Nørrekær Enge as obtained for Prinses Alexia, so the theory behind the TI effects on the
power curves is again verified. Also the change in sign of the differences at 4 m/s can be
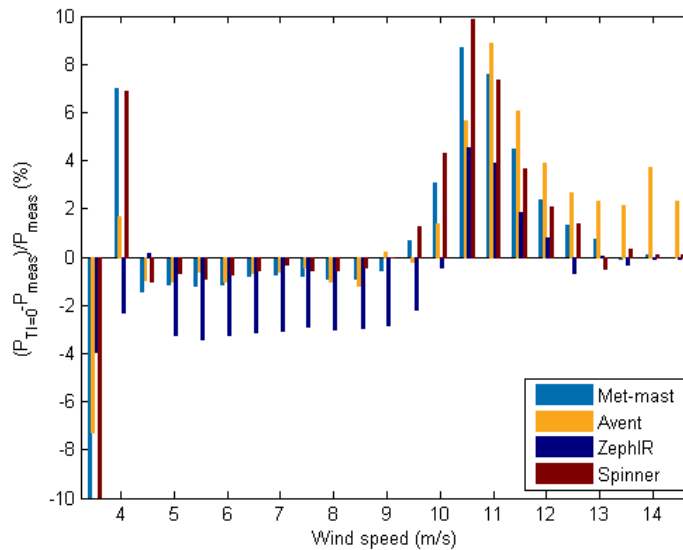
Figure 7.10: Difference between zero turbulence power curve and measured power curve

seen, which could be caused by averaging of the data as discussed in subsection 7.2.1.

Interestingly, the differences between the ZephIR Lidar and met-mast lie significantly lower than the differences between the other devices and the met-mast. The larger negative change in the power curve at low wind speeds could indicate that the ZephIR Lidar measures a higher TI than the other measurement devices, but when looking into the binned TI values the opposite was found. It is not clear what the cause is of this difference compared to the other devices. On the other hand, the smaller increase in power output at higher wind speeds can indeed be the result of lower TI measurements of the ZephIR Lidar as shown in subsection 5.2.6. So, the normalised power curve using the ZephIR Lidar shows overall lower power outputs compared to the other measurement devices. Furthermore, no significant deviations can be seen from a comparison to the simulation results in Appendix F.

7.3.2 Reference turbulence power curve

Now the zero turbulence power curves are defined, the power curves can be normalised to different TI values. These will be compared to the original measured power curve to observe the effects of TI normalisation. The power curves normalised to TI values of 0.06, 0.08, 0.10 and 0.12 are compared to the measured power curve. The results of all measurement devices are presented in Figure 7.11. The underestimation of the TI by the Lidars compared to the met-mast (and spinner anemometer) can be clearly seen from the differences between the power curves. The negative effects at low wind speeds and the opposite at higher wind speeds as a result of normalising to a lower TI, equal to 0.06, in the case of the met-mast and spinner anemometer can be clearly observed, while these TI values show almost no change in the power outputs from the ZephIR Lidar and to a lesser extent also from the Avent Lidar. Therefore, it is important that the TI measurements are reliable to generate site-specific power curves by applying turbulence normalisation.

(a) Met-mast

(b) Avent Lidar

(c) ZephIR Lidar

(d) Spinner anemometer
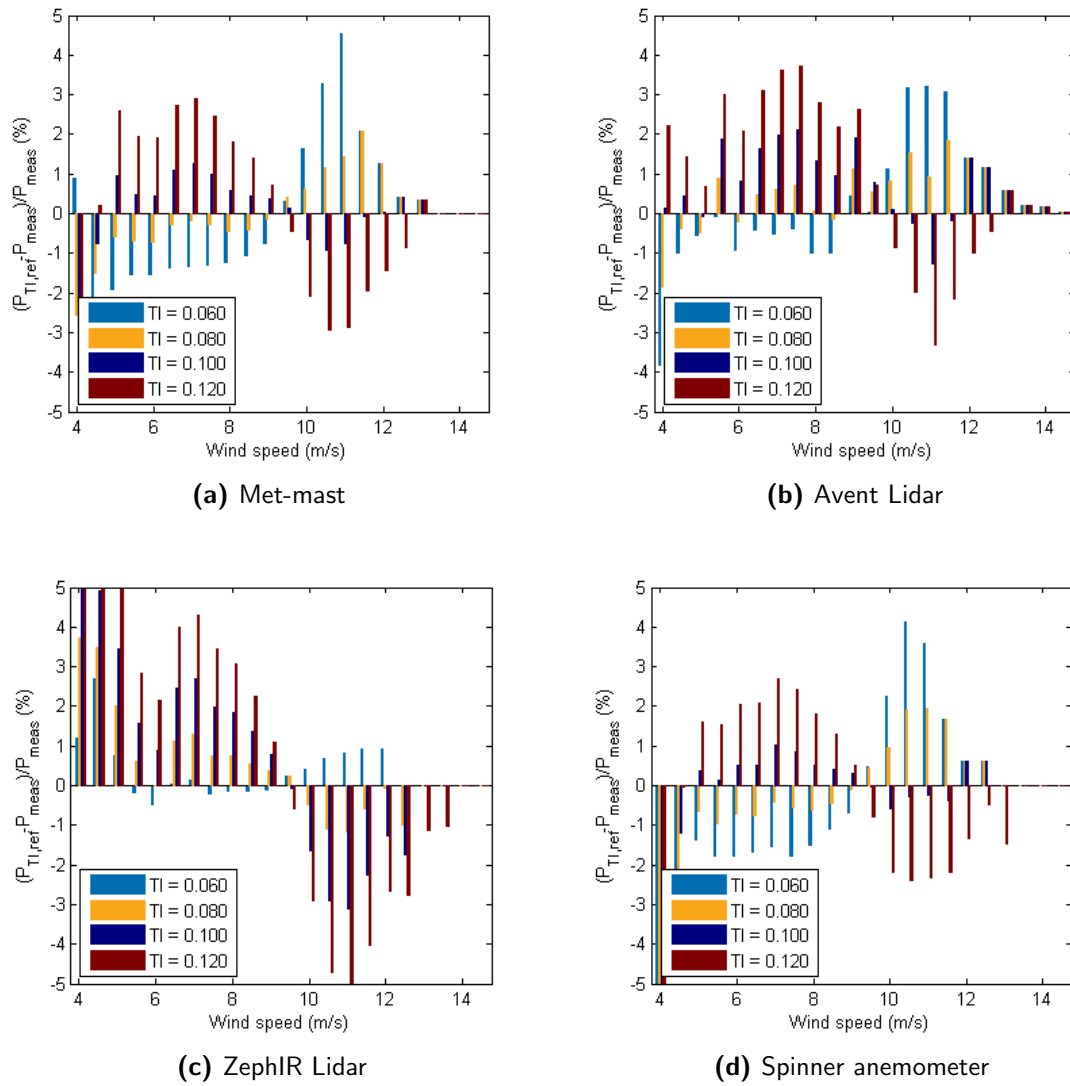
Figure 7.11: Difference between reference turbulence power curve over measured power curve
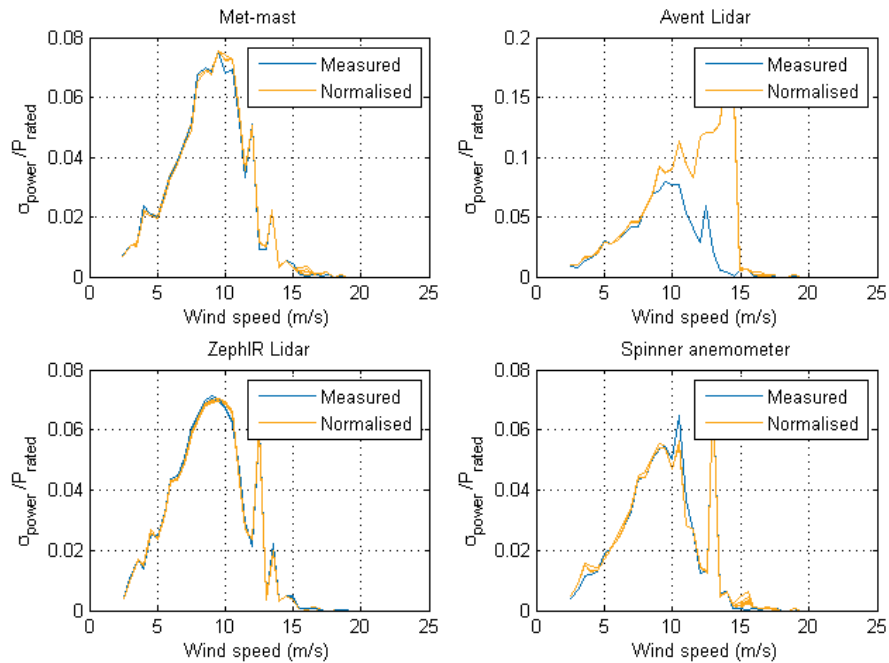
Figure 7.12: Scatter around power curve before and after turbulence normalisation

7.3.3 Scatter around power curve

As also done for Prinses Alexia, the scatter around the power curve is analysed. It was expected that TI normalisation would adjust the power measurements so that they will lie closer to the power curve since the TI effect is taken into account. Again, TI normalisation did not result in lower scatter around the power curve as can be seen in Figure 7.12. Moreover, the scatter in the power curve of the Avent Lidar show some unexpected changes close to rated wind speed. This means that the differences between the power outputs and the power curve increase after TI normalisation.

The other plots show almost no change, so there is an error in the data from the Avent Lidar. As can be seen from Figure 7.9b, around rated wind speed the ratios of the binned power curve lies above 1, which means that the zero turbulence power curve exceeds rated power here. Thus, normalising the measured power can result in significant changes and consequently increase the scatter which occurs in this case around rated wind speed. Again, in case of real measurements no improvement in the scatter can be observed while this would be expected in theory. The same statement therefore holds from Prinses Alexia that other factors could influence the power curve uncertainty more.

7.3.4 AEP

At last, the AEP as function of TI is calculated for two different annual mean wind speeds. The calculated AEP is normalised by dividing it by the AEP calculated for a TI value of 0.10. The results are shown in Figure 7.13 from which similar effects can be observed as seen at Prinses Alexia and discussed in subsection 3.1.1. Indeed, a high TI increases the
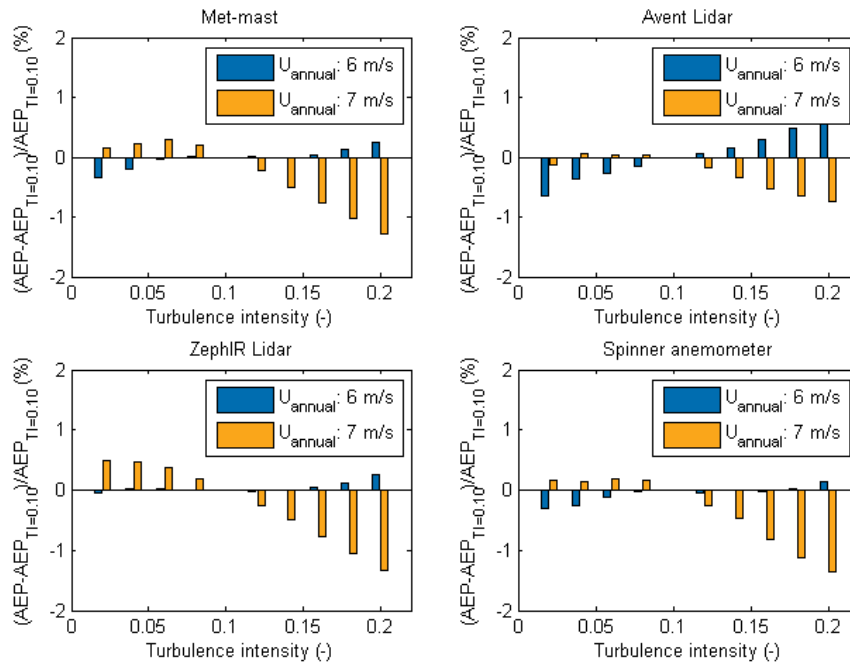
Figure 7.13: Difference between AEP as function of TI and the AEP for TI=0.10

AEP calculated with the lower wind speed, while a lower TI is preferred when the annual mean wind speed is relatively high.

It can also be seen that the difference between the two annual mean wind speeds for one TI value is similar for each device. For example, the two bars at a TI of 0.02 differ ±0.5% in all plots. So, in principle each device could be used to determine the increase or decrease in AEP as a result of a different annual mean wind speed. Since the annual mean wind speed is in general site-specific as well, it seems that each device could be used in case a turbulence normalisation should be performed.

The only big difference between the plots is the larger increase in AEP for higher TI values at an annual mean wind speed of 6 m/s using the Avent Lidar data. Also, the decrease in AEP in case of a wind speed of 7 m/s at higher TI values is lower compared to the data from the other measurement devices. So, the positive TI effect on the power output at low wind speeds exceeds the negative effect of TI at higher wind speeds up to approximately 6.5 m/s. This can be explained by looking at Figure 7.11 in which the changes in power output can be seen for different TI values. A larger increase can be observed in the power output up to 9.5 m/s at a TI value of 0.12 in the plot of the Avent Lidar compared to the other measurement devices. Consequently, higher TI values could increase the power output even more and therefore result in a higher AEP when using the data of the Avent Lidar. In addition, the decrease in power output at higher wind speeds due to a higher TI is less or comparable to the other measurement devices.

Chapter 8

Heterogeneity

In this chapter, the effect of heterogeneity on Lidar measurements will be discussed. As mentioned in section 2.5, simulations will be analysed to gain understanding of the concept of heterogeneity. The simulations will be validated with measurements from a five-beam Lidar at Nørrekær Enge between May and December 2015.

8.1   Method

In theory, a two-beam Lidar is not able to define enough variables for quantifying heterogeneity, because it can only measure the RWS at both beams and there are three unknowns (X, HWS, and YM). A five-beam Lidar measuring in cross configuration, illustrated by the right geometry in Figure 2.1, has an extra beam in the horizontal plane, which measures in the centre of the rotor axis. This allows a comparison of three LOS velocities from which the heterogeneity can be determined. However, a non-linearly changing heterogeneity makes this calculation impossible due to the additional unknown corresponding to the second heterogeneity effect. On the other hand, the linear case may be solvable with a two-beam Lidar.[61]

The first method to implement heterogeneity effects in two-beam Lidar measurements was based on the assumption that heterogeneity only affects one beam and that it increases linearly from LOS 0 to LOS 1. This has the following effect on the LOS measurements[61]:

Table 8.1: Adjustment in LOS 1 measurements

LOS0:	HWS0 = HWS	RWS0 = HWS$\cdot \cos(\alpha)$
LOS1:	HWS1 = HWS + X$\cdot$HWS	RWS1 = $(1 + X)\cdot$HWS$\cdot \cos(\alpha)$

It should be noted that YM is assumed to be zero in this case, which is feasible since $cos(\gamma) \approx 1$ (for small γ) results in a negligible effect on the calculated HWS from the RWS measured by the Lidar. However, the linear increase in HWS does not correspond with

having the same HWS at the centre as measured by LOS 0. Therefore, an adjustments to the first method was provided by assuming linear changing heterogeneity on both beams. The first option results in the following LOS measurements:

Table 8.2: Adjustment in LOS measurements using method 1

LOS0:	HWS0 = HWS - X·HWS	RWS0 = (1 - X)·HWS·$\cos(\alpha)$
LOS1:	HWS1 = HWS + X·HWS	RWS1 = (1 + X)·HWS·$\cos(\alpha)$

It can be seen that the heterogeneity effect in the linear case results in the same effect added to one of the beams as subtracted from the other beam. In addition, a second correction was presented which assumes a non-linear heterogeneity between the two Lidar beams. In this case, the two beams will be affected randomly resulting in a different heterogeneity (X_0 and X_1) between -1 and 1. The RWS equations change as follows:

Table 8.3: Correction in LOS measurements using method 2

LOS0:	HWS0 = HWS + X_0·HWS	RWS0 = (1 + X_0)·HWS·$\cos(\alpha)$
LOS1:	HWS1 = HWS + X_1·HWS	RWS1 = (1 + X_1)·HWS·$\cos(\alpha)$

It should be checked whether the linear or non-linear adjustment in a homogeneous wind field represents the flow better in reality. Both options are demonstrated in Figure 8.1, where the left one corresponds with the linear adjustment. The last option is expected to quantify the effect of heterogeneity most accurately, because the turbulent behaviour of wind, which results in different wind speeds along a line for example, is taken into account. By comparing the different methods, the feasibility of each option can be examined.

Heterogeneity has not yet been investigated extensively, because it is a complex subject in wind research. Therefore, it is worth to investigate the effects of it in wind energy applications. In this thesis, the focus will lie on the effect of heterogeneity on 10-minute average Lidar measurements. It can be expected that different analysis tools lead to different results, thus a Matlab simulation will be performed as well as an experiment at Nørrekær Enge. Via the simulation an indication can be found of the effect of heterogeneity, which can then be validated by the real measurements.

8.1.1 Synthetic wind field

The simulations will be performed using synthetic turbulent wind fields, which will be generated with Bladed. These wind fields contain homogeneous wind conditions so that the wind speed, TI, and direction do not change on average over a certain period of time independent of location. The wind velocities are simulated in planes perpendicular to the wind speed as shown in Figure 8.2. The blue coordinate system displays the positive orientation of the coordinate system including the starting point of each axis. Thus, the wind speed measurements will be gained by propagating through the synthetic wind field with the average wind speed. The benefits of this analysis tool are that the wind conditions are known in all cases while the parameters within the field can be influenced.
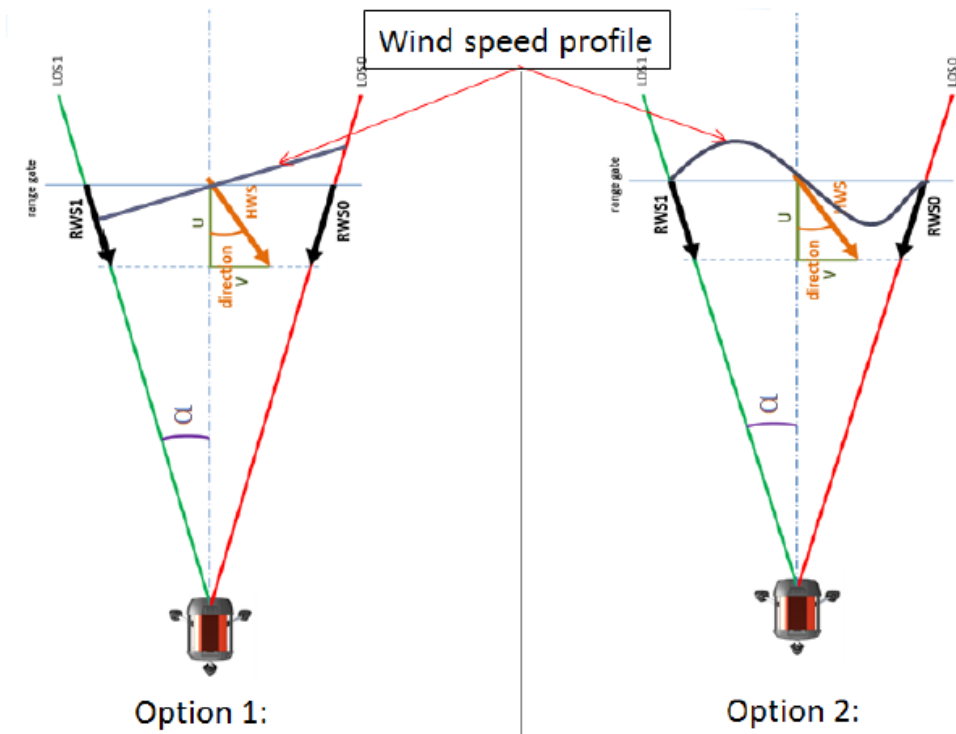
Figure 8.1: Adjustments for the wind speed profile measured with Lidar[61]
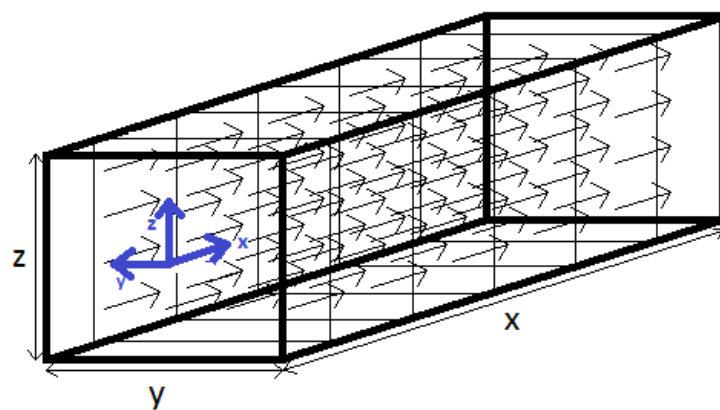
Figure 8.2: Example of a synthetic wind field

A wind field created with Bladed is stored as a *.wnd* file. This file cannot be read directly by Matlab and has to be converted using a Matlab tool from W. Bierbooms. The outcome is a standard normalised distribution based on a zero mean wind speed and a standard deviation of 1. The normalised values, which are in Bladed format, require a conversion to obtain units of meters per second (Equation 8.1). The TI values can be gained from the conversion tool.

$$U_{grid}(y,z,t) = u_{hub} \left(\frac{TI(u)}{1000} U_{grid,norm}(y,z,t) + 1 \right) \tag{8.1a}$$

$$V_{grid}(y,z,t) = u_{hub} \left(\frac{TI(v)}{1000} V_{grid,norm}(y,z,t) \right) \tag{8.1b}$$

$$W_{grid}(y,z,t) = u_{hub} \left(\frac{TI(w)}{1000} W_{grid,norm}(y,z,t) \right) \tag{8.1c}$$

8.2   Simulation

The effect of heterogeneity on Lidar measurements will first be investigated by means of a simulation in which measurements from a virtual two-beam Lidar are compared to the wind conditions at the centre line between the two measurement points of the Lidar. For this simulation, a synthetic wind field is generated using Bladed that contains 4096 (in x-direction) times 21 (in y-direction) times 14 (in z-direction) data points. A frequency of 4 Hz was applied to ensure a feasible grid accuracy as discussed in Appendix G. The total time was set equal to 1024 s, which results in 4096 data points in x-direction at each (y, z)-location. The input parameters for Bladed are given in Table 8.4.

Table 8.4: Bladed input parameters for synthetic wind field

Parameter	Value
Width	200 m
Height	130 m
Number of points in y-direction	21
Number of points in z-direction	14
Duration	1024 s
Frequency	4 Hz
Mean wind speed	12 m/s
Turbulence spectrum	von Karman
Roughness length	0.02 m
TI_u	0.120
TI_v	0.094
TI_w	0.067
Seed	1

In this wind field, the y-values range from -100 to 100 m in steps of 10 m and the z-values from -65 to 65 m in steps of 10 m. Each time step, the x-value, at which the yz-plane is assumed to contain the wind speeds (u, v and w), increases 12 m on average due to the
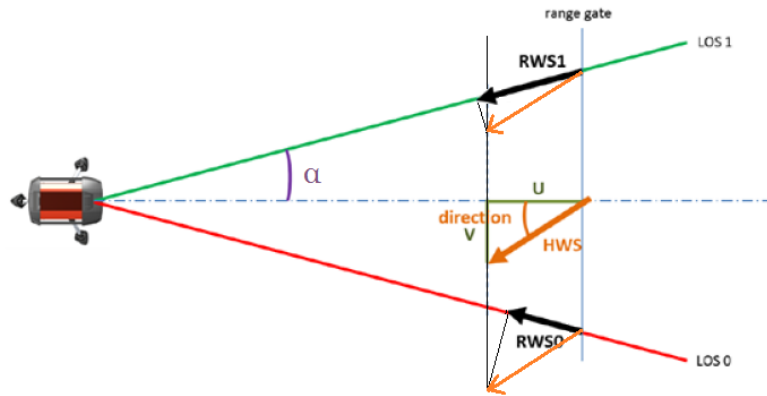
Figure 8.3: Lidar beams and HWS in front of the Lidar

average wind speed of 12 m/s in the x-direction. Thus, measurements will be taken at x-values ranging from 0 to 98292 m in steps of 12 m. The locations of the two virtual Lidar beams in the yz-plane can be determined from a regular two-beam Lidar opening angle of 15° and a measurement distance of 2.5 rotor diameters. In the case of Nørrekær Enge, which will be used as reference, the rotor diameter is equal to 78 m. The measurement points are then located at 60 m from the centre line ($y=0$ m), which represent the Lidar measurement points best in the simulated wind field. The height of the Lidar (beams) is set equal the hub height of 80 m from the wind turbines at Nørrekær Enge. The first z-value of -65 m is considered as ground level, thus the height in the wind field of the Lidar is at $z=15$ m.

Then, wind speeds can be extracted from these positions in the wind field in order to obtain the LOS measurements using Equation 8.2. Hereafter, the wind speeds in x-direction, y-direction and HWS as well as the wind direction can be calculated with Equation 2.4 and Equation 2.5.

$$RWS0 = u\cos\alpha + v\sin\alpha \tag{8.2a}$$
$$RWS1 = u\cos\alpha - v\sin\alpha \tag{8.2b}$$

A wind field generated by Bladed is homogeneous, but can be changed to a heterogeneous wind field easily. For example, a small increase in wind speed can be implemented in the left half of the wind field such that not each part of the wind field is the same. Thus, the difference in Lidar measurements can be simulated by comparing a homogeneous simulation with a heterogeneous one. By performing simulations with different wind field adjustments, the effect of different heterogeneity values on Lidar measurements can be evaluated. Two different types of adjustments to the wind speed in x-direction will be analysed as described in section 8.4. These adjustments also vary in magnitude to check which adjustment approaches reality best. These wind fields are used as input to check if Lidar is able to quantify heterogeneity and to correct for it.

It is assumed that the wind conditions along the centre line represent the real conditions experienced by the rotor of a wind turbine. In case of a homogeneous wind field, the whole

wind field experiences the conditions from this reference location on average. Thus, the wind speeds from this location will be compared to the Lidar measurements. When the differences between the measurements and wind conditions at the reference location are known, it is time to investigate the effect of heterogeneous wind conditions on Lidar measurements and the feasibility to correct for heterogeneity. This will be done by using two different codes, each using one of the correction methods discussed in section 8.1. Both methods will be examined on how accurate they approximate the wind conditions at the reference location.

The first method is based on the assumption of experiencing the same heterogeneity effect on both RWS measurements, but with an opposite sign, compared to the reference location (Table 8.2). In this case, one value will be found for the heterogeneity effect on the Lidar beams. The second method enables to determine a heterogeneity effect on both beams individually as expressed in Table 8.3.

To quantify heterogeneity, the measured RWS by each Lidar beam in the heterogeneous wind fields will be changed with different heterogeneity values. In case of method 1, the RWS will be adjusted with X values ranging from -1 to 1 in steps of 0.01. This will result in 201 options and an accuracy of 1% in the measured HWS. This will also be done for method 2, but then for each possible combination of X_0 and X_1 resulting in 201 times 201 options. Next, the difference in the 10-minute averages of the HWS and wind direction between the simulations and the reference location in the wind field will be determined. Using initial limits for the differences of 0.1 m/s in wind speed and 0.5° in direction, the combinations that satisfy the set limits will be obtained. When there is no value for heterogeneity found that satisfies both limits, the limits will be increased with their initial value. From the results of both methods, the lowest heterogeneity value found for X in case of option 1 and $X_0 + X_1$ in case of option 2, will be determined. Finally, the limits with which the values were found will be compared to each other to conclude which method is the most accurate in quantifying heterogeneity.

In this way, the heterogeneity in the wind field can be quantified. Also, the accuracy of the correction method can be investigated by checking the limits. Consequently, the ability of Lidar to correct for heterogeneity effects in 10-minute average measurements can be analysed. Before the analyses are performed, the code will be validated in the next section. The next step consists of adjusting the wind field to obtain a heterogeneous wind field. Then, the previously described procedure for correcting the measurements can be performed on the adjusted wind field.

8.3 Code validation

The first simulation was performed under homogeneous wind conditions to validate the method and code. In a homogeneous wind field, the mean of the wind speed in x-direction measured at the locations of the Lidar beams should be equal to the mean wind speed listed in Table 8.4. Similarly, the average wind speed in y-direction should approach zero. As a result, the average RWS should be equal to $HWS_{avg} \cdot \cos(\alpha) = U \cdot \cos(\alpha)$ (Equation 2.2). Moreover, the average wind speeds along each y- and z-position in the x-direction in the wind field should be equal to each other, since each part of a homogeneous

(a) LOS measurements from both Lidar beams **(b)** Wind speed in x- and y-direction (u and v)
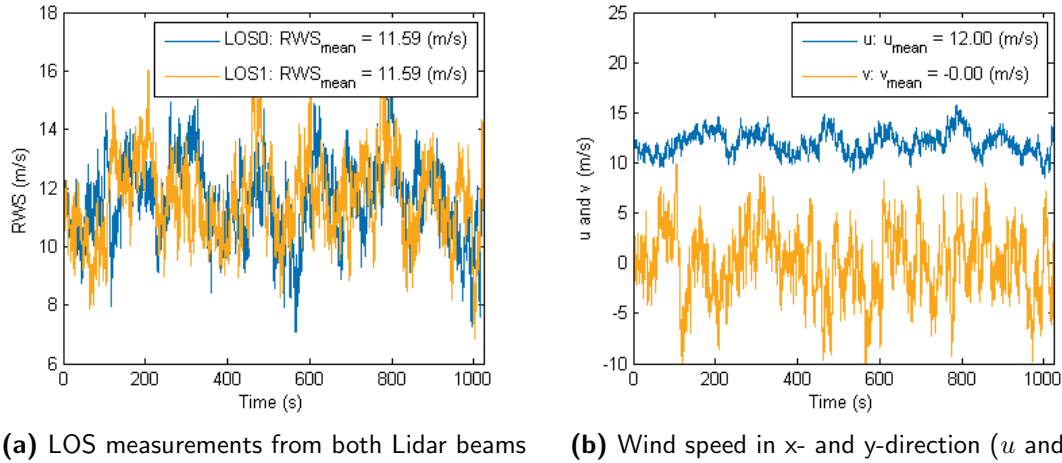
Figure 8.4: Validation of LOS measurements

wind field has the same average wind conditions as another part. This was checked for the two measurement points of the Lidar, which are the most relevant positions.

The LOS measurements including their average from the complete period of 1024 s are shown in Figure 8.4a. It can be seen that the average RWS measured by the Lidar beams are equal to the expected average of 11.59 m/s for $U = 12$ m/s and $\alpha = 15°$. Also, the wind speeds in x- and y-direction were calculated using Equation 2.4 and are plotted in Figure 8.4b. The calculations agree with the characteristics of a homogeneous wind field in which the average wind speed in x-direction is 12 m/s and in y-direction 0 m/s.

The previous was also done for the HWS and direction measurements. First, the RWS measurements of the Lidar are averaged, and then the wind speeds in x- and y-direction are calculated. By averaging over the measurement period, deviations in positive and negative wind speeds cancel each other out. On the other hand, the direction calculation does take the sign of the wind speed in y-direction into account since a negative value leads to a negative wind direction and vice-versa. The calculations showed indeed that averaging led to a significant better result for the HWS, 12 m/s instead of 12.75 m/s as found for the average HWS when first calculating the HWS for each RWS measurement. The wind direction was less affected by the averaging, 0° instead of 0.0085°.

In addition, the effect of the Lidar's sample frequency on the wind speed, direction and TI measurements is analysed. During the measurement period of 1024 s the wind speeds change due to turbulence, but they are constant on average. As can be stated, a 1 Hz sampling frequency of the Lidar gives sufficient data from which the averages are calculated. It is expected that with a lower sampling frequency the results become worse. The effects of different sampling frequencies on the wind speed measurements in x- and y-direction are shown in Table 8.5. It can be seen that the sampling frequency does not affect the HWS and direction measurements in a homogeneous wind field significantly. As the Lidar's sample frequency is currently set to 1 Hz, it is possible to validate the simulations at 1 Hz with the Lidar measurements.

Furthermore, the TI measurements were validated before starting the simulations with a heterogeneous wind field. To do so, the standard deviation was calculated and divided

Table 8.5: Average wind speed calculations as function of Lidar sampling frequency

Sampling freq. [Hz]	Δu [m/s]	$\frac{\Delta u}{U}$ [%]	Δv [m/s]	Wind direction [°]	TI [-]
4	0	0	0	0	0.0953
2	0	0	0.01	0.1	0.0954
1	0.01	0	-0.01	0	0.0951
0.5	-0.01	0	-0.03	-0.2	0.0947
0.25	0.01	0	0.06	0.3	0.0933
0.125	-0.05	0	0.22	1.1	0.0942
0.0625	0.07	0.01	0.33	1.6	0.0933
0.03123	0.13	0.01	-0.25	-1.2	0.0846

by the mean wind speed over the complete simulation period of 1024 s. This was done for both the reference location and Lidar beams. At the reference location, the same average TI values in x- and y-direction were found as the input values. But, the TI calculated using the 4 Hz Lidar measurements was 21% lower than the input value of the TI in x-direction as given in Table 8.5. This lower TI is caused by the averaging of the RWS measurements to obtain the wind speed in x- and y-direction as given in Equation 2.4, because on average it results in wind speeds closer to the mean wind speed and consequently a lower standard deviation. The underestimation can be taken into account by increasing the TI measurements with a factor of 1.26.

Similarly, the difference in RWS between both beams is higher. Looking at the equation for the wind speed in y-direction from the RWS measurements, the magnitude of the wind speed in y-direction will be higher compared to the reference location. Thus, a smaller standard deviation is measured in the x-direction whereas the standard deviation in the y-direction is larger. At a constant mean wind speed in the x-direction, the TI in x-direction becomes lower and in y-direction higher. Another cause of the difference could be the orientation of the two Lidar beams. As a result of the opening angle, the beams are measuring in the xy-plane, which means that the standard deviation results from the standard deviations both in x- and y-direction. Therefore, as the standard deviation in y-direction is lower due to a lower TI_y input than the one in x-direction, a lower TI will be measured in x-direction on average than expected.

8.4   Wind field heterogeneity adjustments

After the code was validated, the wind field was adjusted in order to obtain a heterogeneous wind field. The first adjustment consisted of a linear change in the wind speed in x-direction, u, along the y-direction as illustrated in Figure 8.1 (Option 1) and expressed by Equation 8.3. The maximum difference between the centre line wind speed and the wind speeds at the edges of the wind field is equal to du and y ranges from -100 to 100 m. In the centre of the wind field, where $y = 0$ m, the wind speed as well as the wind direction remain the same.

$$du(y) = \frac{y}{100}du \qquad (8.3)$$
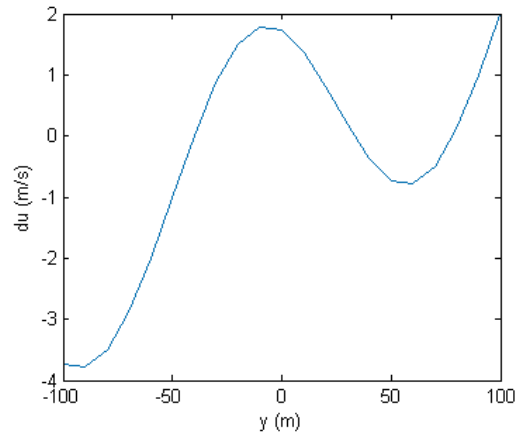
Figure 8.5: Second wind field adjustment in x-direction, u

It could be that a linear adjustment does not represent reality well, so a sinusoidal adjustment was added to the linear one. When implementing a sine only as shown in Figure 8.1 (Option 2), the measurements are similar to the linear case, since the wind speed at the centre line does not change and the Lidar measurement points experience an opposite change in u of the same magnitude. Similarly, a sine, with a wavelength equal to the wind field width of 200 m, added to the linear adjustment would also only increase the magnitude. Therefore, a sine shifted one quarter of the wind field width to the left with a period of 150 m is used on top of the linear adjustment. The resulting change in wind speed is shown in Figure 8.5 and expressed in Equation 8.4. In this case, also the wind speed along the centre line will be changed. In reality, this wind profile can occur when the wind is coming through hills for example, but also in a wind farm between two turbines.

$$du(y) = \frac{y}{100}du + \sin\left(\frac{\pi}{75} \cdot (y + 50)\right)du \tag{8.4}$$

Adjustments will take place for different values of du, since the best representation of reality is not known. These values are equal to: 0.05, 0.10, 0.25, 0.50, 1.00 and 2.00 m/s. This means that the maximum adjustments, which take place at the edges of the wind field, are equal to these values in the linear case. In case of the sinusoidal adjustment, they represent the amplitude and maximum linear change. Later, when comparing the simulations to the five-beam Lidar measurements, it could be possible to determine which adjustment approaches reality best. However, the opposite could be revealed if no good estimation can me made by the simulations.

8.5 Two-beam Lidar simulation

In this section, the results using a two-beam Lidar in a simulated heterogeneous wind field are presented and discussed. The measurement frequency of the simulated Lidar is set to 1 Hz.

(a) HWS   **(b)** Wind direction
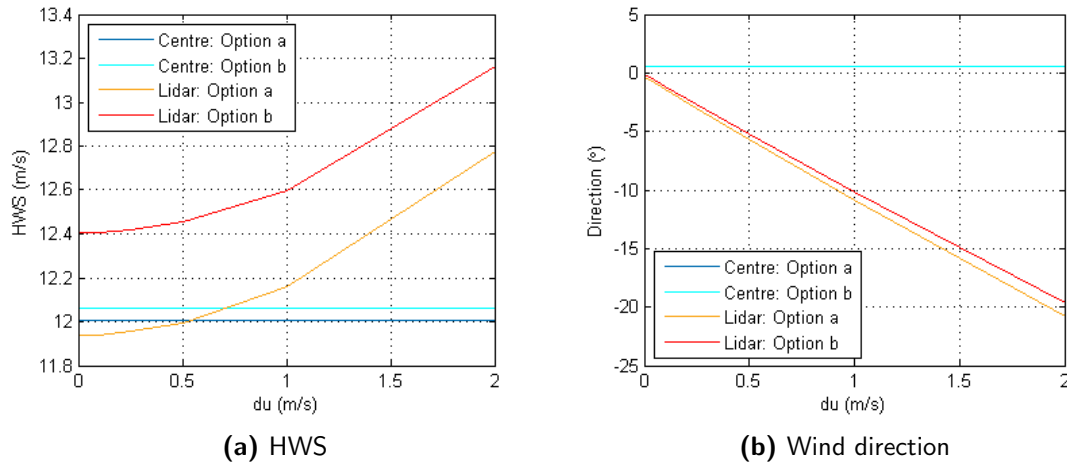
Figure 8.6: Comparison of Lidar measurements against reference location

8.5.1   Linear adjustment

The linear adjustment leads to an increase in the wind speed in x-direction in the left half of the wind field, where the y-coordinates are positive (see Figure 8.2), and a decrease in the other half. At the locations of the Lidar beams, the increase and decrease are equal to $0.6 * du$, where du represents the maximum change in wind speed, due to the measurement locations of the two-beam Lidar in the wind field. This leads to higher HWS and smaller wind directions in the left half of the wind field, as the wind speeds in y-direction remain the same. The wind speed at the reference location remains the same since the change is zero at the centre line. The effect on the Lidar measurements will be discussed below.

The difference between the Lidar measurements and the reference location are first discussed. Two different options for obtaining the 10-minute averages can be examined for a two-beam Lidar:

a) Taking the averages for both RWS measured during a 10-minute measurement period. The HWS and wind direction are then calculated with the RWS averages.

b) Calculate for each RWS measurement the HWS and wind direction. The HWS and wind direction of the 10-minute averages are calculated by averaging the HWS and wind direction measurements within those 10-minute periods.

A Lidar uses the first option to calculate the 10-minute averages[4], but it may be interesting to use the second method if it is possible to correct each RWS measurement. The effects of each linear adjustment on the HWS, wind direction and TI are shown in Figure 8.6. The HWS and wind direction measurements are compared to the reference location for the two mentioned averaging options.

As expected, the deviations increase with increasing adjustments while the HWS and direction at the reference location remain the same. Looking at the HWS measurements, option a) shows the smallest differences. On the other hand, a change of 0.5 m/s in the wind speed leads to a 5° offset in the wind direction for both options, which is close to the

Table 8.6: Linear and non-linear correction values for the linear adjustments in the wind field

du [m/s]	X [-]	X_0 [-]	X_1 [-]
0	0.01	0.01	-0.01
0.05	0.01	0.01	-0.01
0.10	0.01	0.01	-0.01
0.25	0.02	0.02	-0.02
0.50	0.03	0.03	-0.03
1	0.05	0.06	-0.05
2	0.10	0.12	-0.10

uncertainty of 4° found by Goossens. This specific offset in wind direction measurements is mentioned here, because the Lidar manufacturer (Avent Lidar Technologies) suggested that wind flow heterogeneity could cause this uncertainty in case of a two-beam Lidar as discussed by Wessels.

Since the current application of Lidar is mainly wind turbine monitoring instead of active control for example, which requires high frequency measurements to be able to align the turbine optimally, option b) will not be further investigated in this thesis. However, it could be interesting to analyse this option when the possibility to apply Lidar for wind turbine control will be investigated.

Now the differences are known, the possibility to implement heterogeneity effects on the RWS to improve the Lidar measurements will be investigated. As given in Table 8.2, the first correction method assumes the same effect on both RWS measured by the Lidar, but with an opposite sign. The second one enables a different correction in both beams as given in Table 8.3. The corrections will be applied on the 1 Hz RWS measurements of the Lidar.

In case the HWS and direction averages of the measurement period between the Lidar and reference location are compared to each other, the applied correction stays constant over time. The optimal correction X or $X_0 + X_1$ can be defined as well as the corresponding accuracy by analysing the results of the different corrections on the RWS from -1 to 1 in steps of 0.01. The results of both correction methods for one measurement period of 600 s are shown in Figure 8.7 and the optimal corrections to incorporate the heterogeneity effects into the measurements are given in Table 8.6 for the linear, X, and the non-linear correction method, X_0 and X_1. The differences in the HWS and wind direction between the reference locations and the Lidar measurements indicate to what extent the Lidar measurements can be improved with the corrections.

An adjustment less than 0.5 m/s does not lead to significant differences in the HWS measurements between the Lidar and the reference location while the offset in wind direction increases continuously. A correction does immediately improve the wind direction measurements while the positive effect in the HWS begins at 1 m/s. The results from both correction methods show similar results in the wind speed and direction up to 0.5 m/s. At higher adjustments in the wind field, i.e. more heterogeneous wind conditions, the non-linear correction is recommended. The TI did however could not be improved with the correction methods.

The trend in the correction values is similar, which can be explained by the fact that correcting measurements with X means a correction of $X \cdot RWS$ in LOS 0 and the opposite correction in LOS 1. This corresponds to the second method having a positive value for X_0 and the opposite value for X_1. This pattern can be clearly seen in Table 8.6, which was also expected, because the wind field had a linear adjustment.

Looking at the TI measurements, which are multiplied with the correction factor as determined during the code validation, they compare well to the reference location. In fact, corrections will not have much influence on the measurements, because the only change in the TI calculations is the mean wind speed which adjustment is very limited.

Small differences in magnitude can be seen between the two correction values of the second option as a result of the sampling frequency and measurements are taken for a period of 600 s instead of the wind field simulation time of 1024 s. Therefore, the assumption that adjustments of $du \leq 0.10$ m/s did not require corrections when the initial limit of the difference between the HWS values is set to 0.1 m/s, as described in section 8.2, does not hold.

It is also interesting to analyse the measurements when applying the same correction factor for any adjustment. In this case, the magnitude of the heterogeneity in the wind field is not taken into account. An example of the results is shown in Figure 8.8, where the optimal correction factors for the adjustment of 0.5 m/s are used as input. By comparing the results to Figure 8.7, where all adjustments are corrected optimally, it can be seen that the HWS and TI improve slightly. However, the wind directions show larger differences up to 5° for both correction methods.

To conclude, a non-linear correction shows only better results in case of large adjustments in the wind field. The question is which adjustment in the wind field does represent reality best. In addition, a constant correction factor will not be sufficient for any adjustment in the wind field. Therefore, both correction methods could still be helpful to correct Lidar measurements for heterogeneity.

8.5.2 Sinusoidal adjustment

In this section, a sinusoidal adjustment will be analysed to investigate the heterogeneity effect on Lidar measurements in more detail. In this case, the wind speed at the reference location will increase compared to the wind speed in the original wind field as seen from Figure 8.5. At the measurement locations of the Lidar, a negative adjustment will be experienced. First, the effects of the sinusoidal adjustments using both averaging methods are shown in Figure 8.9. It can be seen that in case of zero adjustments option a) approaches the HWS best. On the other hand, when increasing the adjustments option b) results in measurements closer to the reference location. As discussed above, option a) will be used since 10-minute averages are considered while averaging option b) could be used to correct individual measurements, for instance 1 Hz.

In Figure 8.10 the results of the HWS, wind direction and TI are presented. Also, in Table 8.7, the values of both correction methods are listed. The inaccuracies in HWS and wind direction increase with increasing adjustments using the linear correction method. A slight improvement in HWS can be observed while the wind direction becomes worse.
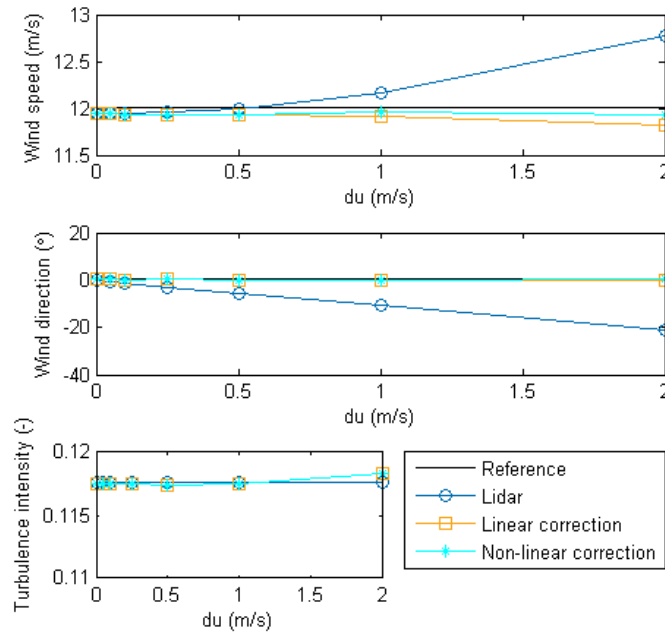
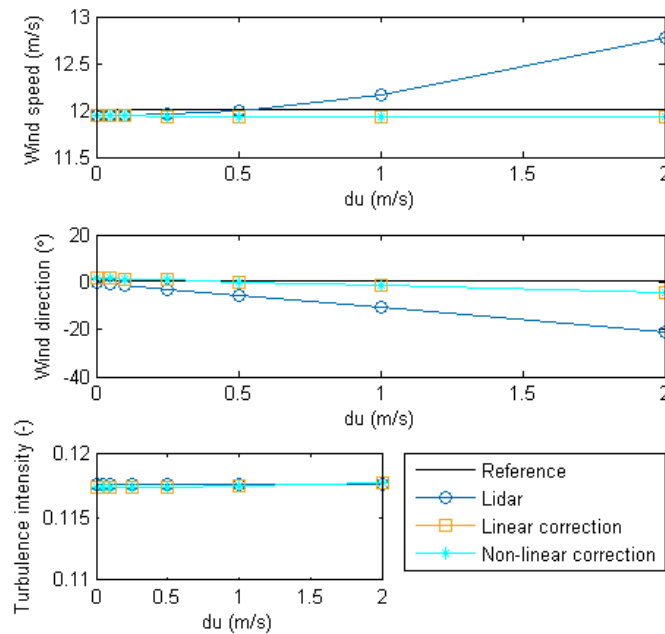**Figure 8.7:** Two-beam Lidar simulations for the linear adjustments including corrections (Table 8.6)

Figure 8.8: Two-beam Lidar simulations for the linear adjustments using pre-defined corrections
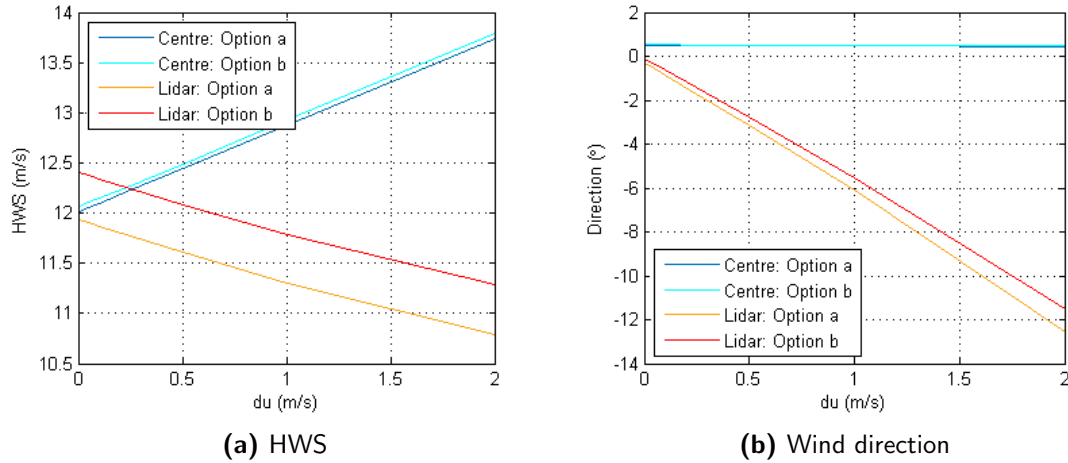
(a) HWS   **(b)** Wind direction

Figure 8.9: Comparison of Lidar measurements against reference location

Table 8.7: Linear and non-linear correction values for the sinusoidal adjustments in the wind field

du [m/s]	X [-]	X_0 [-]	X_1 [-]
0	0.01	0.01	-0.01
0.05	0	0.01	0
0.10	0	0.02	0.01
0.25	0	0.05	0.02
0.50	0	0.09	0.05
1	-0.1	0.18	0.10
2	-0.18	0.38	0.22

Interestingly, a non-linear correction follows the HWS and wind direction as defined at the reference location well. Moreover, the wind direction difference of approximately 4°, which was mentioned by the Lidar manufacturer, at a 0.5 m/s adjustment is reduced to almost zero. However, it is still uncertain which adjustment in the wind field relates to reality. Thus, a validation will be performed to examine the different approaches.

Additionally, the TI measurements are compared to the reference location. As can be seen, the corrections do not result in significant changes in the TI measurements. Again, this can be explained by the limited changes in the TI parameters, the mean and standard deviation of the wind speed in x-direction.

Next, the ability of Lidar to determine the corrections will be investigated. It is clear that Lidar measurements can be improved by correcting them for heterogeneity, but this is only possible with more measurements. Therefore, the next step is to simulate measurements from a five-beam Lidar. This Lidar can measure the wind speed in x-direction at the reference location, i.e. the centre, which can then be used to correct the RWS measurements of the two beams at both sides using the right configuration from Figure 2.1. Then, it is possible to see the improvement using a third beam at hub height in the centre. Also, the ability to correct for heterogeneity can be investigated.
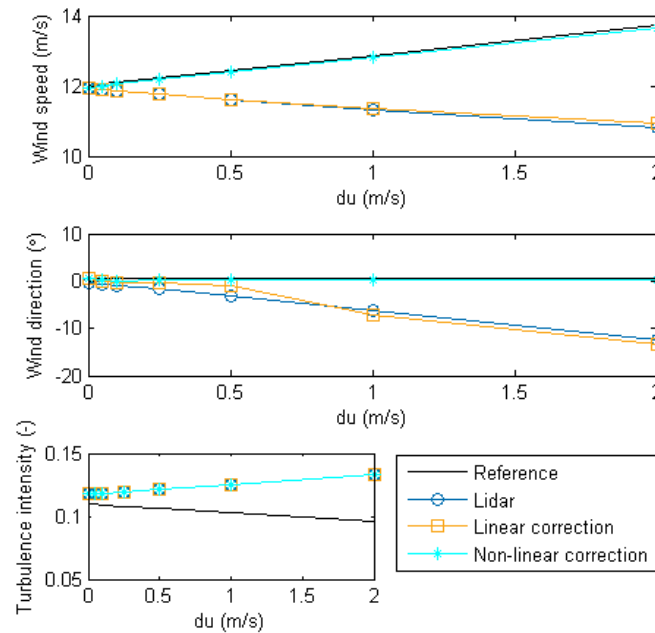
Figure 8.10: Two-beam Lidar simulations for the sinusoidal adjustments including corrections (Table 8.7)

8.5.3 Alternative simulations

The previous results are obtained from simulations with a constant TI and 1 Hz sample frequency. In reality, different TI will occur affecting the Lidar measurements, which will be examined with simulations by changing the TI. In addition, it is interesting to see if a higher sample frequency would improve the Lidar measurement accuracy and corrections. The results of simulations with a different TI and a 2 Hz sample frequency are given in Appendix H.

It was found that for 10-minute average measurements an increase of the sample frequency to 2 Hz would not lead to better measurements. Also, the effect of a different TI did not result in significant differences compared to the simulations with the original TI. So, changing the sample frequency or TI shows only limited effects on the HWS and wind direction measurements.

8.6 Five-beam Lidar simulation

As discussed above, heterogeneity could not be quantified using a two-beam Lidar, but after comparing its measurements to the reference location, the heterogeneity effect could be determined. Interestingly, a five-beam Lidar has a beam in the centre from which the wind speed parallel to the Lidar axis can be obtained, which is visualised in Figure 8.11. So, the wind speed component in the x-direction at the reference location is known. It is
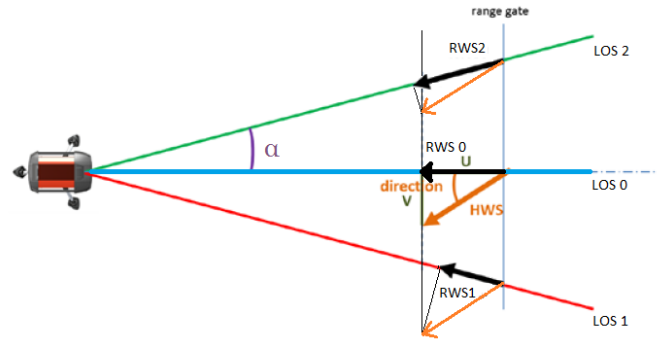
Figure 8.11: Five-beam Lidar measurements and HWS in front of the Lidar

therefore interesting to investigate to what extent a five-beam Lidar is able to quantify heterogeneity and correct for it. This will be done by performing the same analysis as described above.

In the following simulations, the wind speed in x-direction is assumed to be equal to the RWS measured by the centre beam, LOS 0. Next, the RWS measurements by LOS 1 and LOS 2 are used to determine the wind speed in y-direction assuming that the wind speed in x-direction is the same as measured in the centre. Then it is possible to determine the HWS and wind direction from combining LOS 0 with LOS 1 and also with LOS 2. The averages of the calculated wind conditions, HWS and wind direction, are considered as the real wind conditions. It should be noted that the direction should be taken into account when averaging the HWS, because the wind speeds in y-direction can be of opposite sign. Applying the method of a linear correction in the HWS, the correction for the heterogeneity effect can be calculated by rewriting the equations from Table 8.2:

$$X_{lin} = \frac{RWS_2 - RWS_1}{2 \cdot HWS \cdot \cos(\alpha)} \tag{8.5}$$

It is not possible to apply a non-linear correction, because in this case more measurements are required. However, if heterogeneity behaves linear on approximation the linear correction method could be sufficient to correct the five-beam Lidar measurements[61]. Now, the linear correction will be applied on the RWS measurements using the expressions from Table 8.2. Finally, the HWS and wind direction shall be determined from the corrected RWS measurements. By comparing them to the wind conditions at the reference location and the measurements without the correction, the Lidar's accuracy and ability to correct for heterogeneity can be analysed.

The results are plotted in Figure 8.12 and the linear correction values are given in Table 8.8 for the different wind field adjustments. Looking at the results of the linear adjustments, as the heterogeneity in the wind conditions increases the Lidar measurements become worse. As can be seen from the corrected measurements, the Lidar is able to correct for heterogeneity in this case. In accordance with previous results, the TI measurements could not be corrected. It can be concluded that in case of linear heterogeneity in the wind field, the linear correction that can be performed by a five-beam Lidar would lead to better measurements.

(a) Linear adjustment

(b) Sinusoidal adjustment

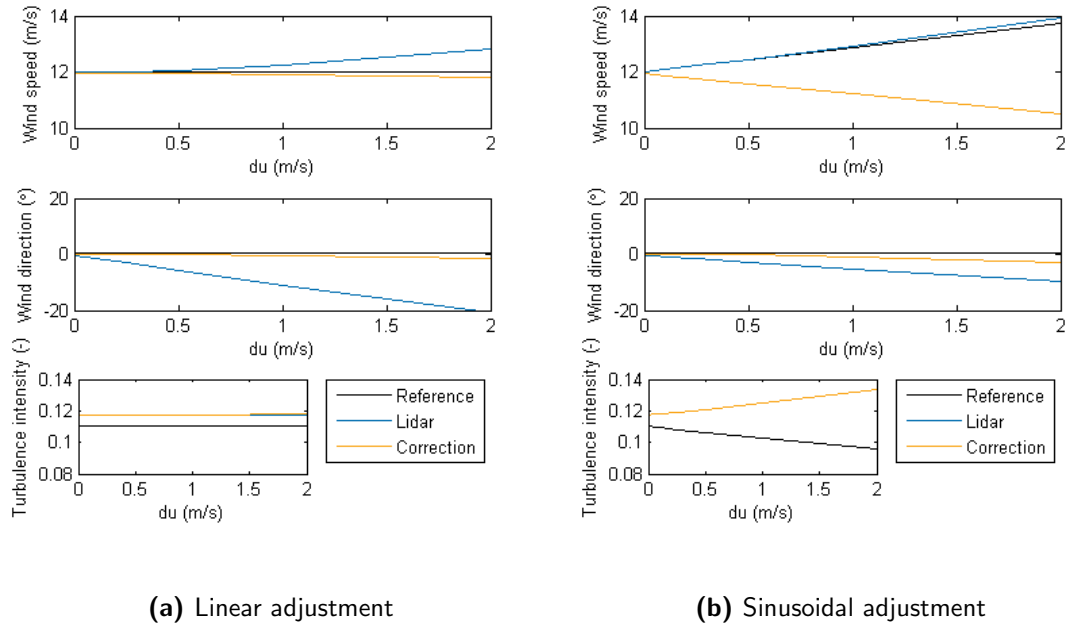**Figure 8.12:** Five-beam Lidar simulations for linear and sinusoidal adjustments including linear correction

Table 8.8: Linear correction values for linear and sinusoidal adjustments in the wind field

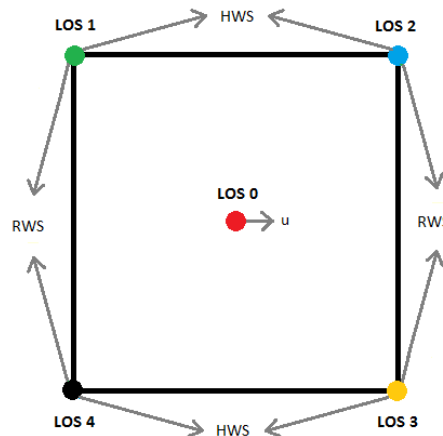| du [m/s]	$\mathbf{X}_{lin}$ [-]	$\mathbf{X}_{sin}$ [-]
0	0.00	0.00
0.05	0.00	0.00
0.10	0.01	0.00
0.25	0.01	0.01
0.50	0.03	0.01
1	0.05	0.03
2	0.09	0.05

Figure 8.13: HWS measurements using five-beam Lidar

On the other hand, it can be seen that the corrected HWS measurements for the sinusoidal adjustment are worse than the Lidar measurements. Interestingly, the correction improves the wind direction measurements while the TI is not changed as expected. So, the performance of the correction method is quite sensitive to the kind of heterogeneity that occurs in the wind field.

8.7 Validation

Now the simulations are analysed, a validation will be performed using the measurements of the met-mast and Avent five-beam Lidar at Nørrekær Enge. The met-mast measurements act as reference to which the Lidar measurements can be compared, because the met-mast is the only IEC-compliant measurement device at this site. The wind speed and YM measurements of the Avent Lidar are compared to the met-mast as well to check the differences between the calculations and the Lidar output. The YM measurements of the met-mast are obtained from the difference between the wind direction measured by the met-mast and the turbine nacelle direction. In this validation, TI will not be discussed since the effect of the RWS corrections is negligible as discussed previously.

The Lidar was configured to measure in a square pattern, so only the centre beam measured at hub height. To obtain RWS measurements at the left and right side of the centre beam, the measurements of the two beams on each side, LOS 1 and LOS 4 as well as LOS 2 and LOS 3, are averaged as illustrated by Figure 8.13. These averages are considered as the RWS measurements of the so-called LOS 1 and LOS 2, the right and left Lidar beams, as shown in Figure 8.11. Before the measurements can be analysed, the data should be filtered so that only the Lidar measurements close to the met-mast are taken into account to ensure a reliable comparison. Therefore, the measurement sector was defined to be between 93° and 123°. In addition, a tilt correction, as described in subsection 2.4.11, will be applied to the Avent Lidar measurements to correct the measurements to hub height.

First, the measurements from LOS 1 and LOS 2 are analysed as if the Lidar had only two-beams. Hereafter, the measurements of LOS 0 are included which determine the wind

Table 8.9: Average difference and standard deviation from each HWS comparison between Avent Lidar and met-mast

Measurement type	Difference [m/s]	Standard deviation [m/s]
Direct output	0.54	0.40
Four beams	0.32	0.33
Five beams	0.57	0.44
Corrected	0.29	0.32

speed in x-direction since this beam measured along the Lidar axis at the centre of the rotor. By combining the RWS measurements from LOS 1 and LOS 2, which can then be averaged to determine the wind speed in y-direction, the HWS and YM based on three Lidar beams can be calculated. It would be expected that the results after including the RWS measurements of the centre beam compare better to the met-mast. After the (improved) HWS and YM are defined, it is possible to calculate the required correction in the RWS measurements from LOS 1 and LOS 2 based on the linear correction method using Equation 8.5. As a result, an indication can be made of the heterogeneity in the wind field based on the Avent Lidar and met-mast measurements. Again, the HWS and YM will be determined from the corrected RWS measurements of LOS 1 and LOS 2.

The results from each HWS comparison are displayed in scatter plots in Figure 8.14. Here, the virtual two-beam Lidar measurements correspond with the averaged measurements of the four corner beams of the five-beam Lidar. Looking at the linear regressions, the differences between the measurements increase slightly when including the measurements of the third beam in the centre whereas the linear correction improves the comparison as seen from the R^2-value. The HWS measurements from the Lidar's output show a similar slope compared to the HWS measurements when the third beam is also taken into account.

However, the measurements without the centre beam show a better correlation as well as a lower difference. Furthermore, it seems that the inclusion of a third beam or a linear correction does not improve the measurements of the virtual two-beam Lidar. So, a linear correction could be insufficient to correct Lidar measurements based on this analysis. It could also be that in reality the heterogeneity is not significant enough to affect the Lidar measurements since the changes are very small.

In addition, the mean values as well as the standard deviations of the differences are given in Table 8.9. Now, it can be clearly seen that the correction improves the five-beam Lidar measurements. However, similar results are obtained using four beams of the Avent Lidar, so it can be questioned whether the direct output is calculated as good as possible.

Next, the YM measurements are to be analysed and the scatter plots can be seen in Figure 8.15. The YM measurements using four beams and five beams compare well to each other. A small change in the slope can be seen, but this does not affect the comparison significantly since most of the scatter is around zero YM. Interestingly, the corrected Lidar measurements show noticeable changes. The scatter reduces as a result of the correction, but the slope changes negatively. The slope of the linear regression using the averaged RWS measurements from the four corner beams is closest to unity, but it does not show lower scatter than the original Avent Lidar measurements. Thus,
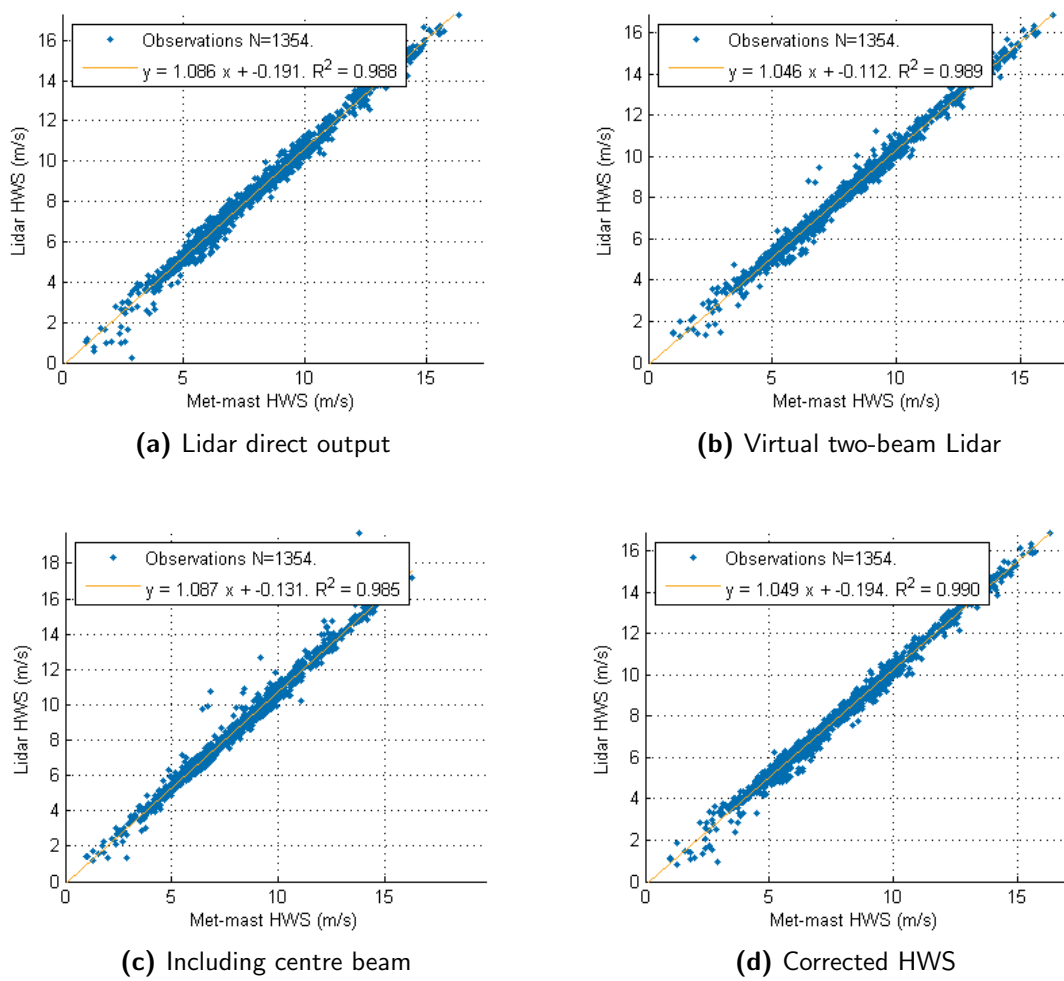
(a) Lidar direct output

(b) Virtual two-beam Lidar

(c) Including centre beam

(d) Corrected HWS

Figure 8.14: Comparison of HWS measurements between Lidar and met-mast

(a) Lidar direct output

(b) Virtual two-beam Lidar

(c) Including centre beam
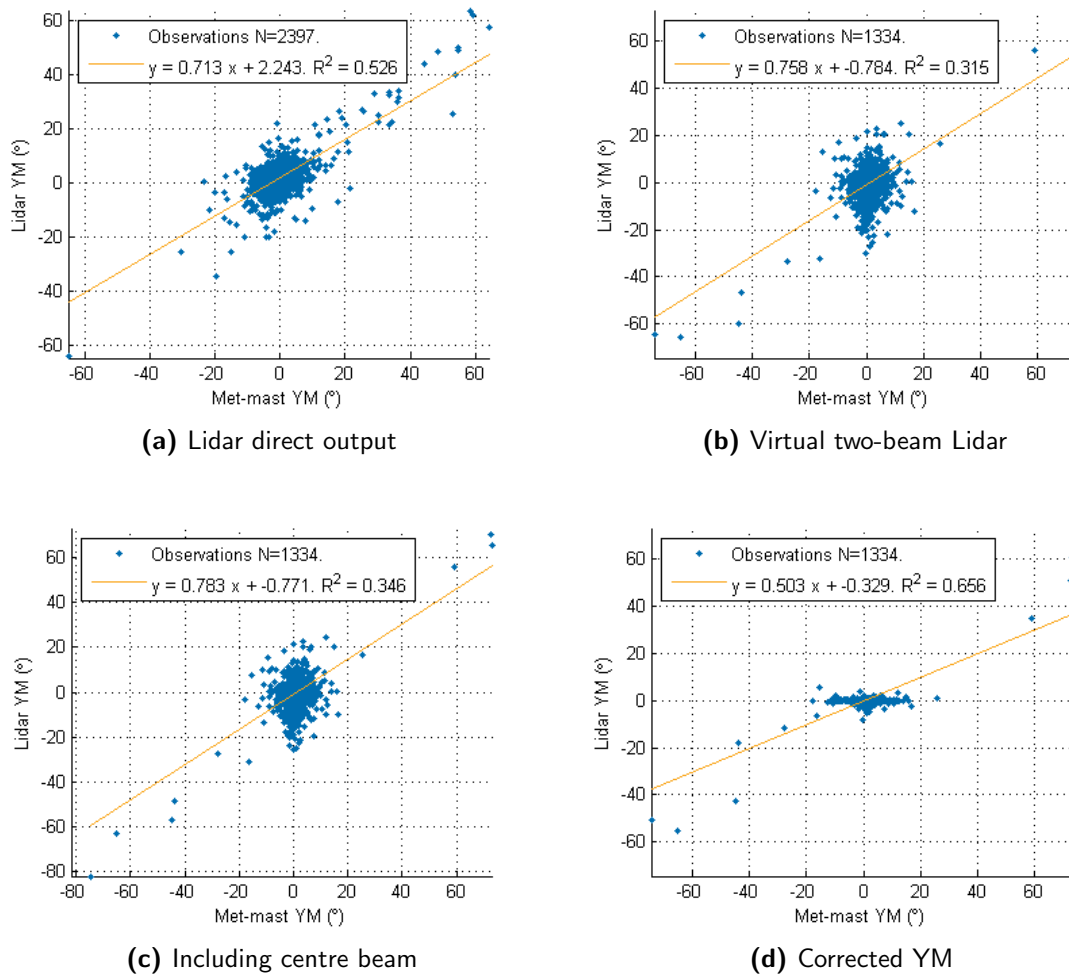
(d) Corrected YM

Figure 8.15: Comparison of YM measurements between Lidar and met-mast

the YM comparisons show no favourable results for the ability of the correction method to improve Lidar measurements.

To have a closer look at the differences between the YM measurements, the average and standard deviations of the differences to the met-mast measurements are given in Table 8.10. This table seems to give similar results as expected from the scatter plots. However, the lower values from the corrected YM measurements are caused by the fact that the RWS measurement of LOS 0 determines the wind speed in x-direction and the resulting wind speeds in y-direction of LOS 1 and LOS 2 are averaged. As a result of this averaging, the YM decreases significantly in the Lidar measurements. At the same time, this leads to a better comparison between the calculations and met-mast measurements because the measurements are located around zero. Thus, the calculations approach the met-mast measurements due to the reduction in YM while the measurements do not improve significantly. Furthermore, it can be seen that the YM uncertainty between the met-mast and Lidar is close to the 4° as found by Goossens.

The next analysis examines the heterogeneity in the wind field by looking into the cor-

Table 8.10: Average difference and standard deviation from each YM comparison between Avent Lidar and met-mast

Measurement type	Difference [°]	Standard deviation [°]
Direct output	3.5	4.6
Four beams	5.1	7.7
Five beams	4.9	7.4
Corrected	2.4	4.7

rection factor implemented into the Lidar measurements. The linear correction was on average -0.0021 and the average of the absolute corrections was 0.0144. An average correction of 1.44% of the RWS measured by the centre beam is approximately 0.10 m/s using the average wind speed measured by the met-mast. This seems to be a low adjustment in the Lidar measurements, but since the power is related to the wind speed cubed the difference becomes ±4% in PCV for example. On the other hand, the average is close to zero so that the adjustments could become negligible when the wind speeds and power outputs are binned due to averaging, since the correction is both negative and positive. The average correction close to zero can also be interpreted as an indication that the heterogeneity in the wind field is negligible so that a correction is unnecessary.

From the previous results cannot be concluded that implementing the effects of heterogeneity using a linear correction improves Lidar measurements. The heterogeneity effect may be negligible, but the correction method can also be insufficient. Another analysis will be performed with the assumption of zero YM and the centre beam representing the HWS so that the heterogeneity in the wind field can be quantified by the differences between the RWS measurements. The differences between the RWS measurements could indicate if heterogeneity can be represented by a linear adjustment in the wind field.

As discussed in section 8.5, Lidar measurements can be corrected if the heterogeneity is approximately linear in a wind field. To be able to check the difference between each beam, the assumption is made that the YM is zero. Thus, the YM measurements of the met-mast larger than 5° are excluded, since 5° leads to only a 0.38% change in the HWS ($\cos(5°)$=0.9964 m/s). In case of zero YM, the RWS measured by the centre beam can represent the HWS. Then, the RWS measurements at both sides will be compared to the measurements from the centre beam from which the correction can be calculated with Equation 8.6. In this equation, the measurements of the centre beam are multiplied by $\cos(\alpha)$ to imitate the measurements at both sides measuring under an opening angle α. A comparison between the met-mast measurements and the measurements from the centre beam is shown in Figure 8.16. It can be seen that in case of a very low YM as defined by the met-mast, the measurements of the centre beam correlate well with the met-mast measurements.

$$X = \frac{RWS_0 \cdot \cos(\alpha) - RWS}{RWS} \tag{8.6}$$

Again, the average of the corrections on both sides are defined as well as the average of the absolute values. The first value does not take the sign into account whereas the latter gives more information about the need for a correction, since it could be that the
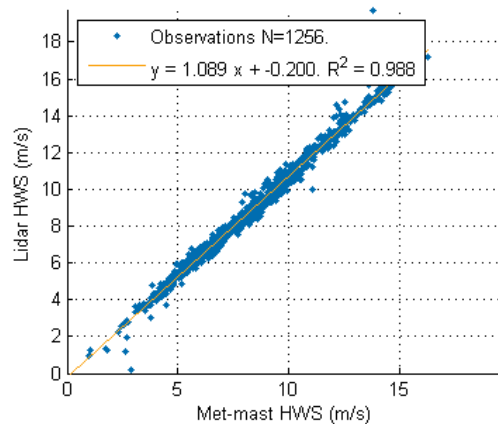
Figure 8.16: Comparison between Avent Lidar and met-mast HWS measurements assuming zero YM and after corrections

average is close to zero while every measurement needed an absolute adjustment of 10% for example, but both negative and positive so that the corrections cancel each other out.

The average corrections in the RWS measurements from LOS 1 and LOS 2 compared to LOS 0 were found to be 0.043 m/s and 0.038 m/s respectively. The absolute corrections were on average equal to 0.050 m/s and 0.047 m/s, which means that at both sides the RWS measurements underestimated the HWS. Moreover, the required change is positive on both sides, which means that the heterogeneity is not linear. So, the required corrections are ±0.5% if a 7 m/s wind speed is considered, which would result in a ±2.1% difference in power output. This uncertainty is significant enough to require a sufficient correction, but due to the non-linear heterogeneity it is difficult to improve the Lidar measurements significantly with a linear correction method.

Chapter 9

Conclusions and Recommendations

In this chapter, the conclusions of this thesis will be presented. Subsequently, the recommendations will be given for future research.

9.1 Conclusions

The first step in this thesis was to gain experience with Lidar data to be able to use its measurements for PCV according to the IEC standard. In addition, it was needed to understand the turbulence normalisation procedure from the IEC properly. These first steps were taken by using the data from the measurement campaign at Prinses Alexia.

The newly developed Avent five-beam Lidar was part of a measurement campaign at Nørrekær Enge. Its availability showed large dependency on each beam. One of the beams was subject to significant errors in the measurements resulting in a 25% availability overall as well as a lower Carrier-to-Noise Ratio compared to the other beams. Therefore, the arbitrary thresholds determined by Borraccino and Courtney and Wessels should be checked before excluding reliable measurements[8][61], but care should be taken when using the Avent Lidar for PCV according to its low availability.

The validation of the wind speed measurements at Nørrekær Enge showed that the Avent Lidar, ZephIR Lidar and ROMO Wind spinner anemometer compare well to met-mast ($R^2 \geq 0.978$). Also, the Lidars seem to measure YM sufficiently accurate when looking at the distributions and standard deviation whereas it was suggested that the spinner anemometer was able to measure YM more accurately than the met-mast and Lidars due to its significant lower standard deviation of $2.20°$ instead of $\pm4°$. However, a conclusion cannot be made according to the discussion on which measurement device measures the 'real' wind conditions.

Considering TI measurements, only the Avent Lidar showed some correlation with the met-mast while the comparison between the spinner anemometer and Avent Lidar showed the best correlation ($R^2=0.786$ against $R^2=0.721$). This could be the result of the fixed

measurement location of the met-mast compared to the Lidars and spinner anemometer which were always measuring wind conditions coming towards the turbine.

Regarding PCV, the Avent Lidar underestimated the power curve slightly as a result of the higher wind speed measurements compared to the met-mast. Consequently, the calculated AEP of the Avent Lidar was up to 3.5% lower while the spinner anemometer showed an approximately 2% better AEP compared to the met-mast. Only the AEP measured with the ZephIR Lidar measurements compared well. In addition, the scatter around the power curve was slightly lower when using the spinner anemometer measurements.

The effect of TI on the power output was also investigated. This was first done by binning power curves to several TI values for a preliminary indication. By comparing the AEP for different TI, the optimal TI was found to be 0.08 at Prinses Alexia and 0.14 up to 0.16 at Nørrekær Enge.

Hereafter, the tubulence normalisation procedure as reported in the IEC standard of 2016 was followed. First, power curve simulations in which only the TI varied were normalised. Both the effects on the power curve and scatter around the power curve were in agreement with literature[27]. Secondly, the turbulence normalisation was applied on the data from Prinses Alexia and Nørrekær Enge. Surprisingly, the effects on the power curves were observed while the scatter did not improve. It can therefore be questioned whether this normalisation can improve power curve uncertainty significantly since the power output also depends on other factors. Please note that the calculations are also affected by the Lidar's uncertainty in measuring TI.

This thesis proved that it is possible to normalise power curves to a certain TI. As the average TI at a site can be defined, the site-specific turbine performance can be determined via the normalisation. Consequently, it could be possible to provide guaranteed power curves for a broader range of TI. This means that the uncertainty in turbine performance due to TI can be reduced.

Furthermore, to the author's knowledge this is the first research that looked deeper into the effect of assuming homogeneous wind conditions between two measurement points of a Lidar. The 4° uncertainty in measuring YM as found by Goossens could be the effect of heterogeneity as suggested by the Lidar manufacturer. Therefore, simulations with various heterogeneous wind fields were performed to investigate the concept of heterogeneity and the effects of it on Lidar measurements. From simulating two-beam Lidar measurements it can be stated that only significant differences in the wind field, i.e. a large heterogeneity, would affect the measurements so that they require a correction to obtain reliable measurements for PCV. For example, a difference of ±4% in the wind field velocities, which was considered as a large heterogeneity, resulted in 4° difference between the Lidar and met-mast YM measurements.

This thesis also focused on the development and implementation of a linear and non-linear correction method for the Lidar measurements. A non-linear correction shows only better results in case of large adjustments in the wind field, i.e. large heterogeneity. However, the question remains which adjustment in the wind field does represent reality best. In addition, a constant correction factor will not be sufficient for any adjustment in the wind field. Therefore, both correction methods could still be helpful to correct Lidar measurements for heterogeneity. The simulations of a five-beam Lidar in case of linear heterogeneity in a wind field showed that a correction improved the measurements.

This could not be obtained when a sinusoidal adjustment was applied to the wind field. Therefore, it can be stated that the ability of a five-beam Lidar to correct its measurements is sensitive to the kind of heterogeneity occurring in the wind field.

Finally, a validation of the heterogeneity was performed by using the measurements of the five-beam Lidar at Nørrekær Enge while the met-mast served as reference measurement device. No conclusive results could be found when applying a linear correction to the HWS and YM measurements from the five beams. It was found that the heterogeneity in reality is significant enough to recommend a correction for reliable PCV, but a suitable correction method could not be developed.

9.2 Recommendations

The data sets of the ground-based Lidar from ZephIR at Prinses Alexia and both nacelle-based Lidars at Nørrekær Enge were not chronically ordered. It could be valuable to investigate the cause of this, since it seems to be straightforward that data is collected and distributed to difference parties in a chronological order.

In addition, the research showed that the nacelle directions were calibrated incorrectly. The problem could be that the calibration is done with a compass inside the nacelle where all the equipment is already installed. As a result, the disturbance in the magnetic field leads to an erroneous calibration. It is therefore recommended to perform a calibration before installing the equipment inside the nacelle.

As the measurement campaigns were performed at two sites mostly surrounded by farmland and water, it could be valuable to analyse the Lidar and spinner anemometer measurements in more complex terrain. In this way, the feasibility of using other devices than met-mast can be evaluated.

As no conclusive results were found on the influence of turbulence normalisation on the scatter around the power curve, it could be valuable to investigate this further by isolating the effects of TI. This means that the effect of turbulence normalisation on the scatter is checked for different TI while the other conditions remain the same. In this way it is possible to determine the effect of TI better than when the other conditions are varying.

In this research it was shown that Lidars and spinner anemometers may not be used for turbulence normalisation, because they could not measure TI as accurate as the met-mast. However, the question can also be which measurement device should be used as reference system. This could be tested by measuring with all measurement devices in a wind field that is completely known.

Another effect on turbine performance that should be further investigated is wind shear. It could be interesting to develop a similar procedure as done for turbulence. This will help to reduce the limited applicability of the guaranteed power curve provided by turbine manufacturers.

The heterogeneity simulations showed no conclusive results regarding the effect of heterogeneity on the Lidar measurements. However, the author believes it is valuable to investigate this concept further. By quantifying heterogeneity with a Lidar continuously

looking to a met-mast, using met-mast measurements as reference, a better comparison can be made between the measurements.

Finally, the simulations can be improved by changing the reference measurements as the wind conditions in one point to a reference area, for example the rotor area of a turbine. A better approximation can then be made of the wind conditions experienced by the turbine rotor. In this way, the effect of having only a limited number of measurement locations instead of a complete rotor representation can also be defined. This can also identify the limitations of point measurements.

References

[1] A. Albers. Critical Limitations of Wind Turbine Power Curve Warranties. Technical report, Deutsche WindGuard Consulting GmbH, 2012. URL http://www.windguard.de/fileadmin/media/pdfs/UEber{_}Uns/Veroeffentlichtungen{_}2012/paper199{_}Power{_}Curve{_}WindGuard.pdf.

[2] Avent Lidar Technology. Wind Iris Brochure, 2013.

[3] Avent Lidar Technology. 5-beam Lidar Software 1.2 User Manual, 2014.

[4] Avent Lidar Technology. Wind Iris Software 1.2 User Manual, 2014. URL http://www.leosphere.com/products/turbine-mounted/wind-iris-nacelle-wind-turbine-lidar.

[5] W.A.A.M. Bierbooms. Matlab function: least-square estimation of Weibull parameters, 1999.

[6] W.A.A.M. Bierbooms. Offshore Wind Climate, 2016.

[7] F. Bingöl, J. Mann, and D. Foussekis. LiDAR error estimation with WAsP engineering. In *14th International Symposium for the Advancement of Boundary Layer Remote Sensing*, volume 1, page 12058, 2008. doi: 10.1088/1755-1315/1/1/012058.

[8] A. Borraccino and M. Courtney. *Calibration report for Avent 5-beam Demonstrator lidar DTU Wind Energy E-Report-0087*. 2016. ISBN 9788793278370.

[9] E. A. Bossanyi, A. Kumar, and O. Hugues-Salas. Wind turbine control applications of turbine-mounted LIDAR. *4th Scientific Conference on Science of Making Torque from Wind*, 012011, 2014. ISSN 1742-6588. doi: 10.1088/1742-6596/555/1/012011. URL http://stacks.iop.org/1742-6596/555/i=1/a=012011?key=crossref.95f22245fc836df7c59a2d7ef15340e0.

[10] A. Cassola, M. Stickland, and A. Oldroyd. Two-beam lidar measurements in a non-homogeneous wind field. *EWEA Offshore 2015, 2015-03-10 - 2015-03-12, Copenhagen*, 2015.

[11] A. Clifton, D. Elliott, and M. Courtney. 15. Ground-Based Vertically- Profiling Remote Sensing for Wind Resource Assessment. 2013. URL www.ieawind.org.

[12] R. T. H. Collis. Lidar Observation of Cloud. *Science*, 149(3687):978–981, 1965.

[13] R. T. H. Collis. Lidar: A new atmospheric probe. *Quarterly Journal of the Royal Meteorological Society*, 92(392):220–230, 1966. ISSN 1477870X. doi: 10.1002/qj. 49709239205.

[14] R. T. H. Collis. Lidar. *APPLIED OPTICS*, 9(8):1782–1788, 1970.

[15] G. Demurtas and N. G. C. Janssen. An innovative method to calibrate a spinner anemometer without use of yaw position sensor. *Wind Energy Science*, 10 (April):1–12, 2016. ISSN 2366-7621. doi: 10.5194/wes-2016-10. URL http://www.wind-energ-sci-discuss.net/wes-2016-10/.

[16] E. W. Eloranta, J. M. King, and J. A. Weinman. The Determination of Wind Speeds in the Boundary Layer by Monostatic Lidar, 1975. ISSN 15200450. URL http://journals.ametsoc.org/doi/abs/10.1175/1520-0450(1975)014{%}3C1485:TDOWSI{%}3E2.0.CO;2.

[17] L. Falbe-Hansen. Technology Review of the ROMO Wind Spinner Anemometer. Technical Report B, Garrad Hassan & Partners Ltd, 2012.

[18] P. A. Fleming, A. K. Scholbrock, A. Jehu, S. Davoust, E. Osler, Alan D. Wright, and A. Clifton. Field-test results using a nacelle-mounted lidar for improving wind turbine power capture by reducing yaw misalignment. In *Nordic Wind Power Conference*, volume 524, page 012002, 2014. doi: 10.1088/1742-6596/524/1/012002. URL http://stacks.iop.org/1742-6596/524/i=1/a=012002?key=crossref.efcc12681c6b46c26d377e1e2f7672c7.

[19] S. Goossens. *Field-test of nacelle-based lidar to explore its applications for Vattenfall as wind park operator*. PhD thesis, Delft University of Technology, 2015.

[20] C. B. Hasager, D. Stein, M. Courtney, A. Peña, T. Mikkelsen, M. Stickland, and A. Oldroyd. Hub height ocean winds over the north sea observed by the NORSEWInD lidar array: Measuring techniques, quality control and data management. *Remote Sensing*, 5(9):4280–4303, 2013. ISSN 20724292. doi: 10.3390/rs5094280.

[21] International Electrotechnical Commission. IEC 61400-12-1. Wind turbines - Part 12-1: Power performance measurements of electricity producing wind turbines. Technical report, IEC, 2005.

[22] International Electrotechnical Commission. IEC 61400-12-1: Wind energy generation systems - Part 12-1: Power performance measurements of electricity producing wind turbines. Technical report, International Electrotechnical Commission, 2016.

[23] G. V. Iungo, Y.-T. Wu, and F. Porté-Agel. Field Measurements of Wind Turbine Wakes with Lidars. *Journal of Atmospheric and Oceanic Technology*, 30(2):274–287, 2013. ISSN 0739-0572. doi: 10.1175/JTECH-D-12-00051.1.

[24] G.V. Iungo and F. Porté-Agel. Volumetric scans of wind turbine wakes performed with three simultaneous wind LiDARs under different atmospheric stability regimes. In *5th Science of Making Torque from Wind Conference*, 2014. ISBN 0739-0572. doi: 10.1088/1742-6596/524/1/012164. URL http://stacks.iop.org/1742-6596/524/i=1/a=012164?key=crossref.192b471f38eba3d41487be5ccbb3212b.

[25] A. Jiménez, A. Crespo, E. Migoya, and J. Garcia. Large-eddy simulation of spectral coherence in a wind turbine wake. *Environmental Research Letters*, 3(1):015004, 2008. ISSN 1748-9326. doi: 10.1088/1748-9326/3/1/015004. URL http://stacks.iop.org/1748-9326/3/i=1/a=015004{%}5Cnhttp://iopscience.iop.org/1748-9326/3/1/015004/fulltext/.

[26] C. G. Justus. *Winds and wind system performance*. Franklin Institute Press, 1978.

[27] K. Kaiser, W. Langreder, H. Hohlen, and J. Højstrup. Turbulence Correction for Power Curves. In *EWEC 2003*, pages 159–162, 2003. ISBN 9783540338659. doi: 10.1007/978-3-540-33866-6_28. URL http://www.ncbi.nlm.nih.gov/pubmed/22096173.

[28] D. Kindler, A. Oldroyd, Al. MacAskill, and D. Finch. An eight month test campaign of the Qinetiq ZephIR system: Preliminary results. *Meteorologische Zeitschrift*, 16(5):479–489, 2007. ISSN 09412948. doi: 10.1127/0941-2948/2007/0226.

[29] K. A. Kragh and M. H. Hansen. Potential of power gain with improved yaw alignment. *Wind Energy*, 18(6):979–989, 2015. ISSN 10991824. doi: 10.1002/we.1739.

[30] T. R. Lawrence, D. J. Wilson, C. E. Craven, I. P. Jones, R. M. Huffaker, and J. A L Thomson. A laser velocimeter for remote wind sensing. *Review of Scientific Instruments*, 43(3):512–518, 1972. ISSN 00346748. doi: 10.1063/1.1685674.

[31] J. K. Lundquist, M. J. Churchfield, S. Lee, and A. Clifton. Quantifying error of lidar and sodar doppler beam swinging measurements of wind turbine wakes using computational fluid dynamics. *Atmospheric Measurement Techniques*, 8(2):907–920, 2015. ISSN 18678548. doi: 10.5194/amt-8-907-2015.

[32] T. Mikkelsen, N. Angelou, K. Hansen, M. Sjöholm, M. Harris, C. Slinger, P. Hadley, R. Scullion, G. Ellis, and G. Vives. A spinner-integrated wind lidar for enhanced windturbine control. *Wind Energy*, 16(4):625–643, 2013.

[33] C. Ng and L. Ran. *Offshore Wind Farms: Technologies, Design and Operation*. Woodhead Publishing, 2016.

[34] K. H. Papadopoulos, N. C. Stefantos, U. S. Paulsen, and E. Morfiadakis. Effects of turbulence and flow inclination on the performance of cup anemometers in the field. *Boundary-Layer Meteorology*, 101(1):77–107, 2001. ISSN 00068314. doi: 10.1023/A:1019254020039.

[35] T. F. Pedersen. Power curves - use of spinner anemometry. In *PWCG, 2014-04-01*. PCWG, 2014.

[36] T. F. Pedersen, G. Demurtas, A. Sommer, and J. Højstrup. Measurement of rotor centre flow direction and turbulence in wind farm environment. In *5th Science of Making Torque from Wind Conference*, volume 524, page 012167, 2014. doi: 10.1088/1742-6596/524/1/012167. URL http://stacks.iop.org/1742-6596/524/i=1/a=012167http://stacks.iop.org/1742-6596/524/i=1/a=012167{%}5Cnhttp://stacks.iop.org/1742-6596/524/i=1/a=012167?key=crossref.47232065d92a392dc38cc31984020104.

[37] T. F. Pedersen, G. Demurtas, and F. Zahle. Calibration of a spinner anemometer for yaw misalignment measurements. *Wind Energy*, 18(11):1933–1952, 2015. ISSN 10991824. doi: 10.1002/we.1798.

[38] T.F. Pedersen, P. Ingham, and H.K. Jørgensen. *Wind Turbine Power Performance Verification in Complex Terrain and Wind Farms*, volume 1330. 2002. ISBN 8755030289. doi: Ris-R-1330(EN).

[39] A. Peña, C. B. Hasager, J. Lange, J. Anger, M. Badger, F. Bingöl, O. Bischoff, J. Cariou, F. Dunne, S. Emeis, M. Harris, M. Hofsäss, I. Karagali, J. Laks, S. Larsen, J. Mann, T. Mikkelsen, L. Y. Pao, M. Pitter, A. Rettenmeier, A. Sathe, F. Scanzani, D. Schlipf, E. Simley, C. Slinger, R. Wagner, and I. Würth. *Remote Sensing for Wind Energy*, volume 0029. DTU Wind Energy, 2013. ISBN 9788792896414.

[40] R. H. Rasshofer, M. Spies, and H. Spies. Influences of weather phenomena on automotive laser radar systems. *Advances in Radio Science*, 9:49–60, 2011. ISSN 16849965. doi: 10.5194/ars-9-49-2011.

[41] A. Sathe, J. Mann, J. Gottschall, and M. S. Courtney. Can wind lidars measure turbulence? *Journal of Atmospheric and Oceanic Technology*, 28(7):853–868, 2011. ISSN 07390572. doi: 10.1175/JTECH-D-10-05004.1.

[42] D. Schlipf, P. W. Cheng, and J. Mann. Model of the correlation between lidar systems and wind turbines for lidar-assisted control. *Journal of Atmospheric and Oceanic Technology*, 30(10):2233–2240, 2013. ISSN 07390572. doi: 10.1175/JTECH-D-13-00077.1.

[43] D. Schlipf, P. Fleming, F. Haizmann, A. Scholbrock, M. Hofsäß, A. Wright, and P. W. Cheng. Field Testing of Feedforward Collective Pitch Control on the CART2 Using a Nacelle-Based Lidar Scanner. In *4th Scientific Conference on Science of Making Torque from Wind*, 2014. doi: 10.1088/1742-6596/555/1/012090. URL http://stacks.iop.org/1742-6596/555/i=1/a=012090.

[44] A. Scholbrock, P. Fleming, A. Wright, C. Slinger, J. Medley, and M. Harris. Field test results from lidar measured yaw control for improved yaw alignment with the NREL Controls Advanced Research Turbine. In *AIAA Science and Technology Forum and Exposition 2015*, number January. National Renewable Energy Laboratory (NREL), 2015. ISBN 9781624103445.

[45] E. Simley, L. Y. Pao, R. Frehlich, B. Jonkman, and N. Kelley. Analysis of light detection and ranging wind speed measurements for wind turbine control. *Wind Energy*, 17(3):413–433, 2014.

[46] C. Slinger. Nørrekær Enge UniTTe campaign a ZephIR lidar perspective. (November), 2016.

[47] B. Smith, H. Link, G. Randall, and T. McCoy. Applicability of Nacelle Anemometer Measurements for Use in Turbine Power Performance Tests. In *American Wind Energy Association (AWEA) WINDPOWER 2002 Conference*, number May, page 19, 2002. URL http://www.osti.gov/bridge.

[48] D. A. Smith, M. Harris, Adrian S. C., T. Mikkelsen, H. E. Jørgensen, J. Mann, and R. Danielian. Wind Lidar Evaluation at the Danish Wind Test Site in Høvsøre. *Wind Energy*, 9(January):87–93, 2006. doi: 10.1002/we.

[49] P. Stuart, N. Atkinson, A. Clerc, A. Ely, M. Smith, J. Cronin, and M. Zhu. Why does T7 underperform? Individual turbine performance relative to preconstruction estimates., 2012.

[50] L. Svenningsen. Proposal of an Improved Power Curve Correction. In *European Wind Energy Conference & Exhibition 2010*, number April, 2010. URL http://proceedings.ewea.org/ewec2010/posters/PO. 310{_}EWEC2010presentation.pdf.

[51] H. C. van der Velde. *Wind turbine power performance testing using a Lidar*. PhD thesis, Utrecht University, 2016.

[52] A. Vignaroli. Measurement campaign in flat terrain , Nørrekær Enge , June- December 2015. (December), 2016.

[53] H. M. Villanueva Lopez. *The Illusion of Power Curves*. PhD thesis, Delft University of Technology, 2014.

[54] M. Wächter, A. Rettenmeier, M. Kühn, and J. Peinke. Wind velocity measurements using a pulsed LIDAR system: first results. In *IOP Conference Series: Earth and Environmental Science*, volume 1, page 12066, 2008. doi: 10. 1088/1755-1307/1/1/012066. URL http://stacks.iop.org/1755-1315/1/i=1/a= 012066?key=crossref.30aba9bfb6133a2aaad1585eaf156e7b.

[55] J. W. Wagenaar, S. Davoust, A. Medawar, G. Coubard-Millet, and K. Boorsma. Turbine performance validation; the application of nacelle lidar. In *EWEA 2014*, page 10. ECN Wind Energy, 2014.

[56] R. Wagner, I. Antoniou, S. M. Pedersen, M. S. Courtney, and H. E. Jørgensen. The influence of the wind speed profile on wind turbine performance measurements. *Wind Energy*, 12(4):348–362, 2009. ISSN 10954244. doi: 10.1002/we.297.

[57] R. Wagner, T. Mikkelsen, and M. Courtney. Investigation of turbulence measurements with a continuous wave, conically scanning LiDAR. Technical Report March, DTU, 2009.

[58] R. Wagner, M. Courtney, J. Gottschall, and P. Lindelöw-Marsden. Accounting for the speed shear in wind turbine power performance measurement. *Wind Energy*, 14 (8):993–1004, nov 2011. ISSN 10954244. doi: 10.1002/we.509. URL http://arxiv. org/abs/1006.4405http://doi.wiley.com/10.1002/we.509.

[59] R. Wagner, R. L. Rivera, I. Antoniou, S. Davoust, T. F. Pedersen, and M. Courtney. Procedure for wind turbine power performance measurement with a two-beam nacelle lidar. Technical Report 0019, DTU Wind Energy, 2013.

[60] R. Wagner, T. F. Pedersen, M. Courtney, I. Antoniou, S. Davoust, and R. L. Rivera. Power curve measurement with a nacelle mounted lidar. *Wind Energy*, 17(9):1441–1453, 2014.

[61] H. J. Wessels. *An experimental study into accuracy of novel techniques in Power Curve verification.* PhD thesis, Delft University of Technology, 2015.

[62] S. Wharton, Z. Irons, J. Newman, and W. O. Miller. 2013-2014 Lidar Campaign: Measurements of Inflow at a Northern Oklahoma Wind Farm. Technical report, Lawrence Livermore National Laboratory, 2014. URL https://e-reports-ext.llnl.gov/pdf/782120.pdf.

[63] W. Widada, H. Kinjo, H. Kuze, N. Takeuchi, and M. Sasaki. Effect of Multiple Scattering in the Lidar Measurement of Tropospheric Aerosol Extinction Profiles. *Optical Review*, 8(5):382–387, 2001. ISSN 1340-6000.

[64] J. Wieringa and P.J. Rijkoort. Windklimaat van Nederland. pages 1–261, 1983.

[65] Zephir Ltd. ZephIR Lidar Brochure. Technical report, Zephir Ltd., 2015.

Appendices

Appendix A

IEC standard

In this appendix, the guidelines of the IEC standard regarding measurement sectors and measurement devices are discussed.

A.1   Measurement sector

Sources of wind flow distortions like topographical variations, other wind turbines and obstacles are to be determined. The measurement directions during operation can be divided into sectors. If a sector is disturbed by a wake of an obstacle or wind turbine, its impact on the met-mast and turbine should be estimated. In Figure A.1, the requirements concerning distance and wake effects are shown for a met-mast.

First of all, small wind turbines will be regarded as obstacles if their height is less than $\frac{2}{3}\left(H - \frac{D}{2}\right)$. Wind turbines should also be regarded as obstacles in stopped conditions, however for simplicity the assumption is made that the wind turbines are continuously in operation. The effects of neighbouring turbines should be determined for both the turbine under test and the measurement device. The following dimensions are necessary: distance and direction from the turbine next to the measurement device or turbine under test, L_n and θ_n, and its rotor diameter, D_n. Also, the wake effect of the wind turbine under test on the measurement device should be taken into account.

Secondly, the obstacles that influence the wind conditions measured by the measurement device or that affect the wind turbine under test should be analysed. The effects of an obstacle on the measurement device and turbine under test should be incorporated if it does not meet the requirements from Figure A.2. In this case, the following dimensions are necessary: distance and direction from the obstacle to the measurement device or turbine under test, L_e and θ_e, and its equivalent rotor diameter as calculated with the following equation:

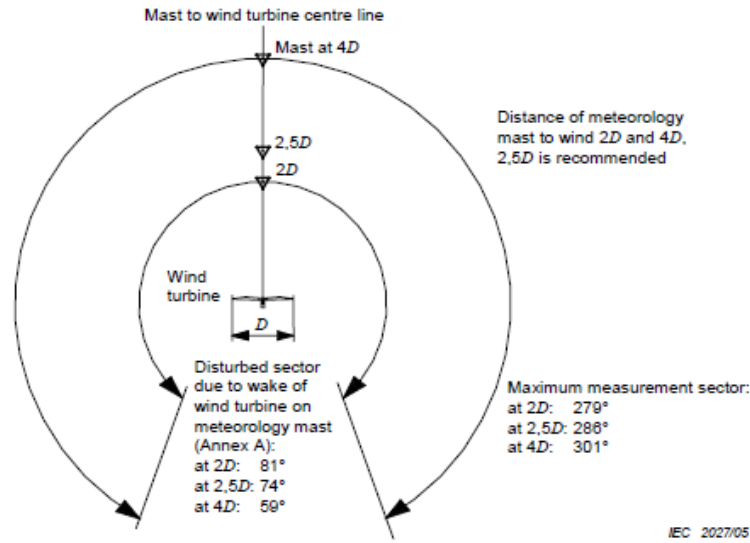$$D_e = \frac{2l_h l_w}{l_h + l_w} \tag{A.1}$$

Figure A.1: Requirements concerning distance and wake effects for a meteorological mast including maximum allowed measurement sectors[21]

where D_e represents the equivalent rotor diameter while l_h and l_w indicate the obstacle height and width seen from the perspective of the measurement device or turbine under test. Obstacles with a width larger than 50 m should be divided into partial obstacles with a maximum width of 50 m. Then, each partial obstacle can be evaluated separately. Finally, the disturbed measurements sectors of obstacles and turbines can be determined by using the graph in Figure A.3, where θ_d is the disturbed sector width. The sector to exclude, between θ_l and θ_r, can be calculated with Equation A.2.

$$\theta_l = \theta_n - \frac{1}{2}\theta_d \tag{A.2a}$$

$$\theta_r = \theta_n + \frac{1}{2}\theta_d \tag{A.2b}$$

A.2 Requirements measurement devices

The IEC also prescribes standards for the measurement devices which are given in Figure A.4. These standards are to be followed for power performance test according to the IEC standards.

Distance*	Sector**	Maximum obstacle height from terrain surface***
<2 L	360°	<1/3 (H-0,5 D)
≥2 L and < 4 L	Preliminary measurement sector	<2/3 (H-0,5 D)
≥4 L and <8 L	Preliminary measurement sector	< (H-0,5 D)
≥8 L and <16 L	Preliminary measurement sector	<4/3 (H-0,5 D)
≥2 L and <16 L	Clearly outside preliminary measurement sector by 40° or more	No limit to height

* from obstacle to wind turbine under test, respectively from obstacle to WME – whereas L is the horizontal distance between wind turbine under test and wind measurement equipment

** *Preliminary measurement sector* shall be understood here as the valid sector which remains after evaluation of neighbouring operating wind turbines (as described in Clause A.2, using the calculation described in Clause A.4), whereas all directions which are less than 40° outside shall also be considered.

*** *H* is the hub height and *D* is the rotor diameter of the wind turbine under test.

Figure A.2: Obstacle requirements for exclusion of measurement sectors[22]
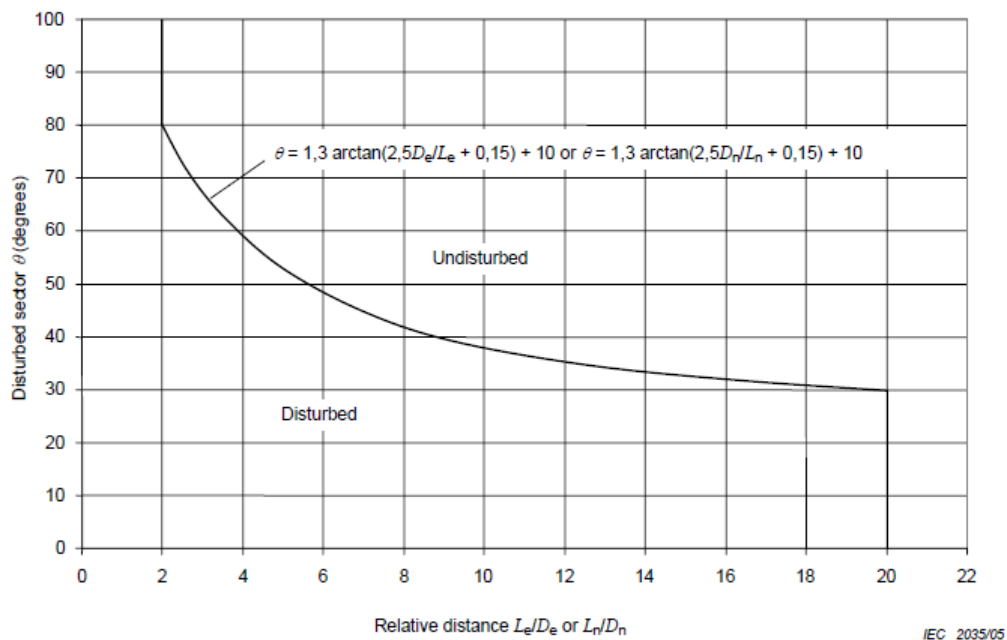
Figure A.3: Sector to exclude as a result of wake effects from neighbouring wind turbines and obstacles[22]

Measurement quantity	Device requirements
Electric power	Class 0.5 or better, meaning a maximal error of 0.5 % at rated power. Device to be mounted between turbine and electrical connection.
Wind speed	Class 1.7A or better, so uncertainty < 0.05 m/s+ 0.005*V. Device to be mounted at ±2.5% from hub-height.
Wind direction	Wind vane mounted on boom. Combined uncertainty less than 5 degrees.
Air temperature	Mounted within 10m of hub height.
Air pressure	Mounted close to hub height.
Turbine signals	Status signals of turbine required. At least data acquisition at 1Hz frequency.

Figure A.4: Standards for the measurement devices in power performance tests[61]

Appendix B

Error in direction measurements turbine N03

This appendix discusses the errors in the nacelle direction of turbine N03 at Prinses Alexia.

The offset of 35° in measuring wind and nacelle direction by turbine N03 was reported to the data analysis team of Vattenfall. First, the performance of turbine N03 was investigated to check if the error resulted in YM. As the wind direction measured by the nacelle anemometer showed a similar offset, it was not expected that the error led to YM, since the turbine aligns with this measured wind direction. However, it could be that the wind direction was measured incorrect and thus also turned the turbine into the wrong direction. A similar turbine performance as for the turbine next to it, N04, was found. Also, the error was continuously 35° which could indicate an incorrect calibration. Therefore, Senvion was contacted to solve this problem and ensure correct direction measurements.

First, the erroneous measurements of both turbines in a specific direction range were investigated by checking when this occurred. If it was during one day or a week, it could be due to a temporary technical problem. On the other hand, when it occurred during the whole measurement campaign the sensors should be checked and fixed. First, the Lidar measurements were filtered between 20° and 45°. This range occurred several times throughout the whole measurement campaign (Jan 2016-April 2016). At these times, the directions measured by turbine N04 were close to the Lidar direction measurements while the directions of turbine N03 varied. This was also found for the direction measurements of turbine N04 above 340°.

Since this does not directly mean that the turbines could not measure these directions, the measurements of the turbines were also filtered for the particular direction ranges. It was observed that the data of turbine N03 contained measurements between 20° and 45°, but they differed again significantly from the Lidar and turbine N04. Likewise, the dataset of turbine N04 contained direction measurements above 340°. However, these measurements did not correspond with the directions measured by Lidar and turbine N03. Therefore,

a fault is clearly present in the direction measurements within a specific range for each turbine.

Finally, the cause of the mis-calibration was investigated and one problem revealed. During installation of the nacelle, the turbine's north direction is drawn inside the nacelle using the magnetic north measured by a compass. However, when all the equipment is already installed, the magnetic field will be disturbed resulting in an erroneous calibration of the turbine's north. Hereafter, the turbine data uses this wrong direction as reference which causes the offset in the turbine direction measurements. Therefore, it is recommended to calibrate the north before installing the generators inside the hub.

Temperature, pressure and humidity measurements

In this appendix the underlying parameters of air density are presented: temperature, pressure and humidity. These measurements are presented to investigate the difference between the results of the air density measured by the Lidar and met-mast at Prinses Alexia.

C.1 Temperature

The temperature measurements of the met-mast and Lidar are shown in Figure C.1a. The temperature ranges from -7°C to 21°C. A scatter plot is given in Figure C.1b to check if they compare well to each other. The meteorological station of the Lidar was located on the ground, so the temperature is corrected to hub height. Another comparison was made of the corrected measurements, which is shown in Figure C.2a and Figure C.2b.

It can be seen that the Lidar measured approximately 0.5°C (-0.2%) lower than the met-mast. The corrected measurements compare worse to each other as the uncorrected, i.e. -1.1°C (-0.40%). This can be explained by the fact that the Lidar measured lower temperatures and these had to be corrected to hub height. Since increasing altitude decreases the temperature further, an even larger difference results between the measurements.

C.2 Pressure

The pressure during the measurement campaign at Prinses Alexia measured by met-mast and Lidar is shown in Figure C.4a. A scatter plot is presented in Figure C.4b for comparison. A low scatter can be seen, but the Lidar measured on average 1.20% higher than the met-mast. After correcting the pressure measurements to hub height, the difference increased to 1.23%.

(a) Complete period

(b) Scatter plot
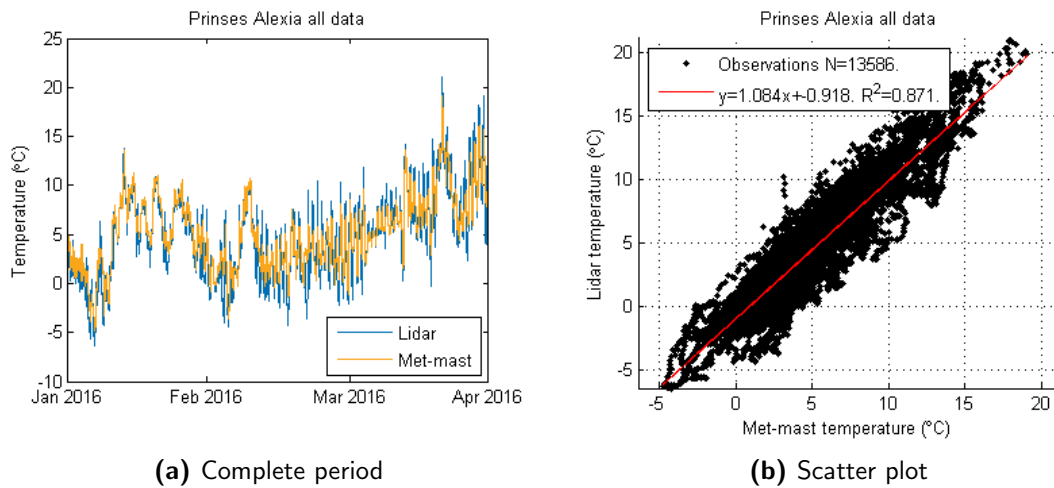
Figure C.1: Temperature measurements by the Lidar and met-mast at Prinses Alexia

(a) Complete period

(b) Scatter plot
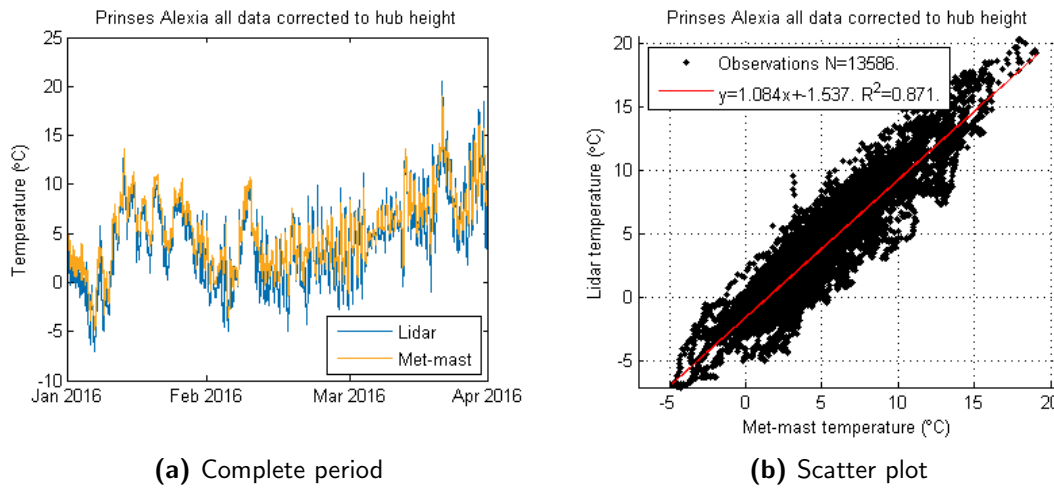
Figure C.2: Temperature measurements by the Lidar and met-mast corrected to hub height at Prinses Alexia

(a) Complete period

(b) Scatter plot
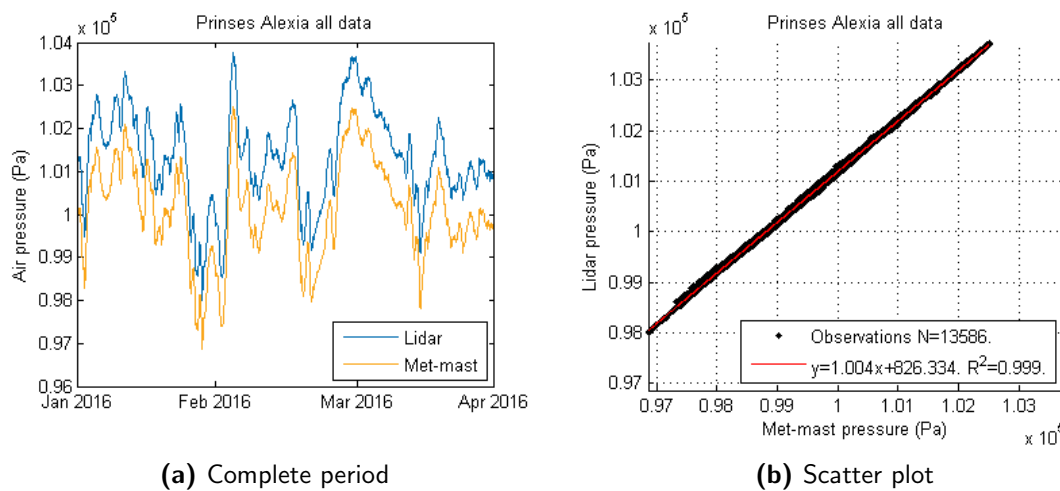
Figure C.3: Pressure measurements by the Lidar and met-mast at Prinses Alexia

(a) Complete period

(b) Scatter plot
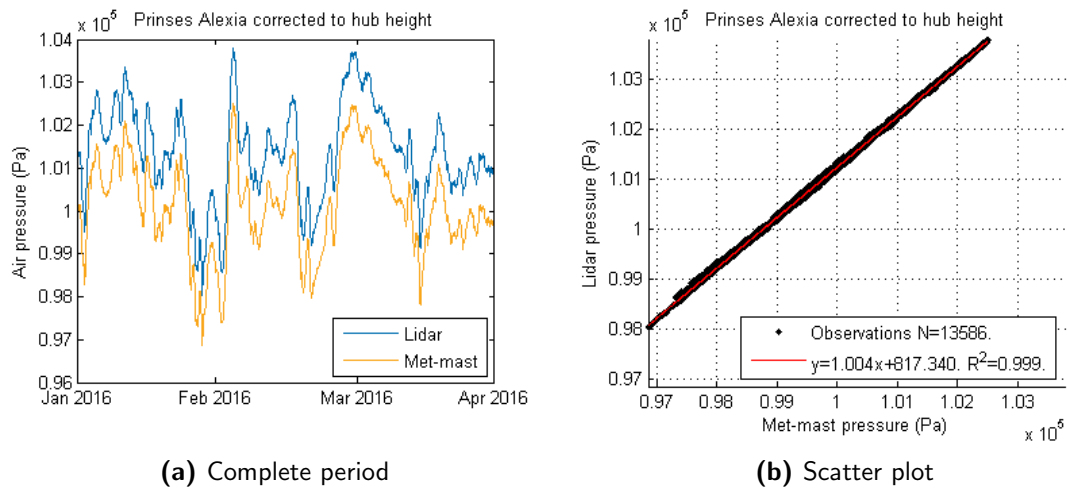
Figure C.4: Pressure measurements by the Lidar and met-mast corrected to hub height at Prinses Alexia

(a) Complete period

(b) Scatter plot
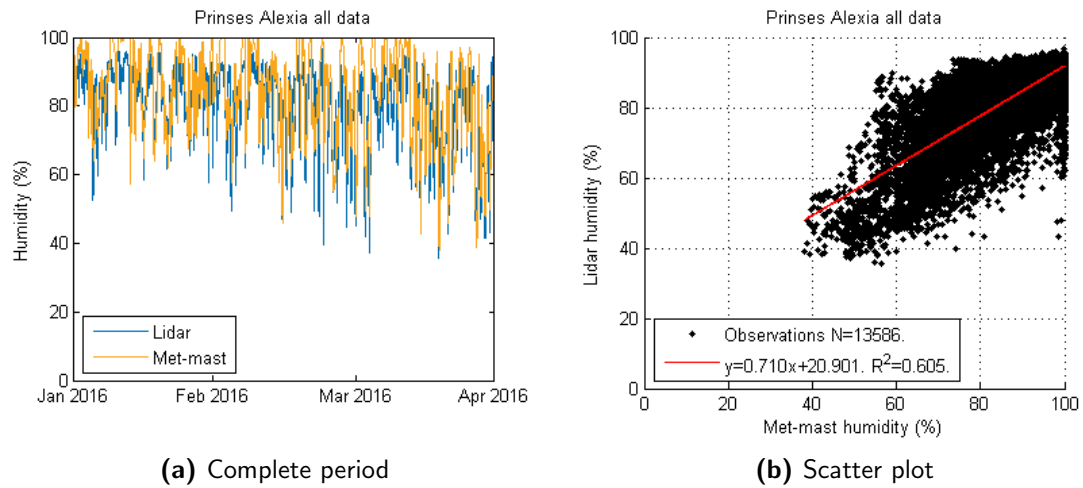
Figure C.5: Humidity measurements by the Lidar and met-mast at Prinses Alexia

C.3 Humidity

The humidity has significantly less influence on the air density when looking at Equation 2.27. The ratio of $\frac{p_{air,10min}}{R_0}$ over $\Phi p_w \left(\frac{1}{R_0} - \frac{1}{R_w} \right)$ lies between 180 and 680 during the measurement campaign. To check the measurements of the Lidar's meteorological system a comparison is made with the met-mast. The measurements are presented in Figure C.5a and the scatter plot can be seen in Figure C.5b. A large cloud of points above 50% humidity shows the large scatter for this parameter. However, the humidity cannot cause the difference in air density due to its low impact.

Appendix D

Data alignment Nørrekær Enge

In this appendix, the scatter plots are given for the alignment check of the data from Nørrekær Enge.

In Figure D.1, the alignment of the Avent Lidar is checked. From the scatter can be seen that no adjustment is required. The same results can be observed in Figure D.2 and Figure D.3 for the ZephIR Lidar and spinner anemometer respectively.

(a) -20 minutes

(b) -10 minutes

(c) Original

(d) +10 minutes

(e) +20 minutes
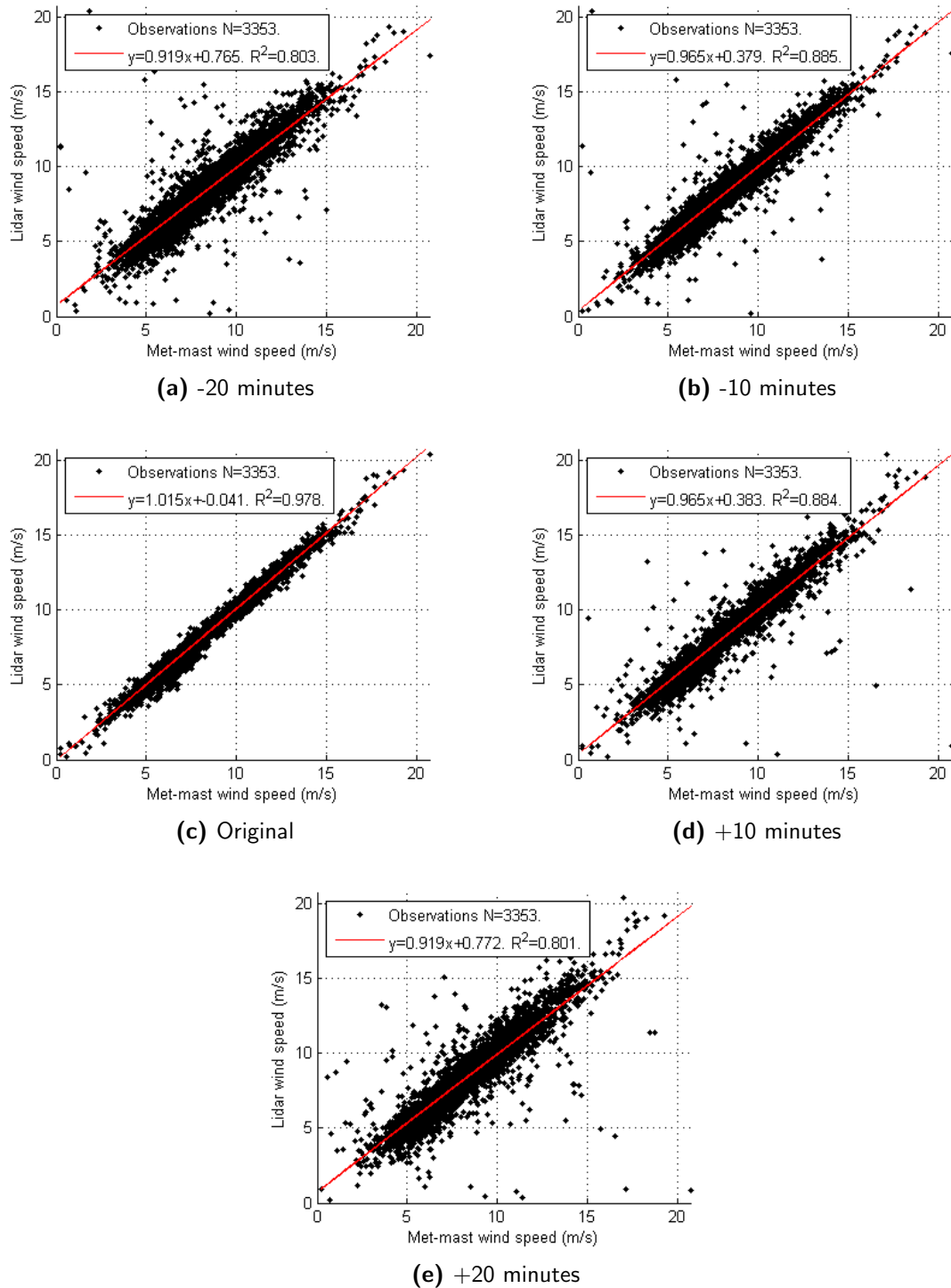
Figure D.1: Scatter plots of wind speed comparison between met-mast and Avent Lidar for different adjustments in time

(a) -20 minutes

(b) -10 minutes

(c) Original

(d) +10 minutes

(e) +20 minutes
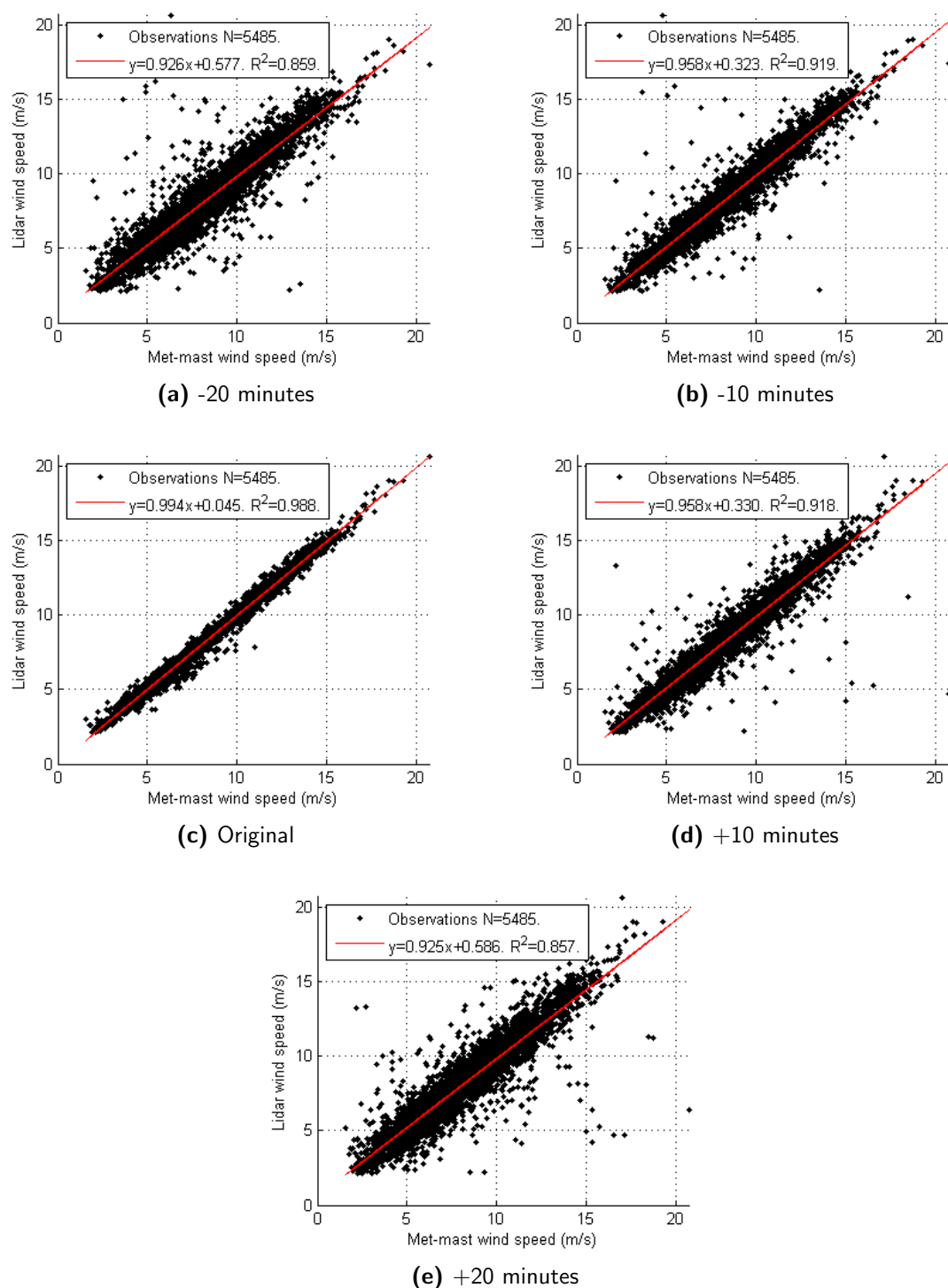
Figure D.2: Scatter plots of wind speed comparison between met-mast and ZephIR Lidar for different adjustments in time

(a) -20 minutes

(b) -10 minutes

(c) Original

(d) +10 minutes

(e) +20 minutes
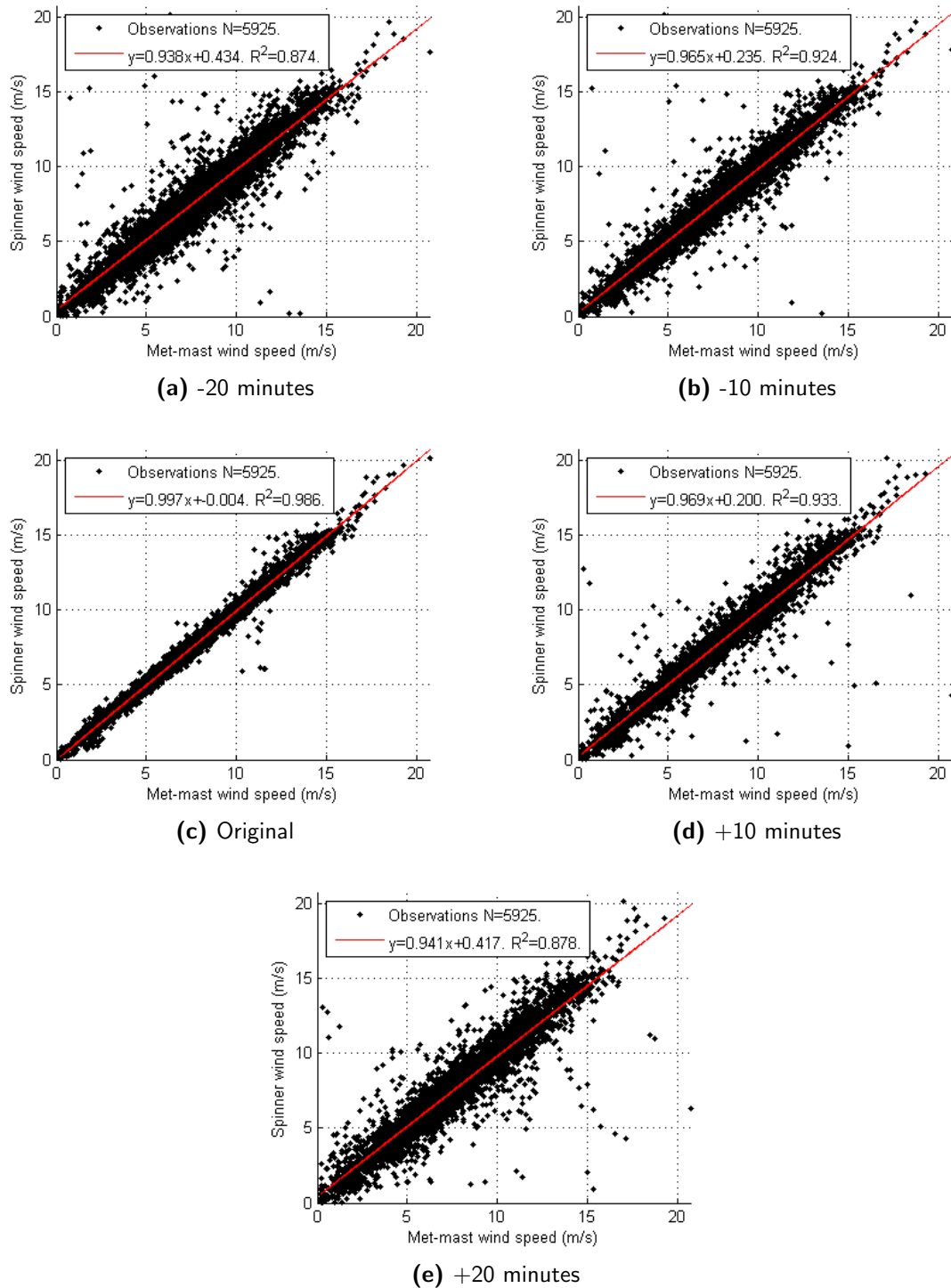
Figure D.3: Scatter plots of wind speed comparison between met-mast and spinner anemometer for different adjustments in time

Appendix E

Alternative comparisons for Nørrekær Enge

In this appendix, the scatter plots of the alternative comparisons between the Lidars and spinner anemometer are shown. As a result of the nacelle-based installation of the Lidars and spinner anemometer, the YM measurements can be compared to each other without the intervention of the turbine direction measurements, which are not trustworthy. First, the wind speed, YM and TI measurements of the nacelle-based Lidars are compared to each other. Hereafter, the measurements of both Lidars will be compared to the spinner anemometer.

To ensure a reliable comparison, the data is filtered for the undisturbed measurement sectors. In Figure E.1 can be seen that the wind speed measurements compare well, but the YM measurements show large scatter. However, the comparison of YM between the ZephIR and met-mast showed worse correlation(Figure 5.12b). From the large scatter cannot be concluded that the Lidars measure YM better than the met-mast. Similar correlation can be seen in the TI measurements as compared to met-mast(Figure 5.15a and Figure 5.15b), but again the ZephIR Lidar seems to underestimate the TI.

Besides a comparison between both Lidars, the measurements of both Lidar are compared to the spinner anemometer in Figure E.2. The wind speed measurements correlate well, which is according to previous comparisons. The YM measurements of the Avent Lidar show a better correlation with the spinner anemometer than the ZephIR Lidar, but still significant scatter can be seen. Also, the correlation between the YM measured from the met-mast in combination with the turbine data and the Avent Lidar was better (Figure 5.12a). Interestingly, the TI comparison of the Avent shows an improvement compared to the scatter plot made with the met-mast in Figure 5.15a.

(a) Wind speed
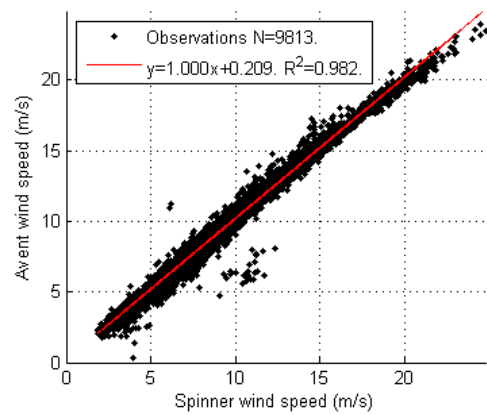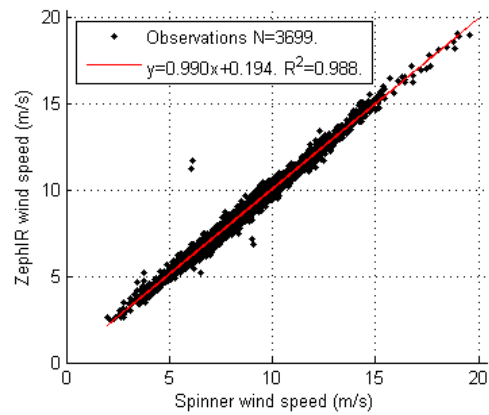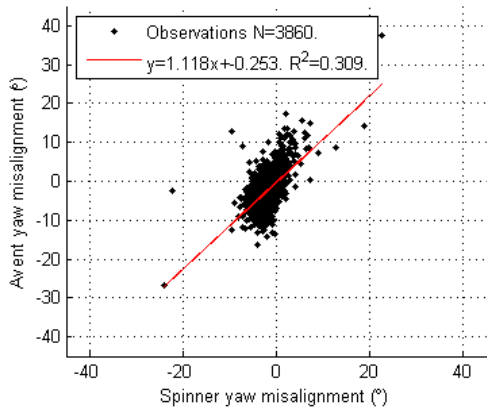
(b) YM

(c) TI
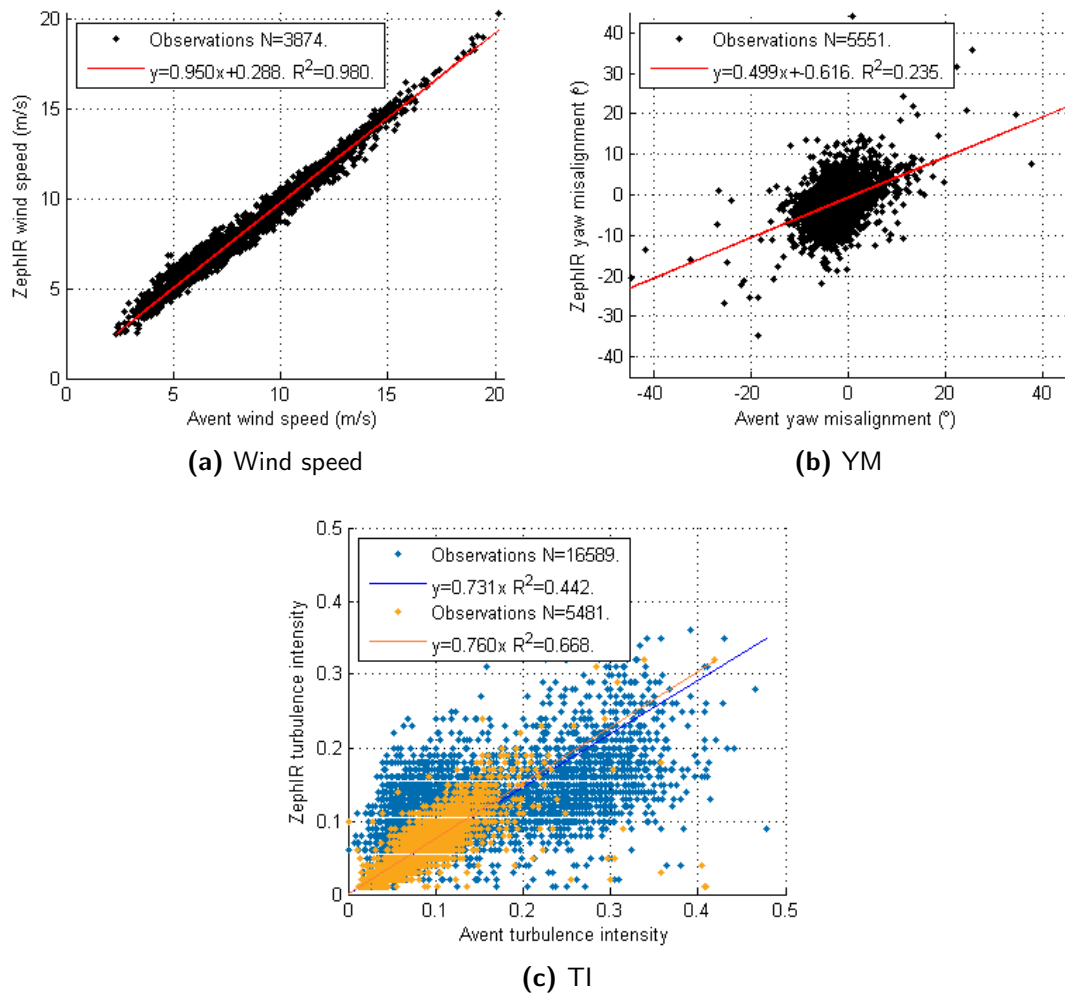
Figure E.1: Comparison between the wind speed, YM and TI measurements of the Avent and ZephIR Lidar
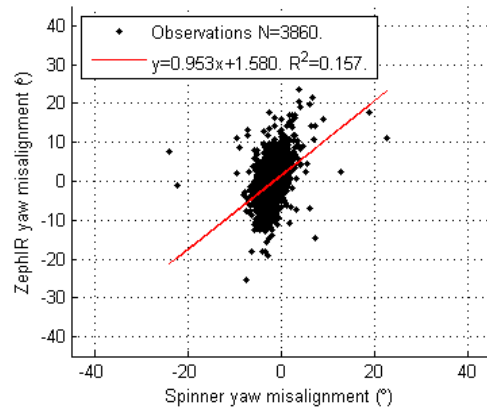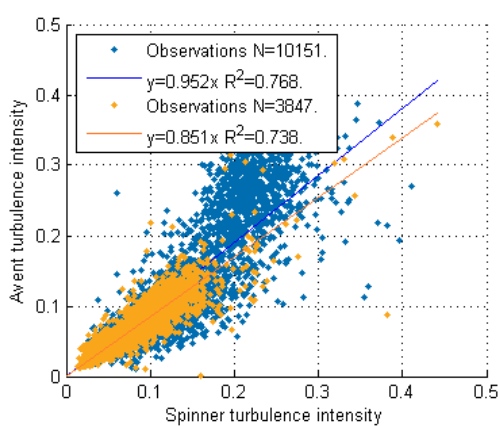
(a) Wind speed comparison to Avent Lidar

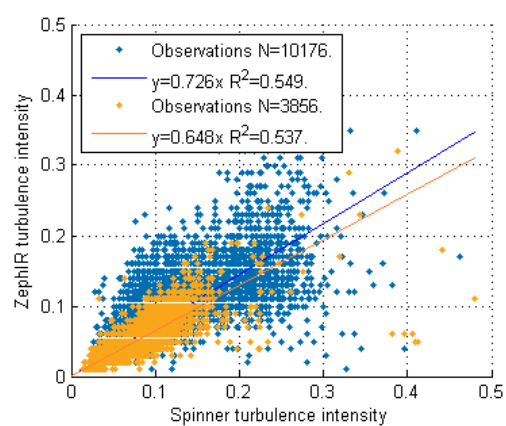**(b)** Wind speed comparison to ZephIR Lidar

(c) YM comparison to Avent Lidar

(d) YM comparison to ZephIR Lidar

(e) TI comparison to Avent Lidar

(f) TI comparison to ZephIR Lidar

Figure E.2: Comparison of wind speed, YM and TI between Lidars and spinner anemometer

Appendix F

Turbulence normalisation

In this appendix, the process of turbulence normalisation will be discussed in more detail to clarify the complex process as described in the IEC standard.

The purpose of turbulence normalisation is to find or correct for TI effects on power curves, which are discussed in subsection 3.1.1. In addition, TI normalisation can be used to obtain power curves for a TI of interest. For instance, the average TI is known of a potential site at which the turbine can be installed. Then, it is possible to determine the site specific power curve to check the turbine performance as if it would be installed at the potential site. It would also be expected that a normalisation of the power outputs to one TI value reduces scatter around the power curve. This can be explained by the fact that TI affects the power output. Also, an higher TI will lead to larger effect on the power output. As a result, normalising all power outputs to one TI should narrow the spread of power outputs.

This will be examined by generating a known set of measurements. First, five sets of wind speeds and power measurements are determined with a different TI. The wind speed ranges from 0 to 25 m/s and the corresponding power outputs are determined beforehand by taking the TI value of each set into account. The resulting power curves for each TI value are presented in Figure F.1 in which the effect of TI on the power curves can be clearly seen.

The data sets are combined after which the process of turbulence normalisation can be performed. The first step of the process consists of defining the cut-in wind speed, rated wind speed, maximum bin average of the measured power and maximum power coefficient. These parameters are required to determine the initial zero turbulence power curve, and are listed in Table F.1. How these values are defined is described in subsection 2.4.12.

Now, the iteration process begins to obtain the zero turbulence power curve and the adjustments to the parameters are to be made with Equation 7.3. Each iteration step, the rated power is adjusted with the maximum simulated power and rated power from the measurements. Before this can be done, the average simulated power within a 10-minute period should be determined with Equation 7.2 by using the binned wind speed from
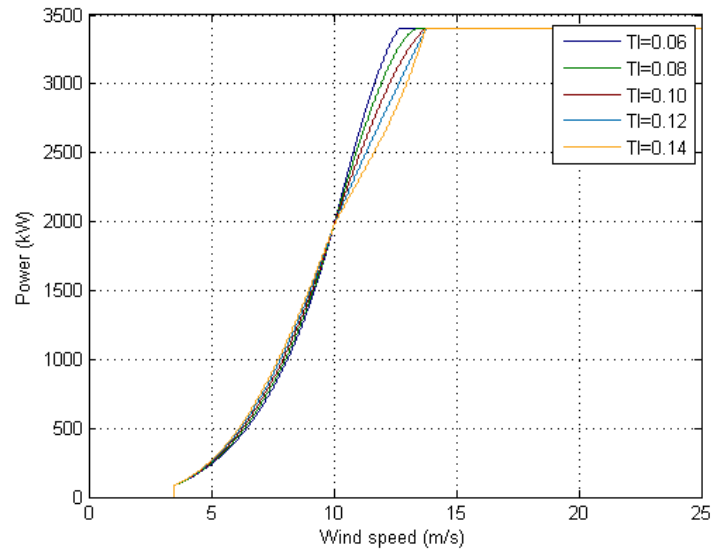
Figure F.1: Power curves for different TI

Table F.1: Initial parameters for zero-turbulence power curve

Parameter	Value
V_{cut-in}	3.5 m/s
V_{rated}	11.9 m/s
P_{rated}	3400 kW
$C_{p,max}$	0.39

the measurements to generate a Gaussian wind speed distribution and the power output from the initial zero turbulence power curve corresponding to that wind speed bin. From the simulated power curve, the cut-in wind speed should be defined using the following requirement: the wind speed at which the first power from the binned values is larger than $0.001 \cdot P_{rated}$. The other adjustment for the cut-in wind speed is constant and equal to the cut-in wind speed from the measurements. Finally, the power coefficient can be adjusted with the maximum simulated and measured power coefficient. This process continues until convergence is reached as given by the requirements set in subsection 2.4.12.

Hereafter, the measurements should be adjusted using Equation 7.4 to obtain the final zero turbulence power curve. Here, the simulated power is to be determined with the measured wind speed, measured TI and the power from the initial zero turbulence as input. The initial zero turbulence power curve is defined for wind speeds between 0 and 100 m/s in steps of 0.1 m/s, which are also used as steps in the Gaussian wind speed distribution. The power from the initial zero turbulence power curve for the measured wind speed should be determined from the initial zero turbulence power curve as follows:

$$V < v_{cut-in} : P_0 = 0 \tag{F.1a}$$

$$v_{cut-in} \leq V < v_{rated} : P_0 = \frac{1}{2}\rho_0 \cdot V^3 * C_{P_{I0,max}} * A_{swept} \tag{F.1b}$$

$$V > v_{rated} : P_0 = P_{rated} \tag{F.1c}$$

In Figure F.2, the red curves represent the measurements and the resulting initial zero turbulence power curve is shown in blue. The negative effect of TI on the power curve around rated wind speed can be clearly seen from the difference between the measurements and initial zero turbulence power curve. The iteration continued until convergence and the final zero turbulence power curve is shown in black. Especially the negative effect of TI on the power curve can be seen from the differences and adjustments between the power curves. Also, the difference between the zero turbulence power curve and the measured power curve is presented in Figure F.3.

Now the zero turbulence power curve is defined, the power curve can be normalised to a specific TI using Equation 7.5. Two different simulated power curves should be defined, one based on the wind speed and TI measurements while the other one is based on wind speed measurements and the specific TI as defined beforehand. The latter TI is chosen to normalise the measured power to a TI of interest. First the power curve will be obtained for the average TI from the measurements. By comparing the measured power curve and the power curve obtained for a TI equal to the average TI, the method can be validated. From figure Figure F.4a can be seen that the generated power curve with a TI of 0.10 compares well against the measured power curve, which indicates a correct turbulence normalisation method. In addition, the power curves are generated for different TI values as shown in Figure F.4b. As can be seen, a higher TI decreases the power more at higher wind speeds than it increases the power at lower wind speeds.

In addition, the AEP is calculated with two annual mean wind speeds for different TI values. These two wind speeds are defined in order to illustrate the change in positive and negative effects as seen from the opposite sign in the differences. So, as can be seen
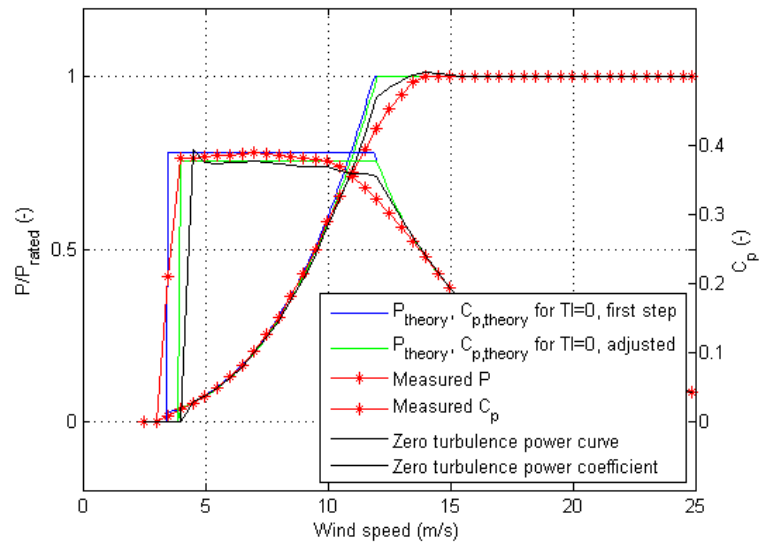
Figure F.2: Zero turbulence power curve (adjusted and final) compared to initial zero turbulence and measured power curve
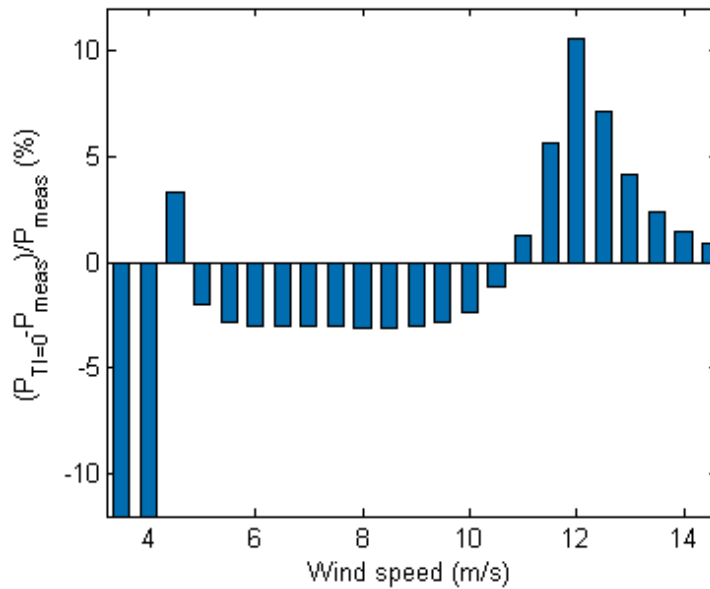

Figure F.3: Difference between zero turbulence and measured power curve
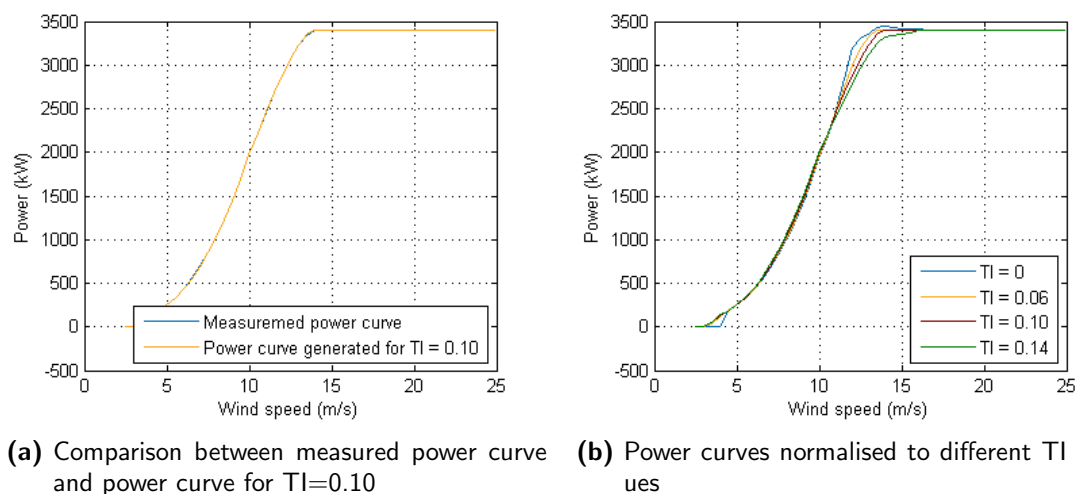
(a) Comparison between measured power curve and power curve for TI=0.10

(b) Power curves normalised to different TI values

Figure F.4: Power curve normalisation

the positive effect at low wind speeds exceeds the negative effect at high wind speeds in case of an annual mean wind speed of 6 m/s. The opposite can be observed for an annual mean wind speed of 7 m/s, which means that the contribution of higher wind speeds is increased. Therefore, a higher TI will lead to a decrease in positive and increase in negative contribution of the power outputs on the AEP. These results show the hypothesis as background for the analysis which will be performed for the measurement campaigns at Prinses Alexia and Nørrekær Enge (chapter 7).

Finally, the change in scatter is analysed after normalising the power outputs to the average TI of the measurements. This means that the power is normalised to a TI of 0.10. First, a linear interpolation is performed between the points of the binned measured power curve. Then, for each wind speed bin the scatter around the power curve can be defined. This is also done for the normalised data. The scatter is calculated by dividing the standard deviation at each wind speed bin by the rated power. Hereafter, it is possible to compare the improvement in the scatter after turbulence normalisation. In Figure F.6, the lower scatter can be clearly seen below rated wind speed. Especially around the wind speeds as discussed in subsection 3.1.1 the effect of different TI values can be seen, since after normalisation to one TI value the scatter is reduced here. This is however the ideal case in which no other factors influence the power curve.
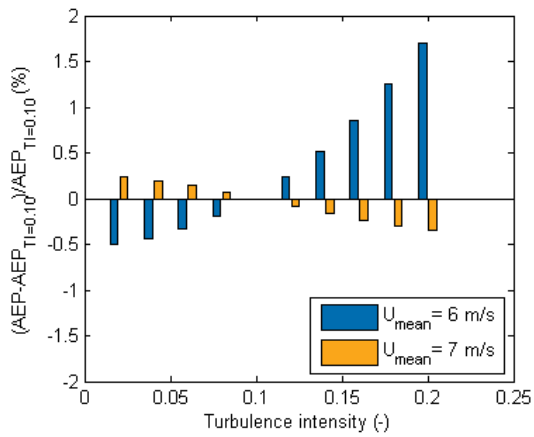
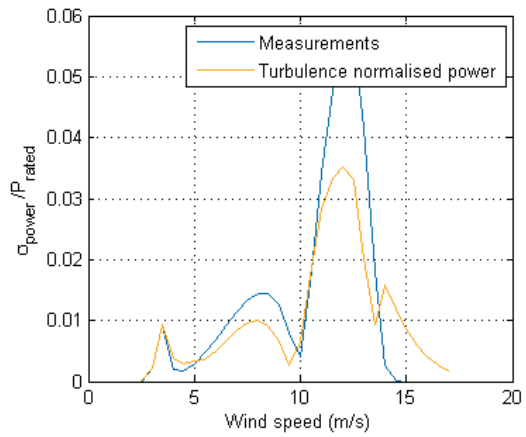**Figure F.5:** Difference between AEP at different TI values and the AEP for TI=0.10

Figure F.6: Scatter around power curve before and after turbulence normalisation

Appendix G

Generating turbulence components

In this appendix, the underlying principle of generating a turbulent wind field using a Von Karman turbulence spectrum is described. Also, the importance of a feasible frequency while generating turbulence and the resulting wind field is explained.

In Bladed, a turbulence spectrum is assumed to generate a synthetic turbulent wind field using a Fast Fourrier transform. For this thesis, a von Karman spectrum is assumed from which the turbulence components in longitudinal, lateral and vertical direction are defined. An example of a von Karman spectrum is shown in Figure G.1a. This diagram shows the frequencies, f_k, of different intensities, S, which determine the turbulence component as a function of time expressed by Equation G.1. From this expression can be seen that the turbulence component consists of different cosines which form together the variation as function of time in longitudinal wind speed shown in Figure G.1b.
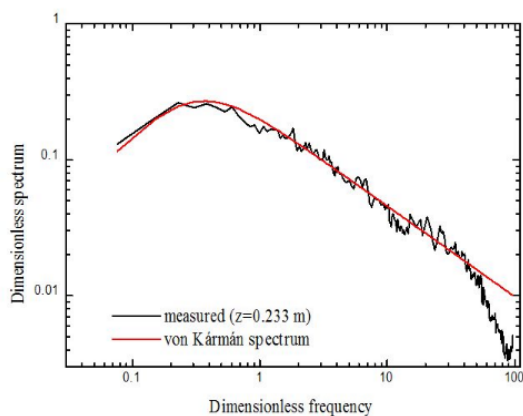
(a) Von Karman spectrum
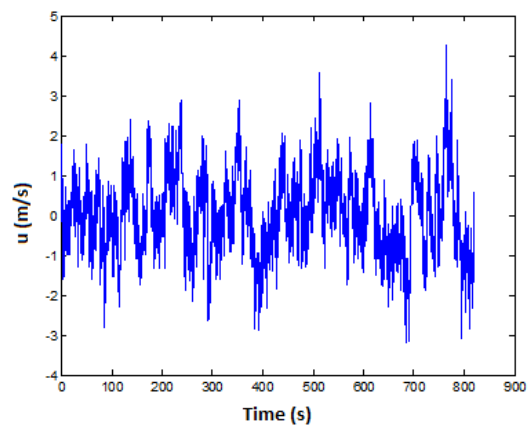
(b) Time-series of longitudinal turbulence

Figure G.1: Von Karman spectrum and the resulting time-series of the longitudinal turbulence component

Table G.1: Parameters for time-series simulation

	A [-]	$\mathbf{f_k}$ **[Hz]**	ϕ_k [-]
1	2	0.1	0
2	1.3	0.2	$0.2*\pi$
3	0.8	0.44	$0.3*\pi$
4	0.7	1.0	$-0.1*\pi$
5	0.2	1.2	0

$$u(t) = \sum_{k=1}^{K} \sqrt{S_k \Delta f_k} \cos(2\pi f_k t - \phi_k) \tag{G.1}$$

Here, f_k represents the frequency of the intensity, S_k, so how many times an intensity occurs per second within the time-series of the turbulence component u. Furthermore, K is the total number of points extracted from the diagram that gives the intensity as function of frequency, while the step in frequency, Δf_k, is related to K as follows: $\Delta f_k = \frac{f_{k,max} - f_{k,min}}{K}$. The random phase-shift of a specific cosine is given by ϕ_k.

When a wind field is generated with Bladed, the sampling frequency is an important parameter for the discrete representation of the wind speeds. A high frequency means a large number of data points per second resulting in a high resolution for the wind speed time series, because the turbulence is a component that varies significantly within one second. The effect of a low frequency, i.e. a high time step, can be observed in Figure G.2 where time-series (Equation G.2) with two different frequencies of 4 and 1 Hz are compared. The values used as input for the time-series are shown in Table G.1. The 10-minute time-series simulated with a frequency of 4 Hz results in a more detailed representation of the turbulence component, since the different cosines that form the turbulence component can be observed. On the other hand, using 1 Hz leads to an inaccurate approximation of the continuous time-series. This can also be observed from the difference in the mean values of approximately 0 m/s in the case of 4 Hz and 0.67 m/s in the case of 1 Hz. A cosine is on average 0, so using 1 Hz as frequency results in a significant deviation from the mean.

$$\begin{aligned} Y = & A_1 \cos(2\pi f_1 t + p_1) + A_2 \cos(2\pi f_2 t + p_2) + \\ & A_3 \cos(2\pi f_3 t + p_3) + A_4 \cos(2\pi f_4 t + p_4) + \\ & A_5 \cos(2\pi f_5 t + p_5) \end{aligned} \tag{G.2}$$

The importance of a sufficient frequency also holds for the turbulence component, for which a sufficient amount of data points should be used to approach the Von Karman spectrum accurately enough. Finally, the simulations of the Lidar measurements should not be limited by the time-series inaccuracy due to its low resolution as a result of a low frequency.

The effect of the Lidar sample frequency can also be investigated. As can be seen in Figure G.2, measurements are taken at 1 Hz, which is a regular measurement frequency
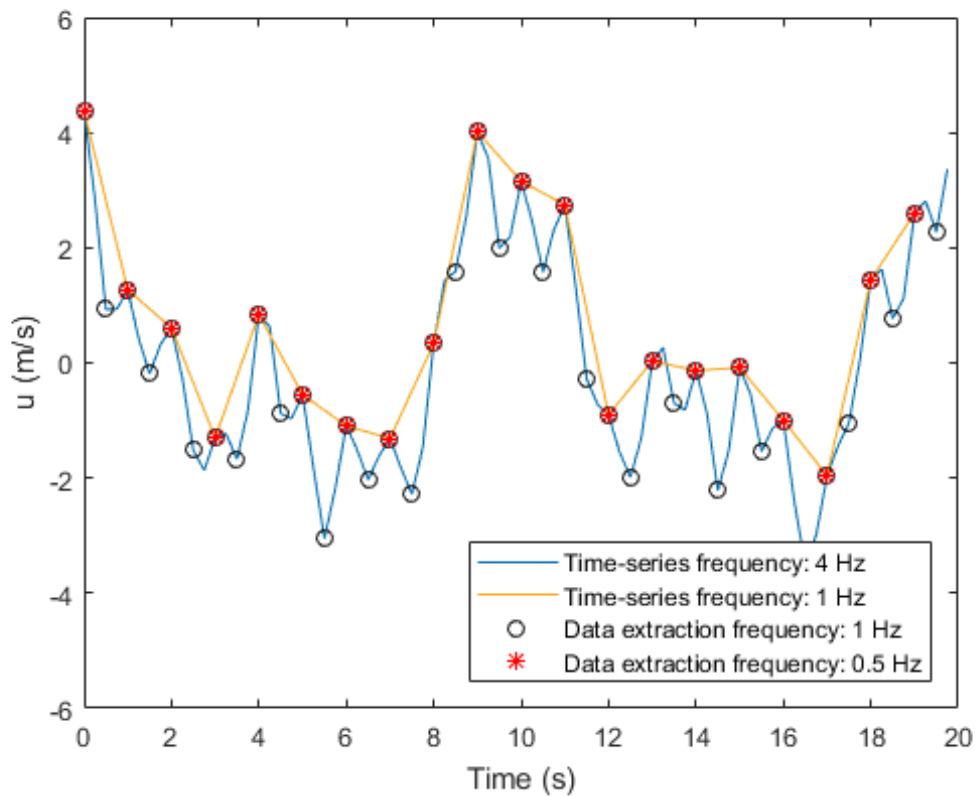
Figure G.2: Time-series plotted using different time steps including data extraction frequency

for Lidar and lower than the turbulence generation frequency. As a result, the mean of the measurements would be 0.67 m/s instead of 0 m/s. However, the possibility to increase the measurement frequency would be interesting to get a better approximation. For instance, a measurement frequency of 2 Hz would have resulted in a mean of 0 m/s. However, this is caused by the higher wind speed measurements that compensate the lower every set of 2 measurements as can be observed in Figure G.2, while at 1 Hz only the tops are measured. Therefore, the effect of measurement frequency will also be looked into during the heterogeneity simulations.

Appendix H

Alternative heterogeneity simulations

In this appendix, the results are shown for the heterogeneity simulations for different TI and using a different sample frequency .

From Figure H.5 until Figure H.10 can be seen that a sample frequency of 2 Hz does not result in noticeable changes. So, from these simulations can be concluded that for 10-minute average measurements an increase of the sample frequency to 2 Hz would not lead to better measurements.

On the other hand, after doubling the TI the difference between the measured HWS and the HWS at the reference location increases only in case of the linear adjustment in the wind field (Figure H.3 and Figure H.4). This larger difference can also be seen after applying a linear correction while a non-linear correction results in an accurate approximation of the HWS. The results of the wind direction and TI show no differences compared to the simulations with the original TI. Again, the effect of an increase in sample frequency is analysed, but no improvement can be observed.

Furthermore, simulations were performed with half of the TI values from which the results can be seen in Figure H.1 and Figure H.2. The same results can be observed compared to the original TI. So, changing the sample frequency or TI show only limited effects on the HWS and linear correction of it in the case of a linear adjustment in the wind field. Looking into the results in case of a sinusoidal adjustment, no noticeable changes are observed.
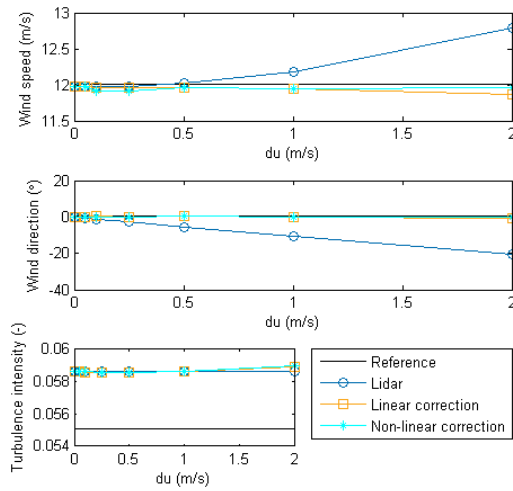
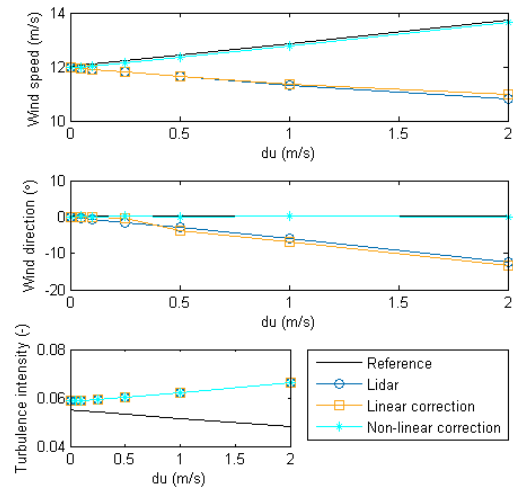**Figure H.1:** Two-beam Lidar simulations after halving TI for the linear adjustments including corrections

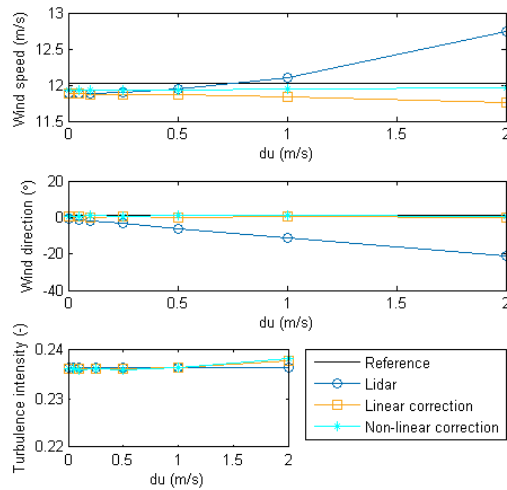**Figure H.2:** Two-beam Lidar simulations after halving TI for the sinusoidal adjustments including corrections

Figure H.3: Two-beam Lidar simulations after doubling TI for the linear adjustments including corrections
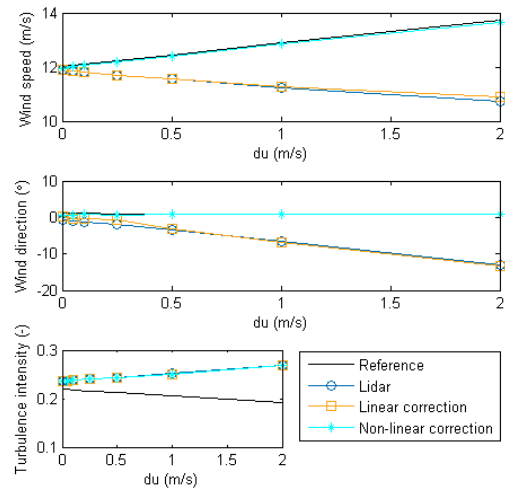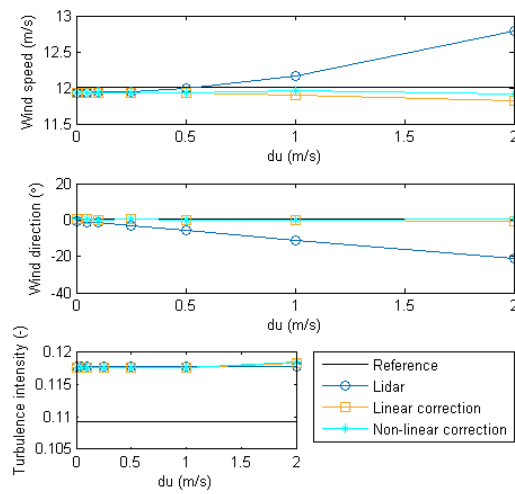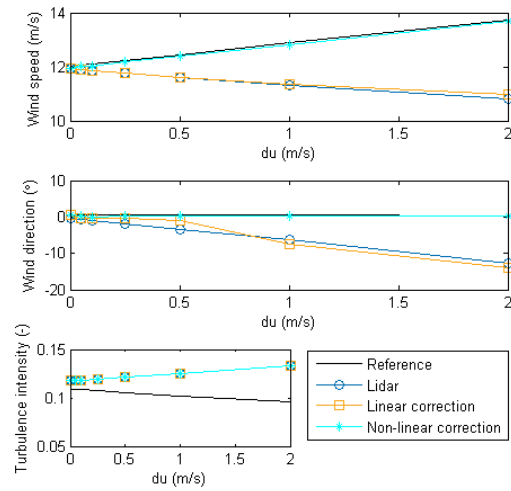

Figure H.4: Two-beam Lidar simulations after doubling TI for the sinusoidal adjustments including corrections

Figure H.5: Two-beam Lidar 2 Hz simulations for the linear adjustments including corrections

Figure H.6: Two-beam Lidar 2 Hz simulations for the sinusoidal adjustments including corrections
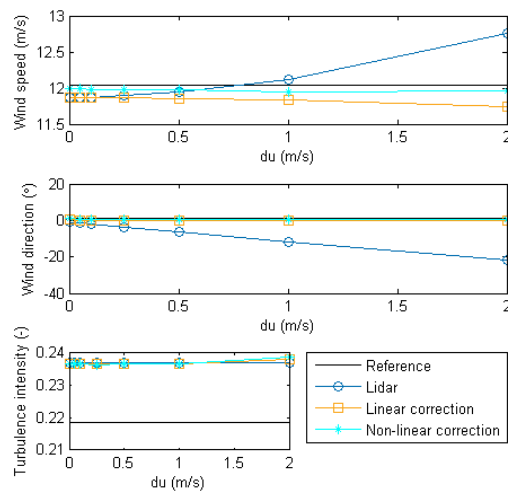

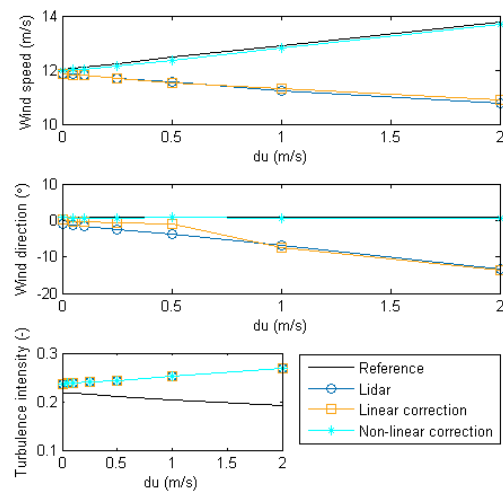**Figure H.7:** Two-beam Lidar 2 Hz simulations after doubling TI for the linear adjustments including corrections

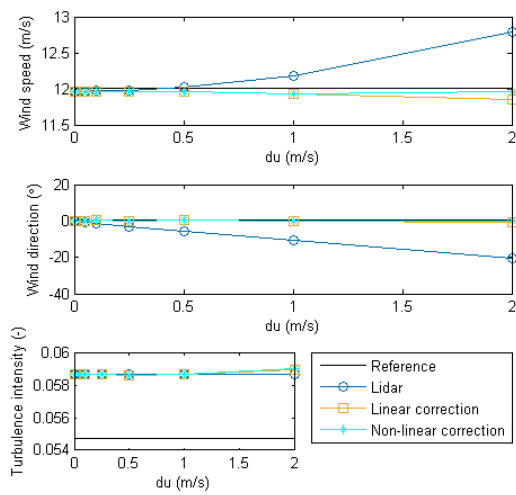**Figure H.8:** Two-beam Lidar 2 Hz simulations after doubling TI for the sinusoidal adjustments including corrections

Figure H.9: Two-beam Lidar 2 Hz simulations after halving TI for the linear adjustments including corrections
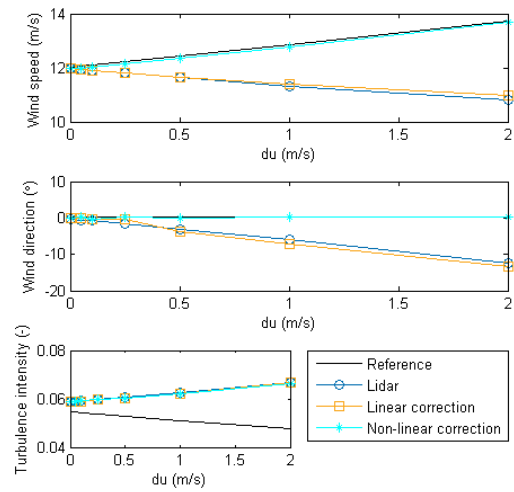

Figure H.10: Two-beam Lidar 2 Hz simulations after halving TI for the sinusoidal adjustments including corrections